SPACE CHARGE EFFECT MEASUREMENTS FOR A MULTI-CHANNEL IONIZATION CHAMBER USED FOR SYNCHROTRON RADIATION

DISSERTATION

zur Erlangung des Grades eines Doktors

der Naturwissenschaften

Vorgelegt von

Amgad Nasr

eingereicht bei der Naturwissenschaftlich-Technischen Fakultät
der Universität Siegen

Siegen 2012

Gutachter der Dissertation: **Prof. Dr. A. H. Walenta**

Prof. Dr. I. Fleck

Prüfer: **Prof. Dr. H. D. Dahmen**

Prof. Dr. C. Grupen

Datum der Disputation: **18. July 2012**

Abstract

In vivo coronary angiography is one of the techniques used to investigate the heart diseases, by using catheter to inject a contrast medium of a given absorption coefficient into the heart vessels. Taking X-ray images produced by X-ray tube or synchrotron radiation for visualizing the blood in the coronary arteries.

As the synchrotron radiation generated by the relativistic charged particle at the bending magnets, which emits high intensity photons in comparison with the X-ray tube. The intensity of the synchrotron radiation is varies with time. However for medical imaging it's necessary to measure the incoming intensity with the integrated time.

The thesis work includes building a Multi-channel ionization chamber which can be filled with noble gasses N_2, Ar and Xe with controlled inner pressure up to 30 bar. This affects the better absorption efficiency in measuring the high intensity synchrotron beam fluctuation. The detector is a part of the experimental setup used in the k-edge digital subtraction angiography project, which will be used for correcting the angiography images taken by another detector at the same time.

The Multi-channel ionization chamber calibration characteristics are measured using 2 kW X-ray tube with molybdenum anode with characteristic energy of 17.44 keV.

According to the fast drift velocity of the electrons relative to the positive ions, the electrons will be collected faster at the anode and will induce current signals, while the positive ions is still drifting towards the cathode. However the accumulation of the slow ions inside the detector disturbs the homogeneous applied electric field and leads to what is known a space charge effect.

In this work the space charge effect is measured with very high synchrotron photons intensity from EDR beam line at BESSYII. The strong attenuation in the measured amplitude signal occurs when operating the chamber in the recombination region. A plateau is observed at the amplitude signal when operating the chamber in the saturation region.

Time response measurement is carried out by filling the chamber with different gasses pressure of argon methane mixture of (90%:10%) and pure nitrogen gas, using a lead slit chopper for pulsating the incoming synchrotron beam. The output current signal is measured with tuning the applied high voltage from recombination regime up to saturation regime.

The numerical simulation is applied to understand the effect of the space charge, recombination effects and the charge dynamics behavior inside the ionization chamber.

Zusammenfassung

In vivo-Koronarangiographie ist eine der Techniken die verwendet wird, um Herzkrankheiten zu untersuchen. Hierzu wird mittels Katheter ein Kontrastmittel mit einem bestimmten Absorptionskoeffizienten in die Herzgefäße injiziert. Anschließend aufgenommene Röntgenbilder ermöglichen die Visualisierung des Blutflusses in den Koronararterien. Als Röntgenquellen können sowohl Röntgenröhren als auch Synchrotrone dienen.
Synchrotronstrahlung wird durch Ablenkung relativistischer, geladener Teilchen (z.B. bei der Durchquerung von Ablenkmagneten) erzeugt und hat im Vergleich zur Röntgenröhre u.a. eine höhere Intensität. Die Intensität der Synchrotron-Strahlung variiert mit der Zeit. Für die medizinische Bildgebung ist es jedoch notwendig, die eingehende Intensität über die Zeit zu integrieren.
Diese Arbeit umfasst den Aufbau einer Multi-Channel-Ionisationskammer, die mit den Edelgasen N_2, Ar und Xe bei variablen Innendrucken mit bis zu 30 bar gefüllt werden kann. Dies erhöht die Absorptions-Effizienz bei der Messung von Intensitätsfluktuationen der Synchrotronstrahlung. Der Detektor ist Teil des experimentellen Aufbaus im Projekt der digitalen K-Kanten Subtraktionsangiographie und dient der Korrektur der Angiographie-Bilder eines zweiten Detektors, der zeitgleich misst.
Die Kalibrierung der Multi-Channel-Ionisationskammer wurde mit einer 2 kW Röntgenröhre mit Molybdän-Anode bei einer charakteristischen Energie von 17.44 keV durchgeführt. Aufgrund der höheren Driftgeschwindigkeit der Elektronen relativ zu den positiven Ionen werden die Elektronen schneller an der Anode gesammelt, wo sie bereits ein Stromsignal induzieren, während die positiven Ionen noch in Richtung der Kathode driften. Die Akkumulation der langsamen Ionen im Inneren des Detektors stört das homogen angelegte elektrische Feld und führt zu einem Raumladungs-Effekt.

Für diese Arbeit wurde der Raumladungs-Effekt bei sehr hoher Photonen-Intensität an der EDR-Beamline bei BESSYII gemessen. Beim Betrieb der Ionisationskammer im Rekombinationsbereich tritt eine starke Dämpfung der gemessenen Signalamplitude auf. Im Sättigungsbetrieb lässt sich ein Plateau-artiges Verhalten der Signalamplitude beobachten.

Zeitaufgelöste Messungen der Detektor-Response wurden für verschiedene Gasdrucke eines Argon Methan-Gemisches (90%:10%) sowie reinem Stickstoff durchgeführt. Hierzu wurde der Synchrotronstrahl durch eine rotierende Schlitzscheibe aus Blei gepulst und während dessen das Ausgangsstromsignal in Abhängigkeit der angelegte Hochspannung vermessen. Die Hochspannung wurde hierfür über den Rekombinations-Bereich bis hin zum Sättigungs-Bereich variiert.

Zum Verständnis des Einflusses von Raumladung, Rekombinationseffekten und dem dynamischen Verhalten der Ladungen innerhalb der Ionisierungskammer wurde eine numerische Simulation durchgeführt.

Contents

Chapter 1 Introduction

1. Introduction

The aim of this project is to build and test a Multi-Strip-Ionization chamber, which will be used for monitoring the synchrotron radiation beam fluctuations for K-edge digital subtraction imaging (KEDSI), especially cardiac imaging using synchrotron radiation sources. Since a synchrotron radiation source always shows small intensity fluctuations due to mechanical movements of beam components, the need for such a correction arises when the inherently possible precision of KEDSI is to be exploited.

Synchrotron radiation sources are mostly based on electron storage rings. They consist of an evacuated annular pipe with curved sections and straight sections where electrons are travelling at relativistic velocities. The synchrotron radiation is produced either by bending magnet which are needed to keep the electrons in a closed orbit as shown in sketch diagram in Fig (1-1), or by insertion devices such as wiggler's or undulators in the straight sections. The loss energy is emitted in the form of synchrotron radiation must be replenished by accelerating cavities in the straight sections [1].

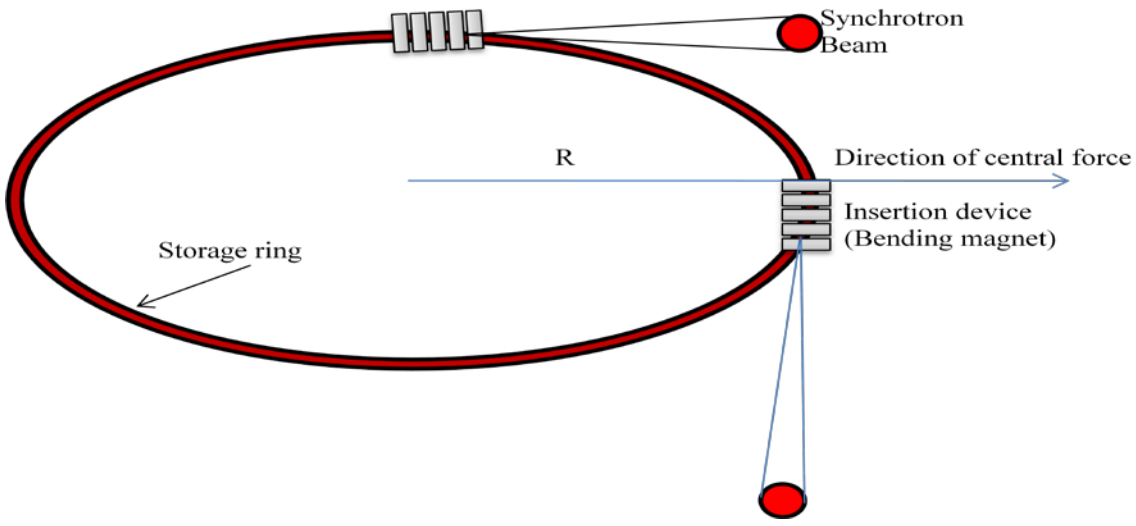

Figure 1-1: Sketch diagram shows the principle of synchrotron radiation production. Were *R* is the radius of the storage ring and the emitted photons at the bending magnet.

Synchrotron radiation has the following characteristics [2] of high brilliance which results in particular in:

1. Small divergence.
2. monochromaticity.
3. High photon intensity.

Modern synchrotron radiation sources deliver beams with such a high brilliance, that measurements with high precisions become possible as minute tracer analysis, EXAFS .etc.
Although the precision is finally limited by the photon noise, given by the variance

$$Var = N_{phot} \tag{1-1}$$

which is equal to the number of photons in a measurement, it is easily seen that the limit in precision may be extremely low: assuming 10^{12} photons in a measurement which lasts 1 sec a relative high precision of 10^{-6} should be achievable.
In practice, however this is not directly achieved. For example, in an absorption experiment governed by the relation

$$I = I_0 \exp(-\mu x) \tag{1-2}$$

With x the length of the absorption and μ the absorption coefficient. The quantity of interest, which has to be determined is

$$\mu = -\frac{1}{x} ln \frac{I}{I_0} \tag{1-3}$$

The possible errors introduced by the other quantities, x and I_0 have to be taken into account. In particular, the error of I_0 may limit the precision considerably, which is caused by the beam fluctuations. The causes for the latter could be electron beam instabilities or mechanical movement of the beam optics components. Therefore for high precision experiments usually self-calibrations procedures are employed, where beam monitoring devices are used for measuring a small fraction of the total beam.

Since X-rays are either absorbed or severely scattered, this measurement relies on the assumption, that the sub-sample measured in the monitoring device is representative to the rest of the beam used for the sample under study.

1.1. K-edge digital subtraction imaging:

The advantage of the synchrotron beam characteristics described above which are not found in any other X-ray source leads to a broad spectrum of research. There are many experiments such as medical imaging or extended x-ray absorption spectroscopy (EXAFS), where it's important

to monitor the incoming photon beam before it passes through the sample. The aim of this project was to build and test a synchrotron beam monitor which will be used for the K-edge Digital Subtraction Imaging (DSI) [3].

Today there are some medical applications with the synchrotron radiation. One of these advanced applications is the digital subtraction imaging (DSI) in energy subtraction mode (Di-chromatic angiography). This offers observation of blood vessels with a diameter far less than 1 mm which is used for basic research applications and may lead to earlier diagnostic stage of cardiovascular or cerebral diseases. A special application has been tested extensively, the intravenous coronary angiography, in order to assess the quality of these vessels without use of a catheter. Although the method proved to obtain the high contrast resolution expected, the usefulness in clinical application is limited because the left coronary artery sometimes is occulted by the ventricle filled with contrast medium. Still, the considerable effort invested in this method and the technical developments are available today for other imaging applications. Since this method set the standard for synchrotron radiation imaging it is presented here in some detail in order to elucidate the principle (Fig. 1-2).

The basic principle is that two monochromatic beams selected by monochromators from the white synchrotron radiation beam with two energies E_1 below the contrast medium K-edge and E_2 above the edge as shown in Fig. (1-2). Taking two different images by using these two monochromatic beams and subtracted them logarithmically, one can get a very significant improvement in the subtracted image. The absorption coefficient of the bone and tissue remain the same in both images and by subtracting remains only the contribution of the contrast medium, which is filled in the blood vessels by intravenous or intra-arterial methods [2, 5, 15].

The radiographic image signal is proportional to the linear absorption coefficient as following

$$N_{abs} = N_0 e^{-\mu\rho x} \tag{1-4}$$

Where N_0 initial photon flux intensity; N_{abs} the absorbed photons; μ linear attenuation coefficient; x is detector depth; ρ density.

Equation (1-4) can also be written as

$$ln\frac{N_{abs}}{N_0} = -\Delta\mu\rho x \tag{1-5}$$

$$\rho x = \frac{1}{\Delta\mu} ln\frac{N_{abs}}{N_0}$$

The setup at the synchrotron radiation source with the arrangement of the devices as shown in Fig (1-3), as the synchrotron beam emitted at the insertion device, a thin crystal monochromator is placed in front of the beam shutter to adjust the beam at different energies and delivers two monochromatic beams with energies above and below the K-edge of the contrast medium absorption coefficient. The beam monitor will be placed in front of the object and two germanium detectors are placed behind the object. Two images will be taken one image with the photon energy above the K-edge and another one with energy below the K-edge, these two images are subtracted logarithmically, the subtracted image which have very high resolution of the heart arteries will be obtained [5].

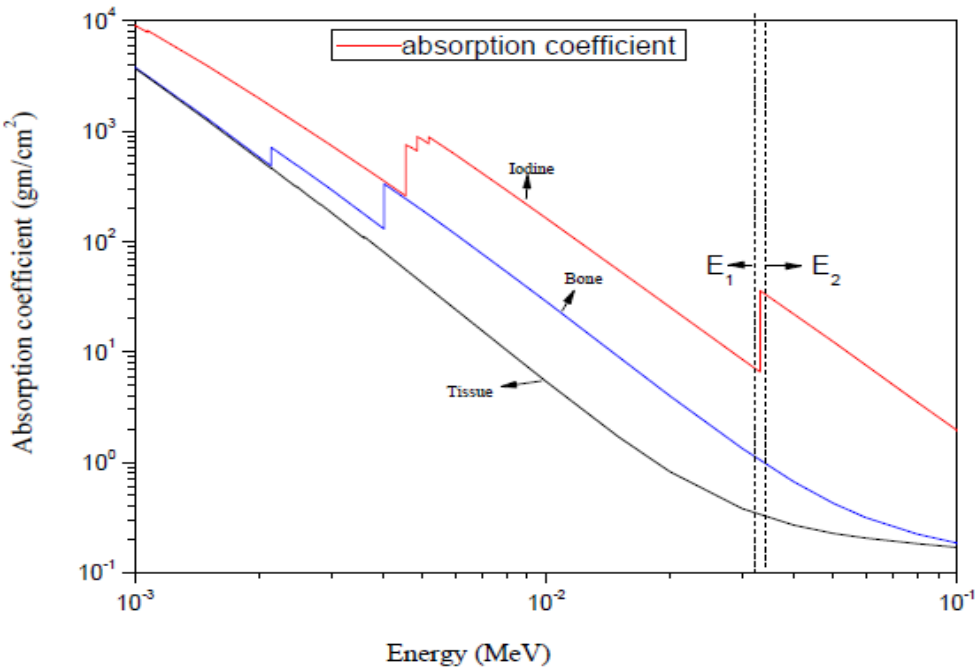

Figure 1-2: The discontinuity in the absorption coefficient of the iodine contrast medium and the contribution of the absorption coefficient of the bone and tissue which will approximately remains constant in both images.

The equation above depends on the left part which assumes that the initial photon flux intensity N_0 is constant. The intensity N_0 of the synchrotron radiation source which is emitted from the insertion device is not absolutely constant. It could be measured by a dedicated integral beam monitor. In our case this solution would not be sufficient since the vibrations of the monochromator result in a variation of the radiation intensity depending on the position on the monochromator. In preliminary tests it was found that the possible natural frequencies of the crystal cause variations which could be represented by polynomes of 8^{th} order. This was the reason to develop the multi-channel ionization chamber with at least 8 separate signal

electrodes which can measure the synchrotron beam intensity and the beam fluctuation as a function of time [4].

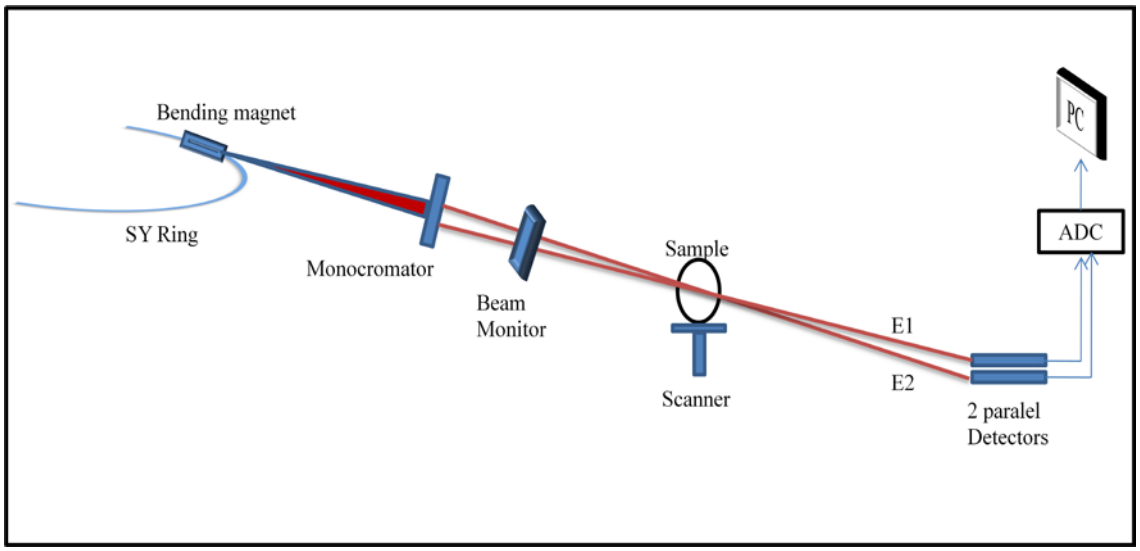

Figure 1-3: Sketch diagram of the setup at the synchrotron radiation. Were E_1 and E_2 are the synchrotron beams with energies below and above the K-edge of the contrast medium. The beam monitor is inserted before the sample to measure the beam fluctuation and two germanium detectors is after the sample.

1.2. Detector geometry

The multi-channel ionization chamber geometry consist of segmented pads to measure the synchrotron fan beam which have 8 pads upwards and 8 pads downwards separated by central electrode to measure the intensity fluctuation of two separated synchrotron beams in the same time as shown in Fig (1-3). The detector has total active length of 15 cm, height of 1 cm and 1 cm depth divided by the anode plate in the center (at depth of 0.5 cm) as shown in Fig (3-1).

In comparison, the two monochromatic synchrotron fan beams are collimated to about Δz=0.4 mm height or less, depending on the required spatial resolution of the image, and separated such that they are recorded independently in the two detector sections. In order to obtain a full two dimensional image the object is scanned with constant speed (v-scan) in vertical direction such that each line is exposed during a time $t_{\Delta x}$ of

$$t_{\Delta x} = \Delta z / v_{scan} \ . \qquad (1\text{-}6)$$

Consequently each line is exposed to the beam for $t_{\Delta x}$ which could be in the millisecond range or even below.

1.3. Detectors characteristics and limitations:

It is desirable that detectors have a linear performance with respect to the incident photon flux which is called linearity. Ideally the flowing current in the outer circuit will be equal to the ionization produced inside the ionization chamber, by the incident ionizing radiation, however at low applied electric field there is big loss in the output charge signal according to the recombination loss. This loss decreases as the applied voltage is increased which accordingly increases the remaining electric field in the detector volume and correspondingly the output charge signal. At sufficient high applied voltage the electric field is high enough to collect all the charges inside the ionization chamber. Further increase of the applied high voltage the output current will be constant which is called saturation regime. In addition to the charge signal reduction due to the recombination the reduced electric field also causes a reduction of signal current due to the slower drift velocity of the electrons and ions producing the measured current. This effect is not visible if the detector is operated in the integrating mode where the charge signal is recorded after the maximum collection time of the slower ions.

It's very important to choose the proper gas and pressure in order to achieve a good signal to noise ratio respect to the required resolution with an acceptable attenuation in the order of 1% of the incoming beam. In these work two types of gasses are used, pure nitrogen and argon methane mixture of (90:10%) with different pressure settings.
In this thesis measurements of the space charge effect are carried out with high synchrotron photon intensities. In addition numerical simulations are carried out in order to understand the charge dynamics. Besides recombination also the repulsion of the generated charges has to be taken into account and to be compared to the measurements.
A full three dimensional simulation of the space charge and associated processes is beyond the scope of this thesis and measurement with arbitrary charge generation with a realistic photon beam is technically not accessible and therefore approximations will be used (see chapter 3.1). It will be shown that useful results can be obtained, in particular with a two dimensional approximation of the electric field in order to optimize the detector design.

1.4. Time structure

The total collection time of the charges depends on the mobility of the charge carriers, the electric field strength and the distances between electrodes.

When illuminating the ionization chamber with a continuous radiation in a given time period, a current signal will flow in the outer read out electronic circuit. In the imaging application, as

explained above, time sections $t_{\Delta x}$ are considered belonging to individual lines. In practice they are obtained by integrating the detector current during the exposure time. For each individual line the flowing current pulses magnitude and duration will depend on the interaction types and position as shown in Fig (1-4) below. The measured charge is the integral of the current I_0 and distorted by time dependent fluctuations like electronic noise [6].

In conclusion, the time response of the monitor detector has to be fast enough to follow the fluctuations of the beam and to allow a clean separation of the integrated intensity during the recording of one line. This requirement is not automatically fulfilled since the response of the detector due to the slow motion of the positive ions is of importance.

A test measurement is carried out using rectangular PMMA chopper with different thickness to modulate the incoming X-ray photon flux and measure the time response signal. Different X-ray photon intensities are applied by changing the X-ray tube current. The chamber was filled with $ArCH_4$ gas mixture of (90:10%) and applying high voltage of 1 kV. The rise time of the signal was 208 µs and the fall time was 242 µs at a chopper frequency of 9.8 Hz as shown in Fig (1-5).

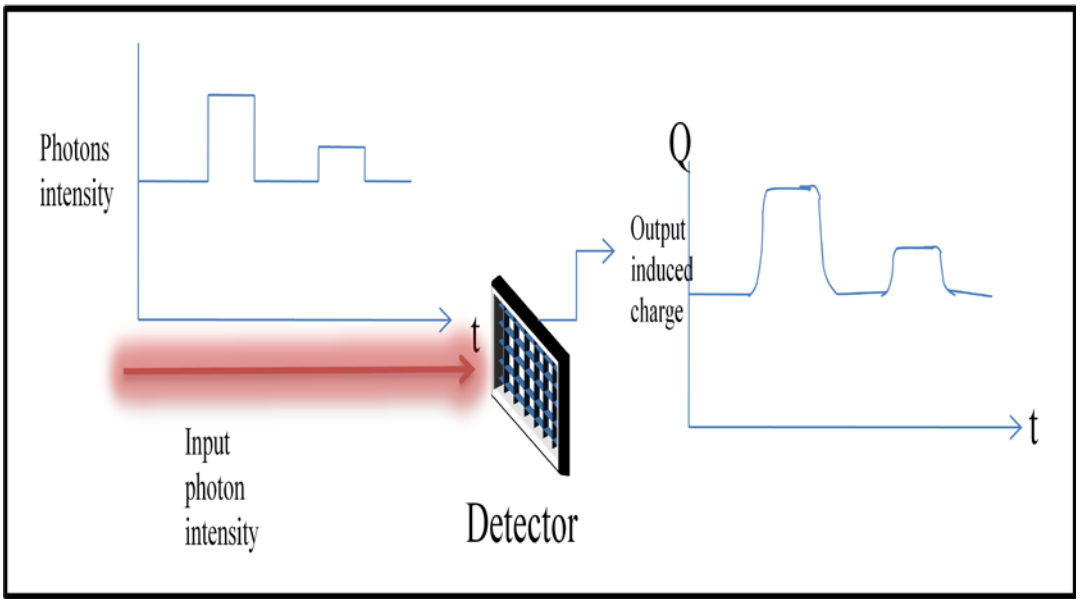

Figure 1-4: Sketch diagram of the modulated input photon intensity which enters the ionization chamber and the corresponding measured signal.

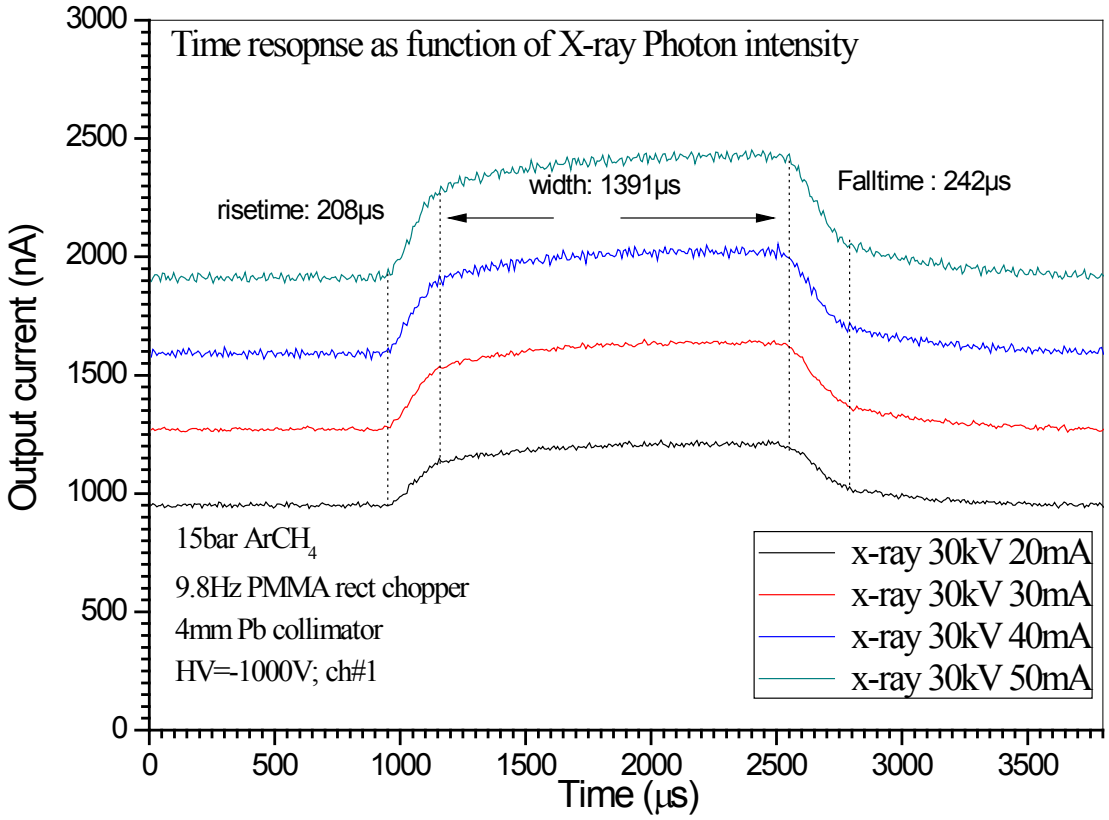

Figure 1-5: The test measurement by modulating the input photon intensity using 1cm PMMA rectangular chopper as a function of different X-ray photon intensities; showing the chopper rise and fall time.

From the above measurements and discussions, it may be anticipated that the time response of the ion chamber is critical and is investigated in detail. It should be mentioned that the two germanium detectors which are used for in the imaging setup as shown in Fig (1-3) are certainly faster since the electrons travel at about the same speed as in a gas detector but the holes in this semiconductor device travel much faster than the ions in a gas detector.

Chapter 2 Theoretical background

2. Introduction

This chapter introduces the theoretical formulas which describe the charge dynamics process during the drift and the charge expansion due to diffusion and drift processes as well recombination and induced charges in the outer plates for the gas detectors.

2.1. Basic principle

Ionization chambers are detectors filled with a certain gas in which the X-ray photons ionize the gas and create electron ion pairs. The electric field created between the electrodes separates the ions and the electrons. The electrons drift towards the anode and conversely the ions drift towards the cathode.

The detector consists of two parallel electrodes separated by a distance *d*. The gap is filled with a gas which defines the sensitive volume of the chamber. The electric field is generated by externally applied high voltage across a gap.

Ideally, the total amount of collected charges at the chamber plates must be equal to the amount of generated electrons and ions at a specific time. However, according to the difference in mobility of the ions and electrons, the charges accumulate at different times on the chamber plates. This is due to the fact that the ions are 1000 times slower than the electrons.

The slower drift of the positive ions towards the cathode plate by the applied electric field will increase the ion density near the cathode plate and minimize the ion density near the anode plate. Accordingly, the electrons which drift in the opposite direction of the ions towards the anode plate lead to a higher electron density near the anode plate and less electron density near the cathode plate. The total electron density inside the chamber is less than the ion density [6].

2.2. Pulsed shape

When a high energy photon passes through the detector it will ionize the gas and produce an electron ion pair. As soon as the charged particle reaches the chamber electrode, a pulsed signal is generated which can be measured with external readout electronic circuits.

The simple geometry of a parallel plate detector is shown in Fig (2-1). This simple geometry is used to discuss the signal-pulsed shape produced in the ionization chamber. The ionization particle moves through the chamber in different positions and produces electron ion pairs.

For a relatively long collection time, the movement and the collection process can be divided into two parts: first the movement and collection of the electrons and secondly, the movement and collection of the positive ions.

The mean drift velocity for the electrons and ions is proportional to the electric field and inversely proportional to the gas pressure as shown in Eq. (2-3) and (2-1). If the mobility of the ions has a value of 10^{-4} bar $V^{-1}s^{-1}$ when applying an electric field of 10^4 V/cm, a velocity of roughly 1 m/s is expected, provided that pressure is 1 atmosphere. This corresponds to a transit time of 5 ms across the full chamber width of 5 mm [7].

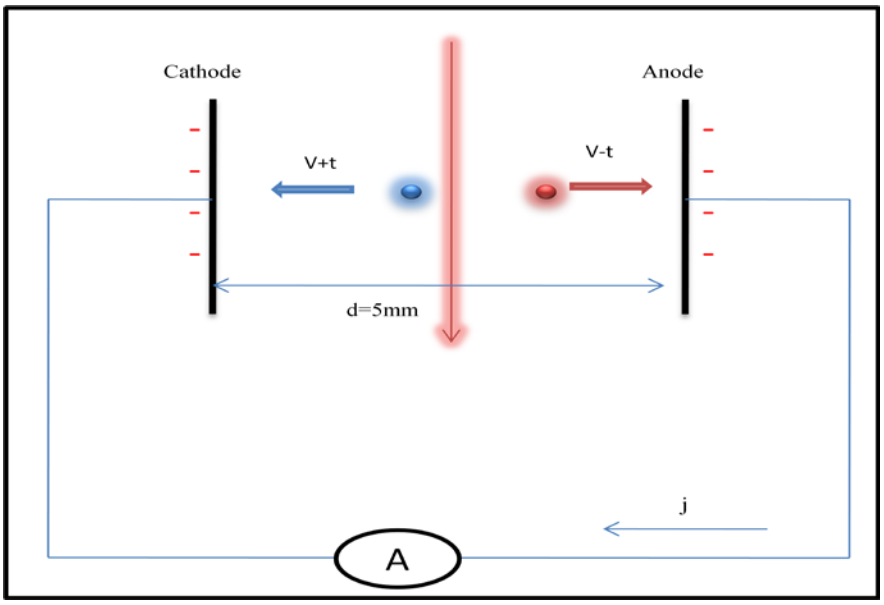

Figure 2-1: Simple parallel plate geometry which contains two electrodes separated by distance (*d*), the photon beam enters the chamber from different positions.

The fact that the mobility of the electron is much greater than the positive ion mobility is due to their mass difference, the electron's velocity is 1000 times greater than the velocity of the positive ions. Therefore, the electrons will reach the anode faster and they will be collected in a short time (a few microseconds). In contrast, the positive ions need longer to be collected (a few milliseconds).

After the electrons are collected they give no further contribution to the output signal. The rest of the signal is from the contribution of the slower positive ions

The pulse shape of the collected charges generated from a discrete photon in the ionization chamber plates is described in Fig (2-2). The initial rapid increase signal is due to the collection of the electrons. The positive ions, being slow, continue to reach the cathode as shown in part (2) followed by a long signal which is due to the collection of the slower positive ions, as shown in part (3).

Figure (2-2) illustrates three slopes which correspond to three classes of current flowing in the outer circuit. The rising part of the curves occurs when the electrons and positive ions are in motion. The first part labeled 1 in the figure is obtained from the contribution of both electrons and ions. When the electrons and positive ions are in motion they induce a current in the chamber plates which can be measured. The slope labeled (2) is due to electron motion only and the third part labeled (3) occurs when positive ions only, which have smaller magnitude, are in motion [7].

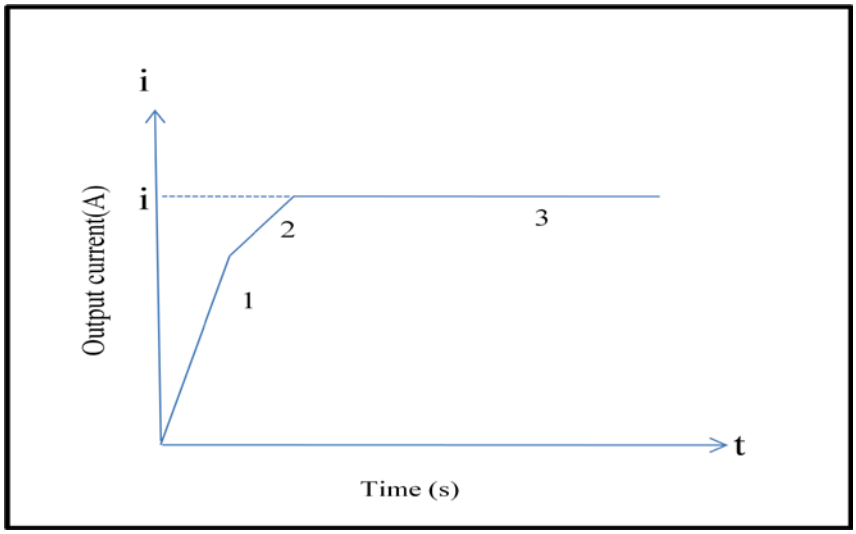

Figure 2-2: The expected pulse shape when an ionizing particle passes through a chamber far from the chamber plates. The full line (1) shows the initial signal till the electron are collected followed by the slower range as the positive ions moves towards the cathode (2) and (3).

Previous discussion indicates that the output signal depends mainly on the generated position of the charge carriers with respect to the chamber plates. Different pulse shapes can be obtained according to the position of the incident X-ray photon.

The various conditions in gas field detectors and the big difference between the electron and ion velocities makes it difficult to sketch the pulse shape accurately.

Three different pulse shapes are described according to the interaction position of the ionizing particle. In these cases it enters the detector from the side and parallel to the chamber plates. In addition, the velocity of the electrons is taken as roughly three times higher than the ion's velocity in the discussion [7].

2.2.1. The interaction position near the cathode

When the ionizing particle enters close to the cathode (negative electrode), the positive ions accumulate quickly. In this case it makes no contribution to the output signal pulse and the slope of the current results from the electrons alone, as shown in Fig (2-3) [7].

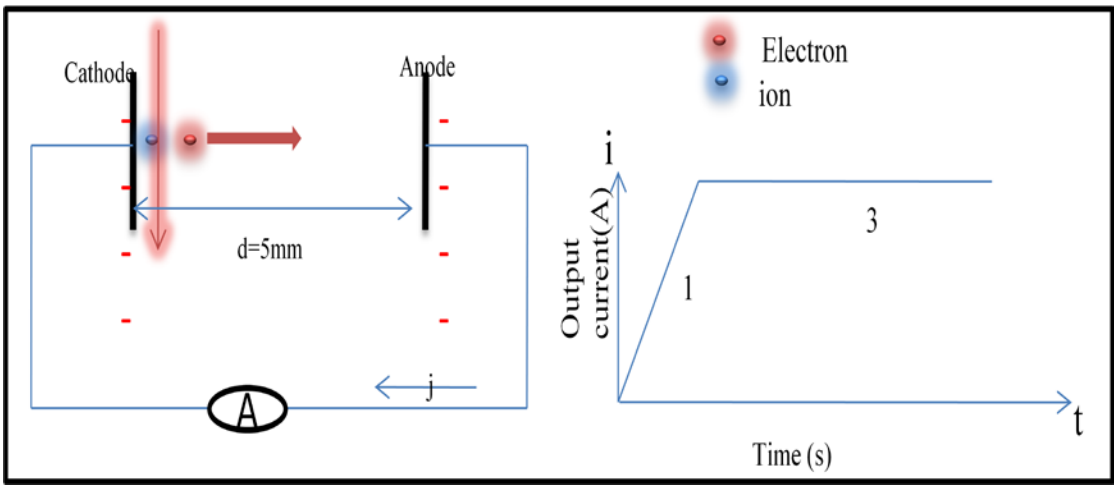

Figure 2-3: The ionizing particle enters the chamber near the cathode plate (left) and the corresponding pulsed signal (right).

2.2.2. The interaction position near the anode

When the ionizing particle enters the chamber close to the anode, the electrons are collected in a very short time. The pulsed shape is only due to the movement of the positive ions towards the cathode which has a slow rise time, seen in Fig (2-4) [7].

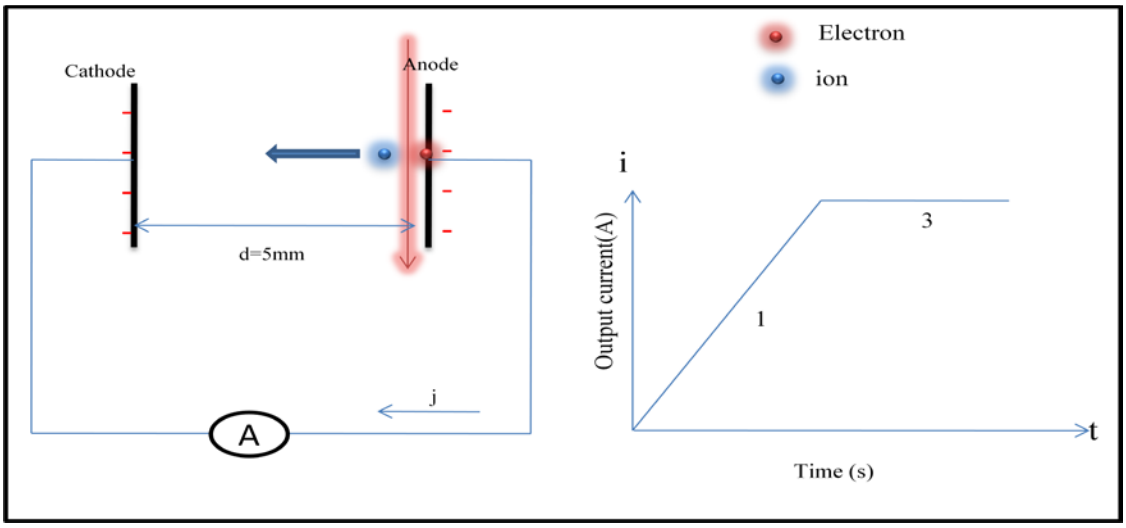

Figure 2-4: Sketch diagram shows the position of the entering ionizing particle near the anode plate (left) and the output pulsed signal (right).

2.2.3. The interaction position in the center

If the ionizing particle enters in the middle of the chamber, the electrons and the positive ions are both in motion until the electrons and ions are collected at the chamber electrodes. The pulsed shape will contain the contribution of both charge carriers as shown in Fig (2-5) [7].

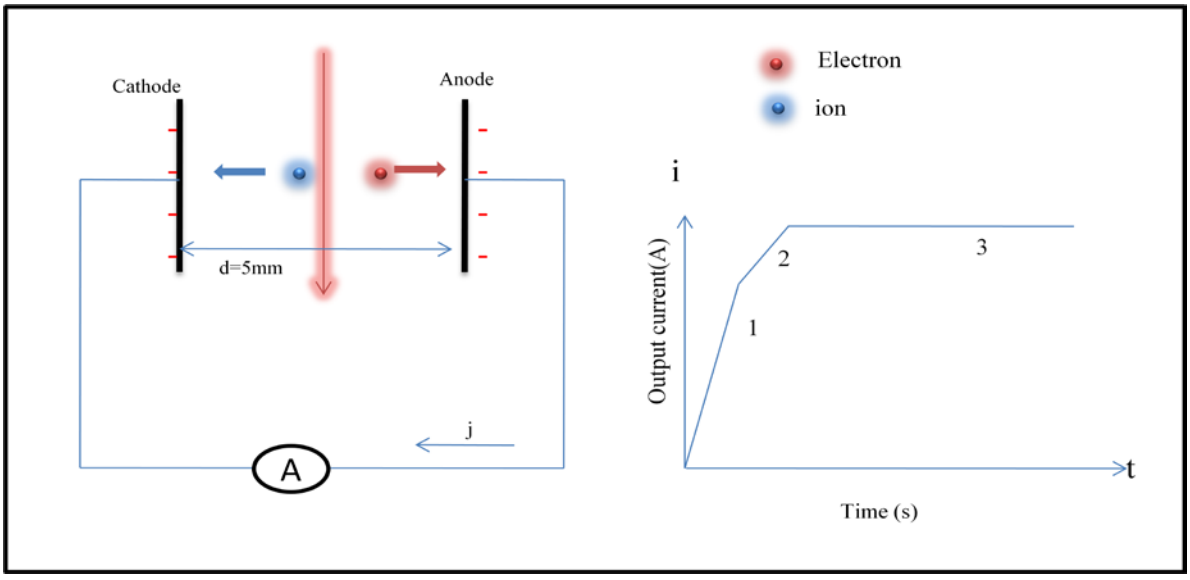

Figure 2-5: The ionizing particle entering the chamber in the middle of the plates left, the pulsed signal shows the contribution of both electrons and ions due to the movement towards the chamber plates.

Practically, when the ionization particle passes through the chamber it produces *N* number of electrons and ions. The movement of each charge carrier induces a pulsed signal in the

chamber readout electrodes and the total net collection of the charges produces a pulsed signal containing the contribution of all charges accumulated in the chamber plates.

2.3. Space charge effect

The distortion of the steady state electric field inside the ionization chamber according to the positive ions density ρ+ is called a space charge effect. The space charge distorts the uniform electric field E according to Poisson's equation given below:

$$\varepsilon \frac{\partial E}{\partial x} = \rho \tag{2-1}$$

Where ρ is the charge density; x is distance from the cathode and ε, permittivity [8]

2.3.1. Charge density distribution

The spread of the positive ions and electrons inside the ionization chamber depends on the applied electric field strength and direction. Boag (1950) studied the space charge effect in a parallel plate ionization chamber, taking into account the varying distribution of the positive and negative charges across the space between the plates of the ionization chamber, the total ionization is produced along the axis per unit time to get an accurate representation of the charge density distribution inside an ionization chamber formed by an X-ray pencil beam [9, 11].

In order to get an accurate representation of the charge density distribution in the sensitive volume, the variation in the charge distribution per time and space should be considered.

The model described by Boag (1969) assumes that the ionization produced is q. He assumes also that at all points in the gas between the plates, the space charge and recombination are negligible. The distribution of the positive charge density $\rho_+(x)$ which drifts with a constant mobility (μ_+) towards the cathode along the direction of the applied electric field E will rise from zero at the anode plate to a maximum of (Q_+d/μ_+E) at the cathode. On the other hand, the fast electrons will drift towards the anode in the opposite direction and the density $\rho_-(x)$ will have the same distribution in the opposite direction with a maximum of (Q_-d/μ_-E) at the anode plate. The steady-state distribution of the space charge can be calculated from the shape of the overlapping positive and negative charge distributions as shown in Fig (2-6) [10].

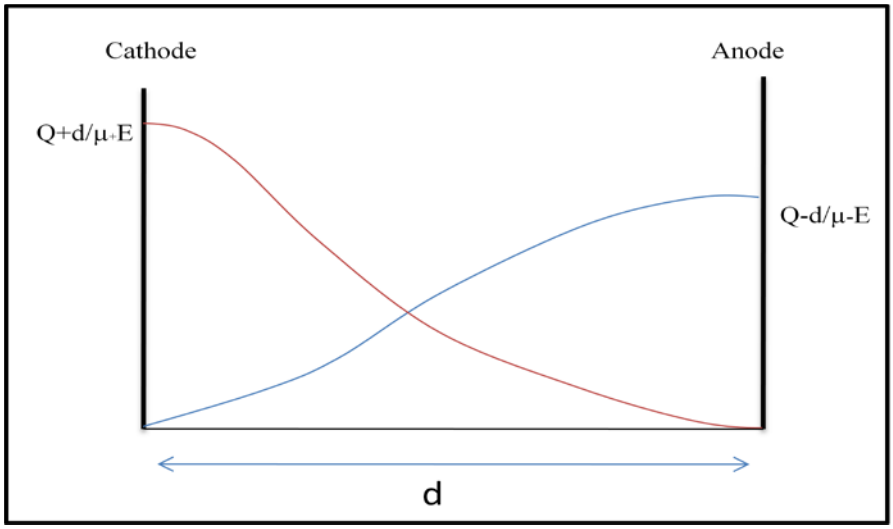

Figure 2-6: Boag illustration of the charge density distribution inside a parallel plate chamber, the positive ion density distribution is higher than the electron density distribution because of its slower velocity

The space charge depends mainly on the amount of free charges between the chamber plates and disturbance by the applied electric field which increases near the cathode plate and decreases near the anode plate.

2.3.2. Electric field distribution

The distribution of the applied electric field is assumed to be constant in the case of the steady state. However, the presence of the positive ions becomes relevant when the ionization chamber is illuminated with high photon intensity. The high photon rate will consequently generate positive space charge whose distribution interferes with the applied electric field and thus disturbs it.

In a one-dimensional description, the electric field depends on time and chamber depth (x). The change of the electric field E according to the space charge $\rho_+(x)$ is calculated using the following Gauss formula [12].

$$\frac{\partial E}{\partial x} = \frac{(\rho_+(x))}{\varepsilon_0} \tag{2-2}$$

Where ε_0 is the gas dielectric constant.

2.4. Drift velocity

Considering the case of isolated electron ion pairs created at some distance from the anode, in the presence of an externally applied electric field, the electrostatic force will move the charges from their original points towards the electrodes. The positive ion will drift toward the negative electrode in the direction of the conventional electric field, whereas the electrons will drift in the opposite direction towards the anode. The drift velocity of the positive ions is given by [13].

$$v_+ = \frac{dx}{dt} = \frac{\mu_+}{P} E = \frac{\mu_+}{P} \frac{V}{d} \tag{2-3}$$

Where μ_+ is ion mobility, v_+ positive ion drift velocity; d total distance; E electric field and V the applied voltage.

From Eq. (2-3), it was found out that the drift velocity is proportional to the electric field and inversely proportional to the gas pressure. The drift velocity per unit electric field divided by density is called the mobility, which remains constant for the positive ions because of their heavy mass.

The electrons have smaller mass than ions, which allow them to experience greater acceleration, typically 1000 times greater than the positive ion drift velocity in the same gas. The electron drift velocity is also dependent on the gas pressure P as shown in the following formula [13].

$$v(e) = \frac{dx}{dt} = \frac{\mu_{e(E)}}{P} E = \frac{\mu_{e(E)}}{P} \frac{V}{d} \tag{2-4}$$

Where $\mu_e(E)$ is electron mobility and $v_{(e)}$ electron drift velocity.

2.5. Recombination

The recombination loss is calculated in the ionization chamber using the electron ion density distribution in the sensitive volume. The theoretical model of recombination was completed by (Hübner (1958), Scott and Greening (1961) and Boag (1969)). Boag discussed the general recombination in a parallel plate ionization chamber near the saturation region by considering the varying distribution of electron-ion densities across the space between the chamber plates [10, 11].

The recombination and screening effect due to space charges are very small in the ionization chamber at low X-ray beam intensity and thus can be neglected. At high X-ray photon intensity, the effect of the positive ion contribution is very important.

The rate of recombination in the detector can be evaluated quantitatively by considering the positive ion density *(n+)* and the electron density *(n-)*, with α the recombination coefficient, as [12].

$$\frac{dn-}{dt} = -\alpha n^{+} n^{-} \tag{2-5}$$

Where the negative sign denotes the reduced number of charged particles with time.

This formula becomes

$$\frac{dn-}{dt} = \frac{dn+}{dt} \tag{2-6}$$

$$\frac{d(n^{-}-n^{+})}{dt} = 0 \tag{2-7}$$

After the integration, we get

$$n^{-} - n^{+} = c \tag{2-8}$$

If the electron density and ion density are equal then we get

$$\frac{dn}{dt} = -\alpha n^{2} \tag{2-9}$$

If recombination takes place during the time interval from $t=t_0$ to $t=t$, provided that the density of the charged particle at $t=t_0$ is n_0 , Eq. (2-7) gives::

$$n = \frac{n_0}{1+\alpha n_0 t} \tag{2-10}$$

After the separation and integration of Eq. (2-7), see appendix [B2]. And by using Boag's theory, the charges which escape the recombination are given by [11, 15].

$$n = \frac{\alpha c n_0 e^{-\alpha c\,(t-t_0)}}{(\alpha c + n_0(1-e^{-\alpha c\,(t-t_0)})} \tag{2-11}$$

Using $n^- - n^+ = c$ when $c \xrightarrow{\Delta} 0$

we get

$$n = \frac{n_0}{1+\alpha n_0 t} \tag{2-12}$$

2.6. Diffusion

The thermal motion of the gas atoms is characterized by the mean free bath, the positive ions and electrons which are created inside the active volume of the ionization chamber also move with random motion and diffuse away from the original position. The free electrons will spread from the original point in a Gaussian spatial distribution and the width will increase with time.

The Gaussian density distribution which describes the point-like charge cloud which begins to drift at time t=0 from the origin is given by [14].

$$n = \left(\frac{1}{\sqrt{4\pi Dt}}\right) exp\ \left(\frac{-r^2}{4Dt}\right) \tag{2-13}$$

Where $r^2 = x^2 + y^2 + (z - ut)^2$; with *D* a diffusion constant

The diffusion width is given by

$$\sigma^2 = \sqrt{2Dt} \tag{2-14}$$

σ is the standard deviation of the charge distribution; *t* is time

If *n* satisfy the continuity equation condition one can drive the diffusion constant by

$$D = \frac{2\varepsilon t}{3m} \tag{2-15}$$

Where ε is the electron energy; *t* average time between collisions and *m* electron mass

Using electron mobility which is given by

$$\mu = \frac{e}{m} t \tag{2-16}$$

From Eq. (2-15) and Eq. (2-16) we get

$$\varepsilon = \frac{3De}{2\mu} \tag{2-17}$$

For $\varepsilon = \frac{3}{2}kt$ Eq. (2-17) becomes

$$\frac{D}{\mu} = \frac{kt}{e} \tag{2-18}$$

Where *k* is the Boltzmann constant; μ mobility and *t* temperature

The diffusion width (σ) of an electron which has traveled over a distance *x* is given by [16]

$$\sigma^2 = 2Dt = \frac{2Dx}{\mu E} \tag{2-19}$$

$$\sigma = \sqrt{\frac{2Dx}{\mu E}}$$

Were *E* is electric field;

Since the positive ions have large masses compared to the electrons, the diffusion coefficient is much smaller than that of the electrons and the angular distribution is considered to be a magnified image around the cathode plate. Okuno (1979) calculated the avalanche distribution of the positive ions around the cathode and electrons around the anode wire in the proportional chamber, taking into account the space charge effect using Argon (90%) Methane (10%) mixture. The simplified formula from Okuno is:

$$\sigma^2 = 2\int_{x=0}^{x=d} \frac{D}{\mu}\,\frac{1}{E_x}\frac{1}{x}\,dx \tag{2-20}$$

Which gives the angular spread of an electron starting at x_0 and reaching the anode at x=x [16].

2.7. Repulsion

Electrostatic repulsion between charge particles is due to the Coulomb force. Considering many charge particles traveling in spherical cross section, Coulomb repulsion pushes the charged particle away from the center. Assuming that Q is the total charge inside the sphere, given by

$$Q(r,t) = q\int_0^r n(r,t)4\pi r^2 dr \tag{2-21}$$

Where *r* is the radius of the sphere and *Q* the total charge density

The dynamic of the electrons, according to electrostatic repulsion, described by:

$$\frac{\partial Q}{\partial t} + \left(\frac{\mu_e}{4\pi\varepsilon}\right)\frac{1}{r}\frac{\partial Q}{\partial r} = 0 \tag{2-22}$$

Where μ_e is electron mobility and ε permittivity

By separating the variables in Eq. (2-22) one gets

$$Q(r,t) = \frac{4\pi\varepsilon r^3}{3\mu_e t}[U(r) - U(r - r_0(t)) \tag{2-23}$$

where *U(r)* is the step function and $r_0(t)$ the limits of the repulsion size reached by the electron at time *t*.

The radius of the charge expansion according to Coulomb repulsion can be derived from Eq. (2-23) as follows:

$$r = \sqrt[3]{\left(\frac{3\mu_e q\ N\ t}{4\pi\varepsilon}\right)} \tag{2-24}$$

N is the total amount of charge from Eq. (2-21) and *q* is electron charge

This equation represents the change in repulsion with time if the amount of charge and mobility (*μ)* is known [17].

2.8. Signal formation

The movement of the charged particle in an electric field induces a signal on the detector electrodes. The surface charge can be calculated by solving the Poisson equation for the potential *φ* with a point charge *q* at *x= x₀* and the boundary condition *φ = 0*; at *x= 0*. From Gauss's law, the resulting electric field E=-∇Ø on the metal surface is related to the surface charge density σ by

$$\sigma(y,z) = \varepsilon_0\, E(y,z,x=0) \tag{2-25}$$

The solution of this particular geometry can be found by assuming a mirror charge *-q* at *x=-x₀.* The electric field on the metal surface is thus given by

$$E_x(y,z) = -\frac{qx_0}{2\pi\varepsilon_0\,(x^2+y^2+z^2)^{3/2}} \qquad E_y = E_z = 0 \tag{2-26}$$

For a moving charge in a trajectory *x (t),* the time-dependent induced charge on the electrode and the induced current is given by

$$Q_n^{ind} = \frac{q}{V} - \nabla\emptyset(x(t) \tag{2-27}$$

$$I_n^{ind} = \frac{dQ_n^{ind}}{dt} = \frac{q}{V} - \nabla\emptyset x(t)\frac{dx(t)}{dt} \quad (2\text{-}28)$$

$$I_n^{ind} = \frac{dQ_n^{ind}}{dt} = \frac{q}{V} Ex(t) \frac{dx(t)}{dt} \quad (2\text{-}29)$$

Where V is applied voltage, Ext=$-\nabla\emptyset x(t)$ the weighting function of the electrode, from Ramo's theorem [18].

The weighting field for the parallel plate detector is calculated by Riegler [19]. This is described by the following formula.

$$Ex(t) = \frac{V}{d} \quad (2\text{-}30)$$

Where d is the total distance between electrodes.

If the charge moves in trajectory $x(t)$ from position $x_0=x(0)$ to position $x_1=x(t_1)$, the total amount of charge Q_n^{ind} that flows between electrodes n and a ground is given by

$$Q_n^{ind} = \int_{t=0}^{t1} I_n^{ind} dt = \frac{1}{V}\int_{t=0}^{t1} q\, Ex(t)v(t)dt \quad (2\text{-}31)$$

Where $v_{(t)}$ is the drift velocity at time t and V the applied voltage between the two electrodes [14].

The output-induced current can be calculated by differentiation of the induced charge given by Eq. (2-31).

Chapter 3 Numerical simulation

3. Introduction

This chapter aims to explain the effect of the positive ions on the electric field inside the detector. The readout current and the influence of the physical parameters introduced in the previous chapter on the detection process. The numerical simulation is thus encoded and involves illuminating the ionization chamber with high synchrotron photon intensity.

3.1. Chamber geometry

The detector architecture illustrated in Fig (3-1) below of the ionization chamber is divided into two parts, each having 0.5 cm depth in the detector, both on the left and right sides. The anode is located in the middle of the detector and two cathodes are located on the left and right sides.

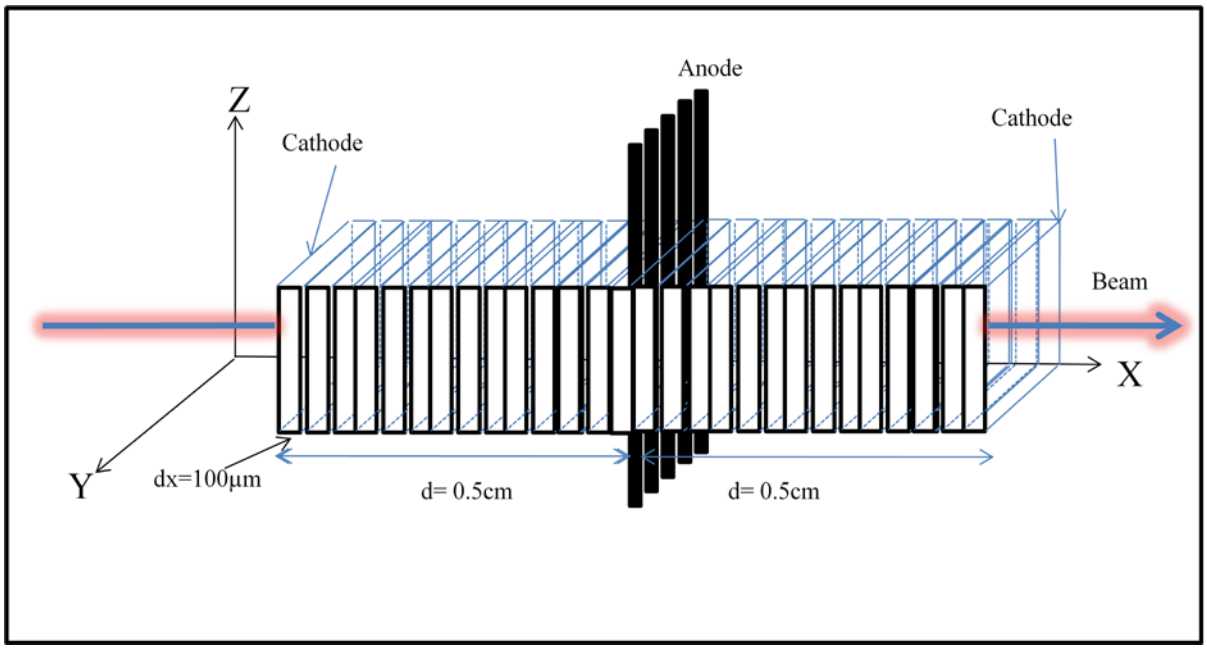

Figure 3-1: Sketch diagram shows the slab unit cross section *dx* on the *x*-axis where the total distance between plates is 0.5 cm. At the left and right sides are the cathode plates, and where the anode plate is in the middle is the sensitive volume which is divided into small bins.

In the simulation, the detector depth is divided into 50 bins. Each bin is 100 µm across. The simulation considers 2 ns bunch time for the incoming synchrotron photon flux as in BESSYII. The simulated synchrotron spectrum shown below is used to calculate the expected absorbed photons in the active volume.

3.2. Simulated synchrotron photon flux spectrum

Synchrotron radiation is generated when accelerating the electron bunch in the storage ring, which is an evacuated annular pipe.

Electrons are pre-accelerated in a linear accelerator and then injected into a straight section of the storage ring, then to the curved section through which the electrons are accelerated. The synchrotron radiation is produced either by the bending magnet which is needed to keep the electrons in a closed orbit, or by an insertion device such as a wiggler or an undulator. The loss of the accelerated electron's energy is emitted in the form of synchrotron radiation. Synchrotron radiation has a broad, continuous spectrum from infrared to hard X-ray. It is emitted from an accelerated charged particle inside the synchrotron ring at the bending magnets or (insertion devices) with high intensity and brilliance.

The spectrum is expressed in terms of photons per second per mm^2 of the source area per $mrad^2$ of the source angular divergence and per 0.1% of the emitted bandwidth.

The synchrotron spectrum from an EDR beam line in BESSYII is calculated in each case for the electron current of I= 200 mA. The photon rate is calculated with XOP software. In addition, the following assumptions were made:

1- The magnetic flux density of the bending magnet is 0.97 T.
2- The electron energy is 1.7 GeV.

The XOP software provides the number of primary photons per s. mrad 0.1% bw. The photon flux is converted to photons per s eV mm^2. The absorption of 1.2 m of air at the entrance to the carbon window of the chamber is calculated. The dead volume of the chamber at the width of 0.5 cm, and including the gas pressure inside the chamber is calculated, as shown in the following plots for both Argon and Nitrogen gases [20].
The full EDR spectrum shown in Fig (3-2) and Fig (3-3) is used in the simulation after the absorption of air, the carbon window and dead volume are corrected at pressures of 15 and 26 bar for Nitrogen and 5, 7 and 10 bar for Argon gas, which is used to simulate the space charge effect in the Multi-channel ionization chamber.

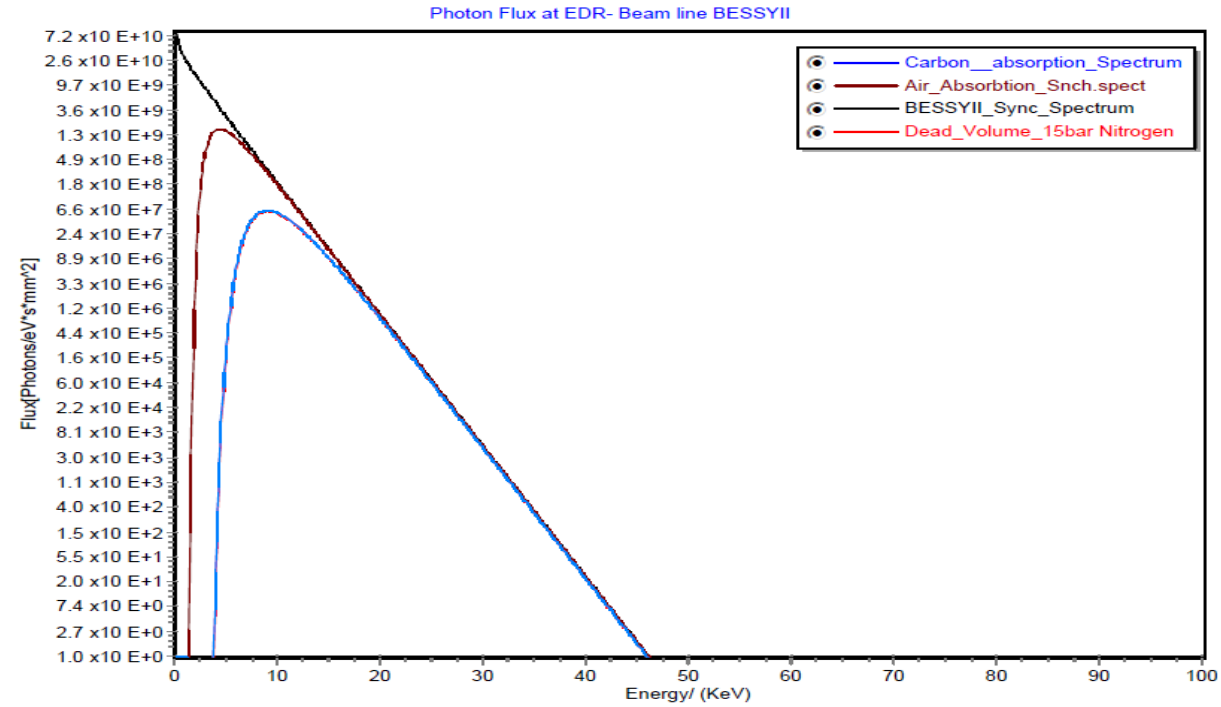

Figure 3-2: The expected photon flux per eV*s*mm^2 at 10 bar Nitrogen gas pressure are shown, with the beam from the bending magnet (Black) after absorption in 1.2 m Air in (brown beam) after absorption at the carbon window of the chamber (Blue), and the dead volume absorption of 10 bar Nitrogen gas with a volume of 7.5 cm^3 (Red).

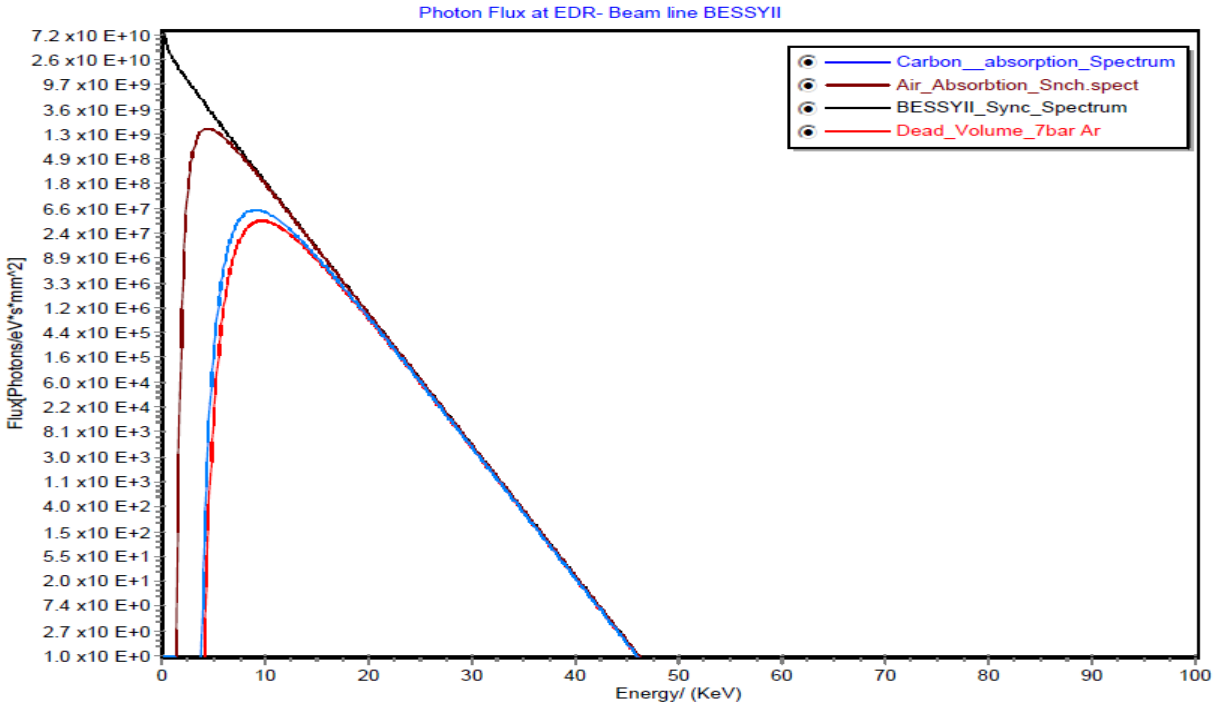

Figure 3-3: The expected photon flux per eV*s*mm^2 for Argon gas pressure at 7 bar, with the beam from the bending magnet (Black) after absorption in 1.2 m air (brown beam) after absorption at the carbon window of the chamber (Blue), and the dead volume absorption of 10 bar Argon-Methane gas mixture with a volume of 7.5 cm^3 (Red).

3.3. Absorption and calculation

The total number of absorbed photons in the active range of the gas is given by the following formula:

$$N_{abs} = N_0\left(1 - e^{-(\mu\rho x)}\right) \tag{3-1}$$

Where ρ *is* gas density, N_0 initial photon flux and x is depth in cm,

From the simulation of the synchrotron spectrum, each photon number with a certain energy bandwidth, as discussed above, is used to calculate the total number of electron ion pairs produced inside the chamber for the total detector volume using the following formula [21].

$$n_{e-ion} = \frac{eE_\gamma N_{abs}}{w} \tag{3-2}$$

Where e is electron charge, E_γ photon energy and w energy needed to create an electron ion pair; w = 36.6 for Nitrogen gas; w = 26.4 for Argon gas from table (3-1)

Assuming that there is no change in y and z directions and that the ions and electrons drift in the x direction only, we can divide the x-axis into small bins from $x=0$ at the cathode and $x=d$ at the anode as shown in the sketch diagram in Fig. (3-1). the total number of electron ion pairs in the small bin Δx is given by

$$n(e-ion)_{\Delta x} = \frac{eN_0E_\gamma\{(e^{-\mu\rho(\Delta x)i}) - (e^{-\mu\rho(\Delta x)_{i+1}})\}}{w} \tag{3-3}$$

The ion charge density ρ_+ is given by

$$\rho_+ = \frac{Q_+}{V} \tag{3-4}$$

Q_+ is the charge number; V is the volume.

3.4. Applied electric field

The following approximations have been made in order to calculate the electric field distribution inside the ionization chamber.

Approximation I:

The fluctuation of the synchrotron beam intensity is given in a percentage range and comes from many sources including the vibration of the monochromator.

The detector is designed to have a precision higher than the beam fluctuation for each pixel and to measure the change between the upper beam and the lower beam with a precision three times better than the photon statistics in each resolution element of the imaging Ge-detector (0.4 mm width).

Taken into account the time sequence the situation may be sketched as in Fig (3-4) below. Since the intensity changes in the MIC are slowly varying in time and space an estimate is generated for the beam intensity hitting the object and producing the modulated image in the Ge-detector. This allows to approximate the signal in the MIC by an extended in y-direction constant intensity and taking only the temporal changes into account. Therefore the simulation is restricted to this case.

It should be noted, however, that for the measurements at the synchrotron only a beam with rather small dimensions was available rather approximation a pencil beam. It will be discussed later, how this affects the conclusions.

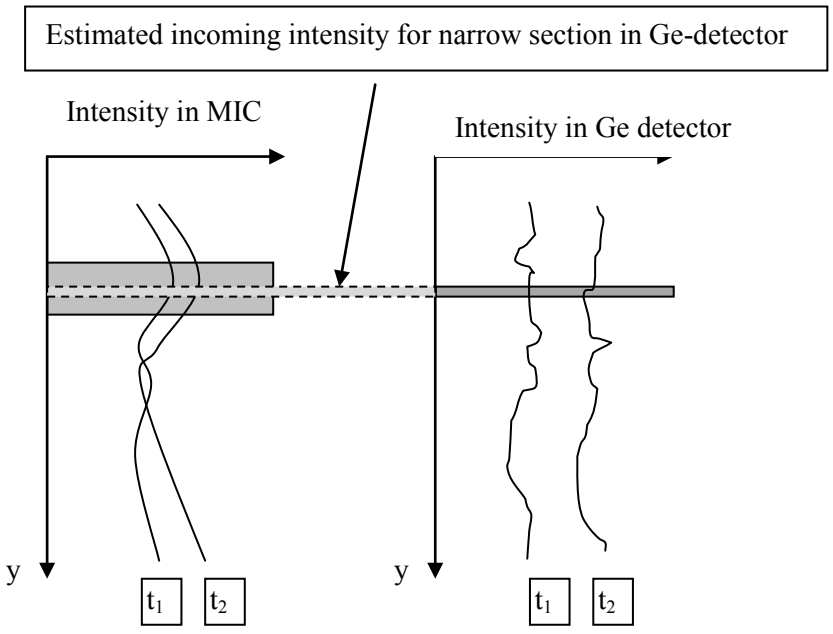

Figure 3-4: Sketch diagram showing the incoming beam intensity and the measured signal by the multi-ionization chamber and comparison of the expected signal from Germanium detector.

Assuming this, the field at any point of interest will have a component along the axis of symmetry. According to the radial symmetry of the ionization inside the chamber, the change is only in the depth direction according to the drift direction of the charge particle. By this

assumption, there is no change in the angular dependent. The radial dependent does not play an important role, while the ionization is only around the pencil beam and the mean of the radial value is taken into account in the calculation.

As the ionization spreads around the pencil beam, the non-uniformity of the electric field, according to the space charge effect will be at the central region of the ionization and surrounded by a uniform electric field. Considering the recombination effect, which is a rapid process, left over are only the slow ions. This also allows using this approximation for the pencil beam situation of the test beam, except with the slowly drifting ions in the tail of the signal.

The total distance in the x-direction is 5 mm, divided into 100 μm bin size and the applied high voltage is U_0. Assuming that the initial value E_0 is variable at $x=0$, we can calculate the difference of the electric field on each surface of each bin from Gauss's law and Maxwell's equation, as follows:

$$\nabla E = \frac{\rho}{\varepsilon_0} \tag{3-5}$$

$$\oint E\, da = \iiint \frac{\rho}{\varepsilon_0}\, dydzdx \tag{3-6}$$

If there is no change in the y and z directions and the change is in the x-direction only, then Eq.(2-6) becomes:

$$E.A = \frac{A}{\varepsilon_0}\int_{x=0}^{d} \rho(x)dx \tag{3-7}$$

The electric field difference at each surface of bin dx is given by

$$\Delta E = \frac{\rho(x)}{\varepsilon_0}dx \tag{3-8}$$

The applied high voltage is known and the total distance d is a constant value. Thus the total electric field inside the active volume can be calculated, taking into account that the electrons and ions drift, and calculating the recombination, repulsion and diffusion process each time. With the first bunch shot with homogenous illumination by an X-ray beam at time $t= 0$, and assuming that the positive ions concentration is constant gives

$$\int_0^d E dx = U_0 \tag{3-9}$$

Assuming that the mean value of the applied electric field is constant throughout the chamber depth at time $t=0$, using the computer simulation we get a value for E_0 by iteration, (more detail in appendix B1). The simulated distribution of the electric field throughout the chamber depth is shown in Fig (3-5).

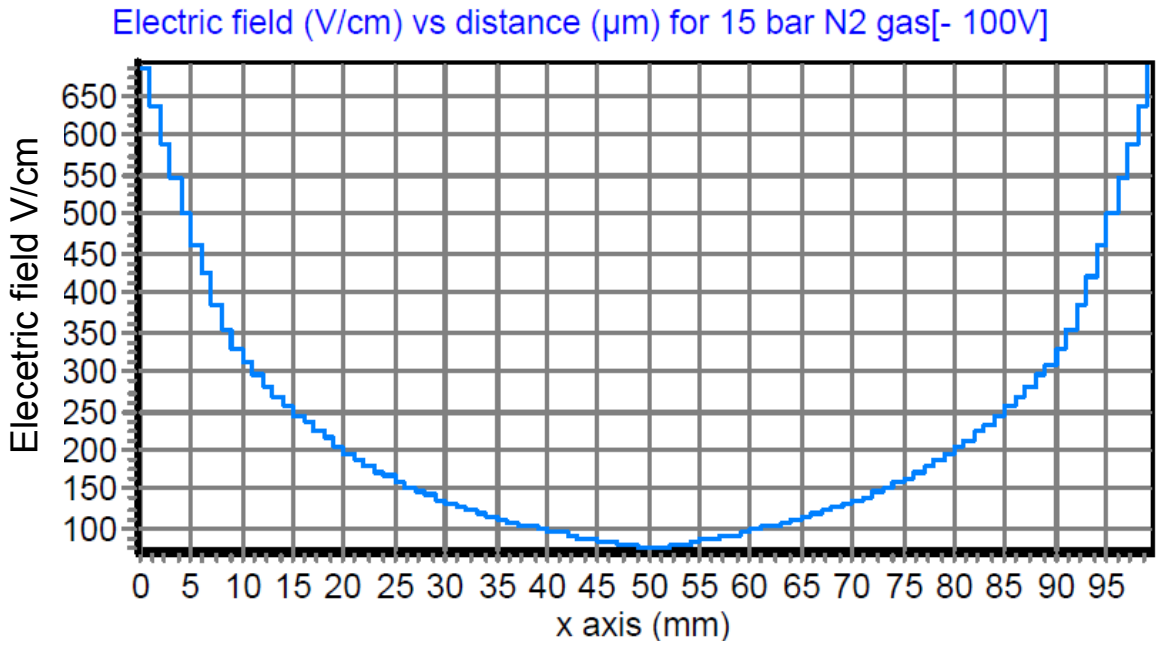

Figure 3-5: Electric field distribution inside the chamber, showing the change according to the surrounding space charge; simulation at 15 bar Nitrogen gas applying an electric field of 200 V/cm.

3.5. Drift velocity of electrons

In some gas mixtures such as Argon-Methane, the electron drift velocity approaches its maximum value in an intense electric field and a saturation effect is observed. Increasing the applied electric field slightly decreases the electron drift velocity. Fraser (1986) represents a Monte Carlo simulation with measurements of the electron drift velocity in a 90% Argon, 10% Methane mixture. The values of electron mobility in this given Argon-Methane gas mixture are derived from simulation and measurement [22]; the drift velocity as a function of applied electric field is shown in Fig (3-6).

The electron mobility for Nitrogen gas is shown in [13], the drift velocity as a function of applied electric field is shown in Fig (3-7).

The values of electron and ion mobility and the photon energy needed to produce electron ion pairs used in the simulation for different gases is shown in Table (3-1) [23].

Table 3-1: The energy required to produce electron ion pairs and electron and ion mobility in the used gases. [leo. 1994], exp. data [Smirnov 1968 Elecki et al. 1975], [sauli 1977]. [V.Palladino, et al., IBL-3013(1974)].

Gas	μ- (electron mobility) (cm^2* bar/ V*s)	μ+(positive ion mobility) (cm^2* bar/ V*s)	W (energy to produce electron ion pair)(eV)
N_2	559.8	1.87	36.3
Ar	$4.39x10^2$	1.7	26.4
Xe	$1.33x10^3$	0.58	22.3

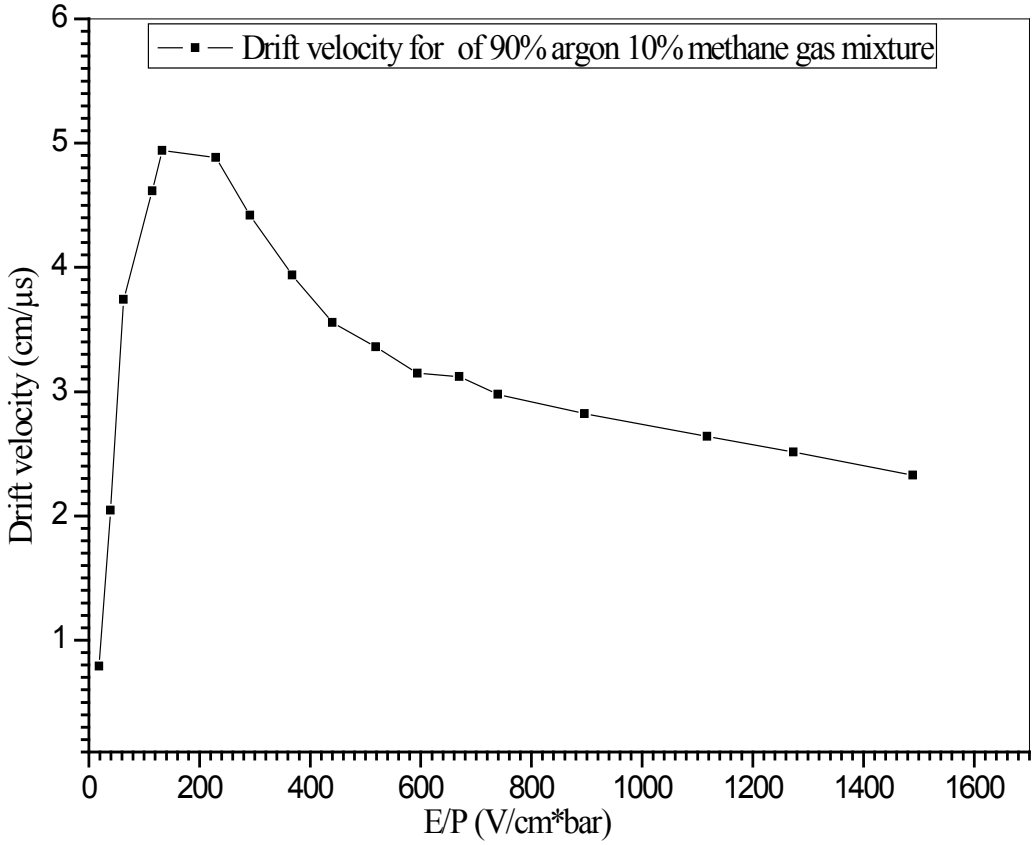

Figure 3-6: Measurement and calculation of electron drift velocity as a function of applied electric field in an Argon-Methane gas mixture of (90:10%).

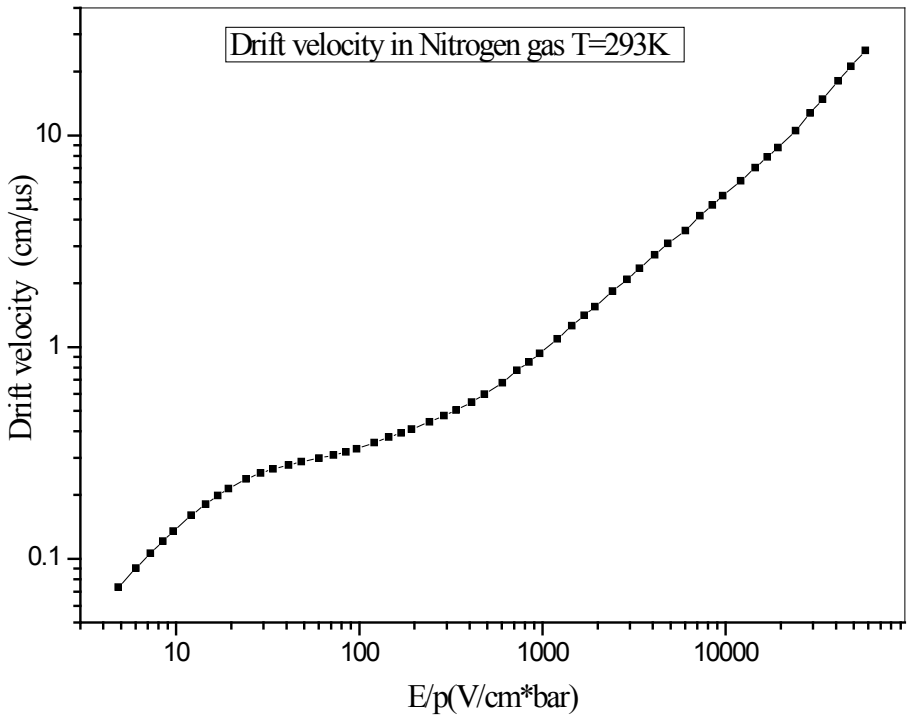

Figure 3-7: Measurement and calculation of electron drift velocity in Nitrogen gas as a function of applied electric field.

The simulated drift velocity of the electrons in Nitrogen gas uses the values of the mobility (µ) from Fig. (3-6) and using the simulated synchrotron spectrum shown before when applying high voltage of 100 V is shown in Fig (3-8).

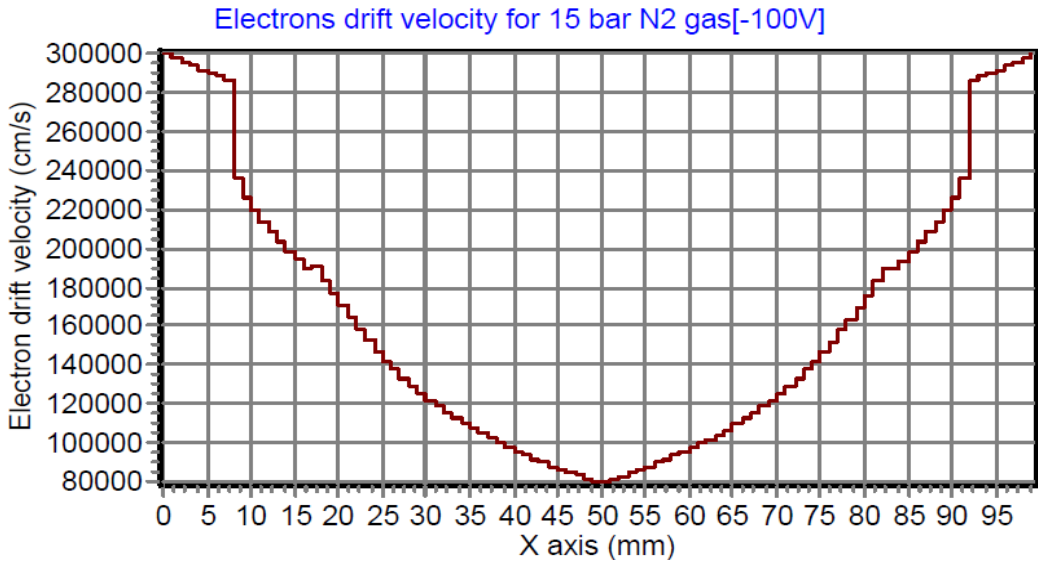

Figure 3-8: Electron drift velocity distributions inside the chamber, the drift velocity is higher near the cathode and slower near the anode, according to the electric field distribution. Simulation curve for 15 bar Nitrogen gas and an applied electric field of – 200 V/cm.

3.6. Drift velocity of ions

The behavior of ions is different from that of electrons because of their much larger mass. The simulated positive ion drift velocity distribution is shown in Fig (3-9) using the mobility value of 1.7 cm^2* bar/V*s for Nitrogen ion mobilities from table (3-1).

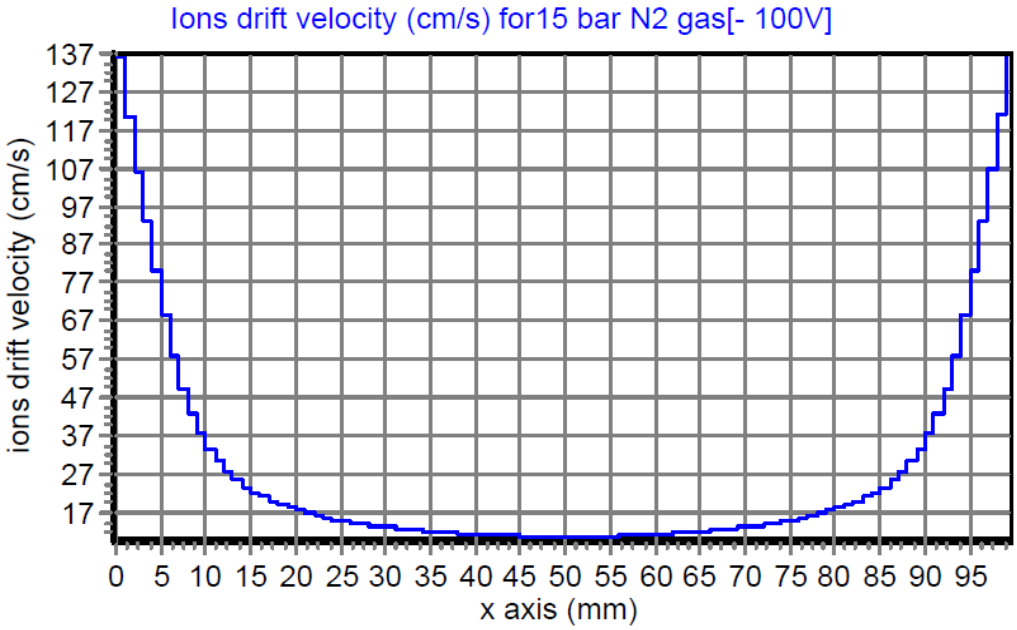

Figure 3-9: Positive ion drift velocity distributions inside the chamber, simulated with 15 bar Nitrogen gas and 200 V/cm applied electric field.

3.7. Charge movements

The charge movement inside the chamber, between the plates is simulated by dividing the total distance (d= 0.5 cm) into small bins. Each bin has a slab thickness of (Δx= 100 µm) and the unit area is perpendicular to the x-axis, as shown in Fig (3-1).

The electron ion densities vary with time according to the different drift velocities as discussed before. Therefore, the main part of the simulation is to obtain the change in charge densities as a function of time. The change of the electron ion densities within each slab is calculated by finding the difference between the numbers of electron entering the slab volume *(Δx)* and the number of electrons leaving the slab volume to the next slab volume towards the anode. The change in the ion number entering the slab volume *(Δx)* and the ion numbers leaving to the next slab volume *(Δx)* are calculated. Taking into consideration the left part of the detector geometry shown in Fig (3-1), the ions drift toward the cathode from right to left and electrons

drift towards the anode from left to right. This process is done by computer software which calculates the change in two nanosecond increments for all bin numbers [12].

Calculating the reference velocity for both ions and electrons is done with:

$$x = v * t \tag{3-10}$$

Where *x* is the distance in cm, v is velocity in cm/s and t is the time in seconds

$$v = \frac{x}{t} = \frac{100\mu m}{2ns} = \frac{100x10^{-4}\ cm}{2x10^{-9}\ s} = 5x10^{6}\ \text{cm/s} \tag{3-11}$$

The start of drifting of the electrons and ions which are created in the first bunch, and using the percentage of the electron drift velocity and the reference velocity, gives us the number of electrons that drift towards the anode and the number of ions drifting towards the cathode to the next bin. This procedure is done for all 50 bins. The remaining electrons and ions in each bin are summed up with the drifted one from the previous bin minus the recombined charges before and after drift.

After 2 nanoseconds comes the new bunch. This creates new electron and ion pairs in each bin. These are added to the existing number of electrons and ions in each bin. This procedure is repeated from the opening time of the chopper till it closed, as shown in the sketch diagram in Fig (3-10). After a certain amount of time the detector reaches the equilibrium state. This means that the number of newly generated electron and ion pairs are equal to the numbers of electrons and ions which disappear by recombination process and accumulate in the anode and cathode respectively, as shown in Fig (3-11).

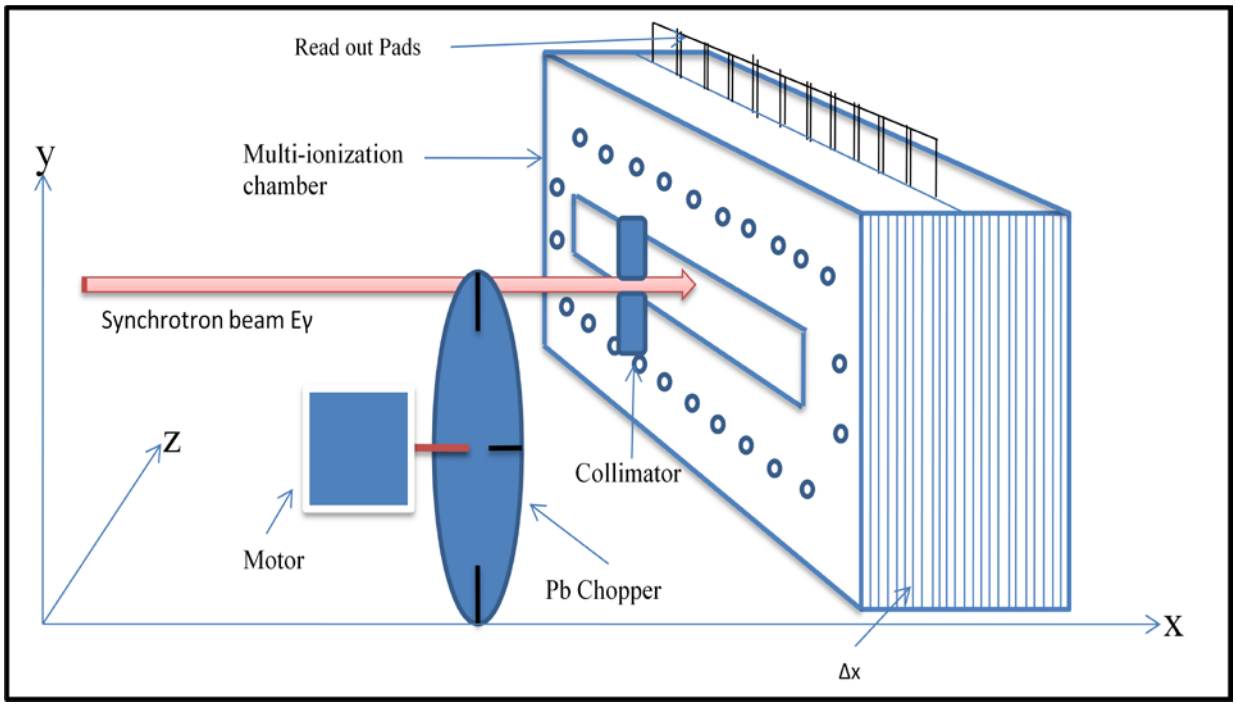

Figure 3-10: Sketch diagram showing the beam monitor divided into small values Δx of 100 µm in the x direction and the X-ray beam coming from left to right with energy $E\gamma$, the chopper is placed in between.

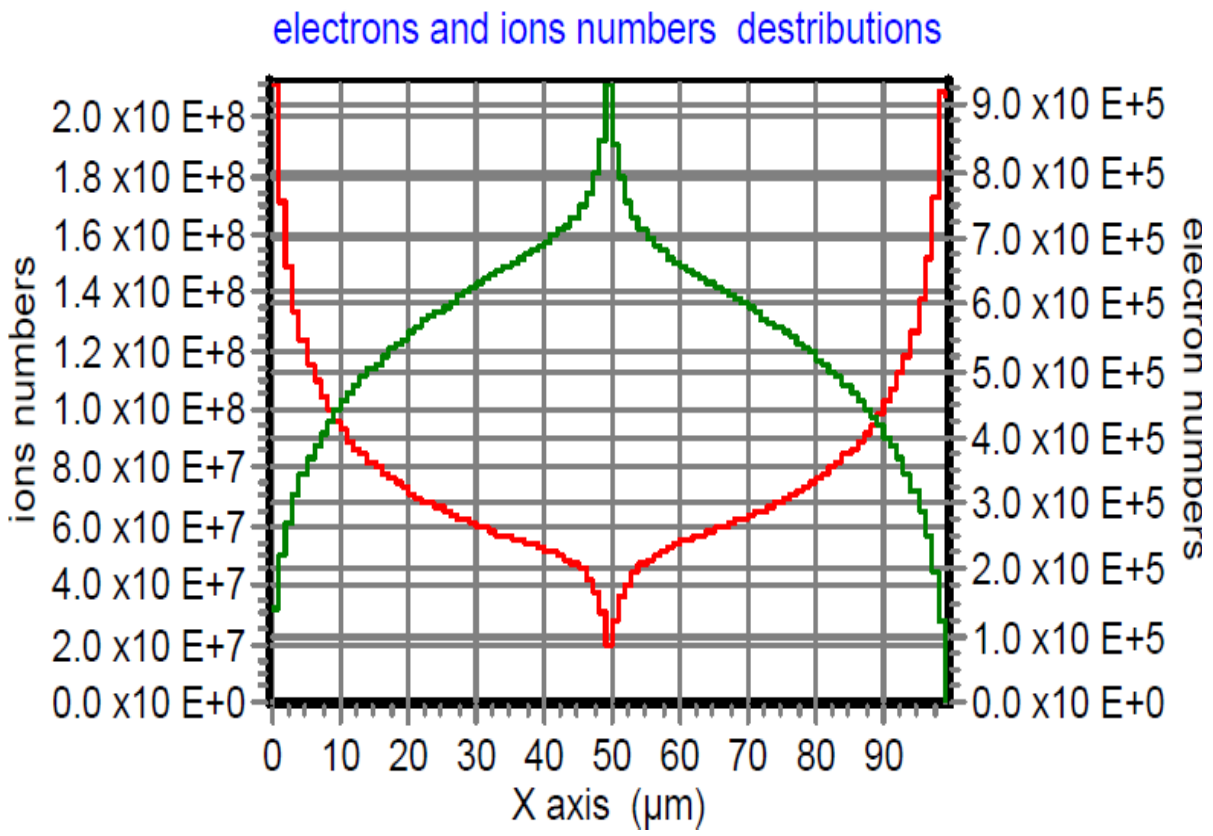

Figure 3-11: Simulated total number of electron (green) and ion (red) distribution inside the chamber while there is continuous illumination by synchrotron beam. For 15 bar Nitrogen gas, and using an applied electric field of -200 V/cm.

After closing the chopper there are no new photons hitting the ionization chamber, but the software keeps on running. After a certain amount of time all electrons disappear and only the remaining ions are drifting, as shown in Fig (3-12). At this time there is no recombination process and the charge is lost only by the accumulation on the cathode plate which delivers the long signal tail observed in the measured signal as shown in chapter 6.

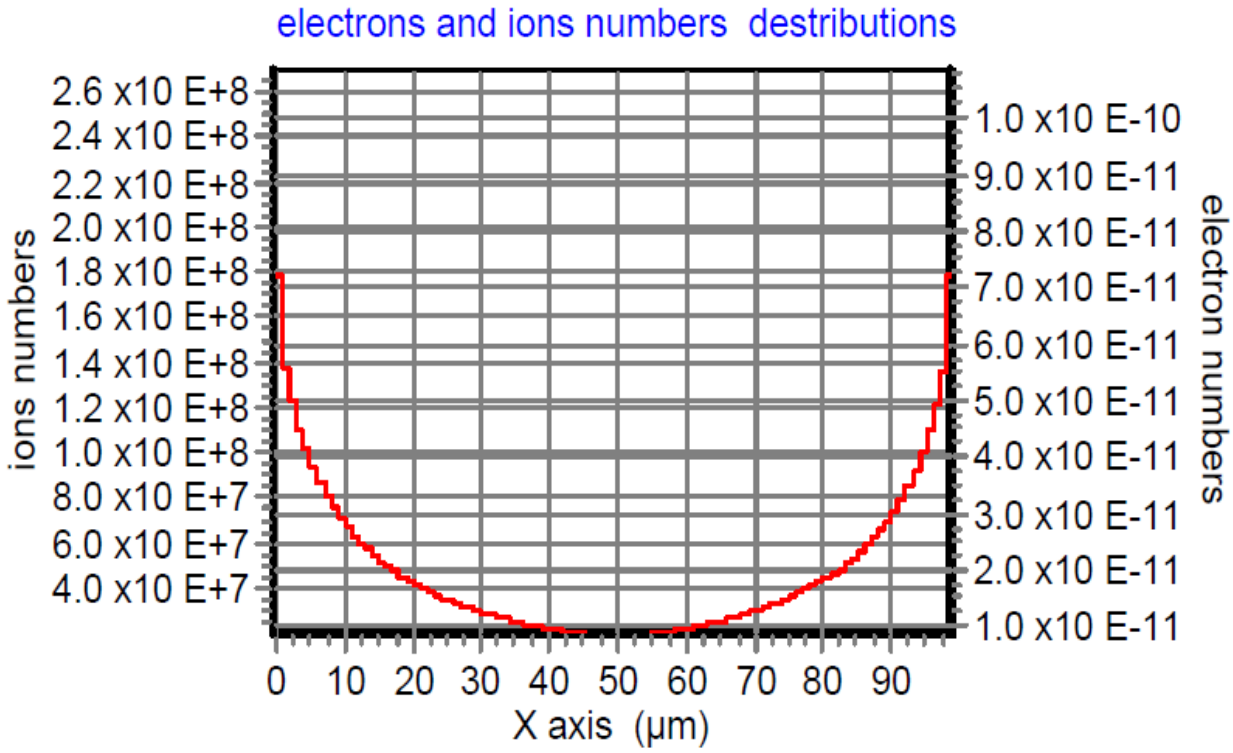

Figure 3-12: Electron and ion number distributions inside the chamber after the chopper has closed, we see only the contribution of the positive ions (red) increasing near the cathode and decreasing near the anode. The electron density is zero.

3.8. Recombination

Using Boag's formula for recombination in a parallel plate chamber and applying the boundary conditions, the recombination effect is calculated at 2 ns intervals before drift and before the new bunch arrives. Every 2 ns, a new number of electrons and ions which escaped recombination are calculated in each bin, and accordingly, the new electric field distribution inside the detector and drift velocities of electrons and ions are calculated with the information of drift velocities and the number of charges in each bin. The induced charges are calculated using Blum's formula, the output current is obtained by differentiating the induced charge. (Appendix B2).

3.9. Chopper system for the time resolved measurements

The beam chopping, with a rotating axis perpendicular to the beam axis, offers a short opening time and the beam is blocked during the closed cycle.

The chopper system for the time-response experiment with an X-ray beam from a synchrotron and an X-ray tube is described below.

The chopper consists of a lead disk with radius of 9 cm, 1 mm of lead and 3 mm of aluminum comprise its thickness and it contains 4 slits, each 1 mm wide, cut into the disk to increase the chopping frequency. A laser photodiode is placed on top of the chopper disk and connected to an Oscilloscope to measure the rotation speed. Another chopper is built with PMMA and also a radius of 9 cm, 4 mm thick and slits of 1 mm in four positions. The disk chopper is mounted on a drill machine which is connected to a stable power supply as shown in Fig (3-13).

The applied voltage has a linear proportional to the chopper frequency as shown in the measurement data in table (3-2) and Fig (3-14).

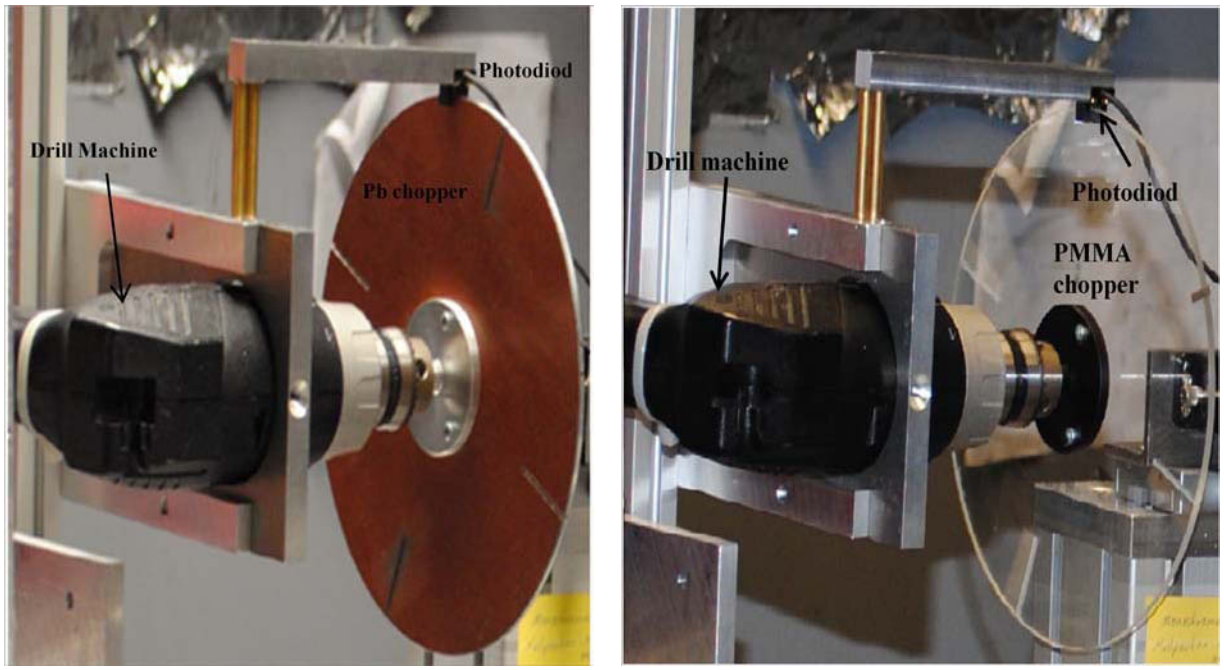

Figure 3-13: The lead disk chopper mounted to the drill machine and connected to the power supply left, the PMMA slit chopper right.

Table 3-2: The measured frequency as a function of applied voltage to the drill machine with Pb and PMMA disk choppers.

Applied voltage (Volt)	Pb slit chopper frequency (Hz)	PMMA slit chopper frequency (Hz)
2	7.06	7.18
3	11.062	11.49
4	15.598	15.726
5	19.602	20.216
9	34.48	34.48
10	37.4	37.79
12	46.72	46.72
14	52.64	53.56

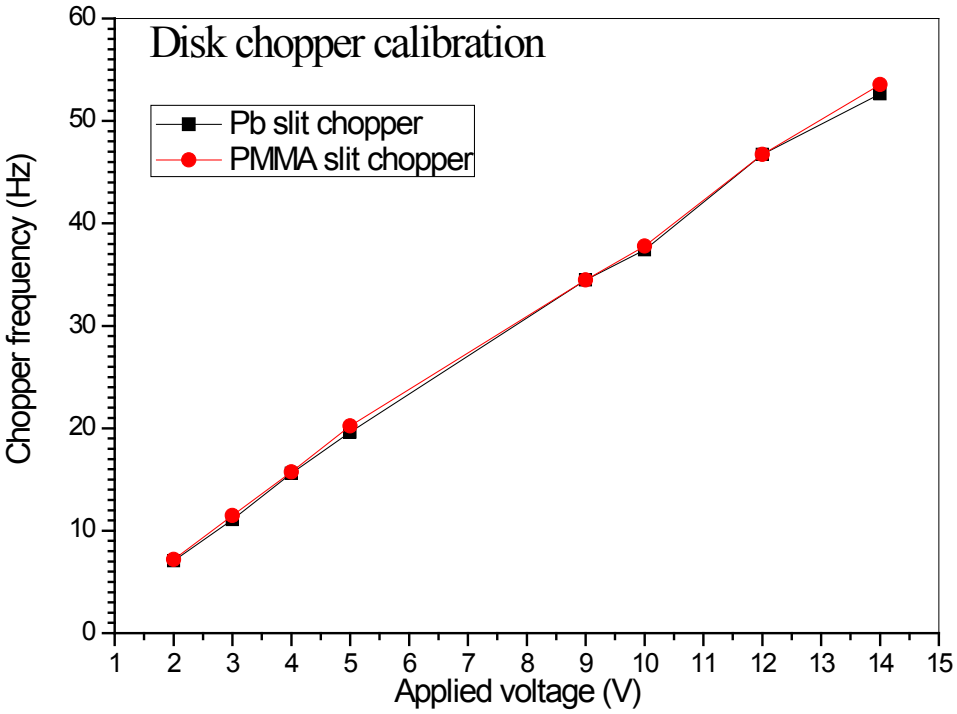

Figure 3-14: The calibration measurement of the applied voltage to the chopper, relative to chopper frequency.

The opening time t of a slit with a width of w for the chopper disk with radius r and rotating frequency f is given by [24].

$$t = \frac{w}{2\pi r f} \tag{3-12}$$

The opening profile of the chopper, for the time-response measurement uses a 0.2 mm vertical lead collimator in front of the detector, where the chopper slit is bigger than the collimator slit. The integrated intensity of the incoming beam profile corresponds to a trapezoidal opening in the chopper. During the open time, the slit open area increases and more photon flux enters the detector till it is wide open for a while and then starts to close with the same function as opening. The slit closes with time till it cuts the beam. Calculated integrated intensity of the simulated synchrotron beam spectrum for close/open/close cycle is shown in Fig (3-15) below.

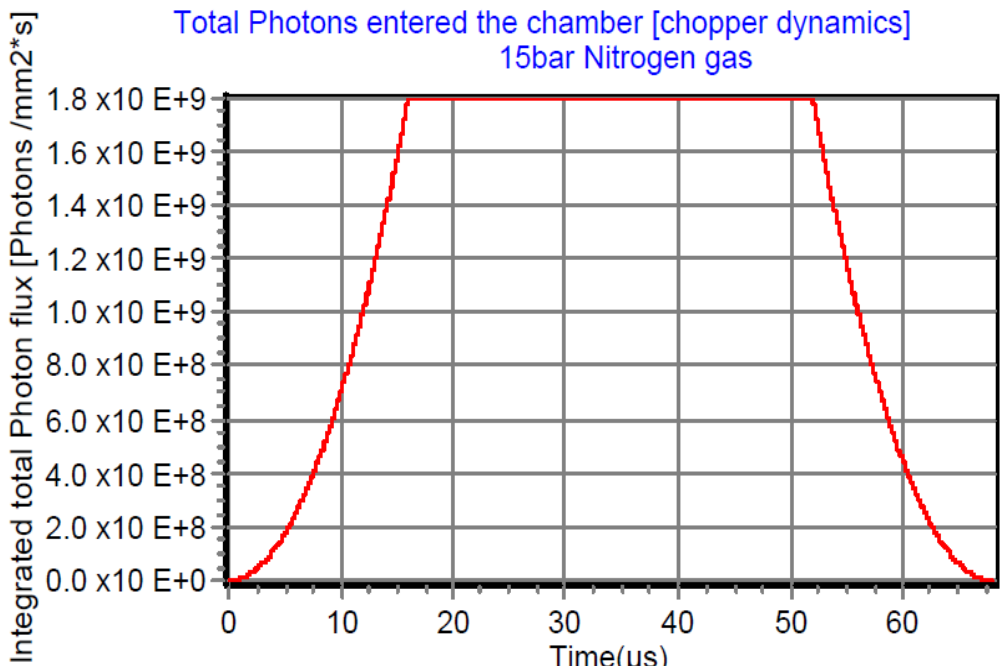

Figure 3-15: The simulated total integrated photons flux shown in Fig (3-2) that enters the chamber for 15 bar Nitrogen gas during the close/open/close cycle of the chopper.

A trapezoidal function is mathematically defined by a lower limit ***a***, an upper limit ***d***, a lower support limit ***b***, and an upper support limit ***c,*** as shown in the sketch diagram in Fig (3-16) below, where ($a < b < c < d$) from Eq. (3-13).

$$f(x) = \begin{cases} 0 & (x < a)\ or\ (x > b) \\ \frac{x-a}{b-a} & a \le x \le b \\ 1 & b \le x \le c \\ \frac{d-x}{d-c} & c \le x \le d \end{cases} \quad (3\text{-}13)$$

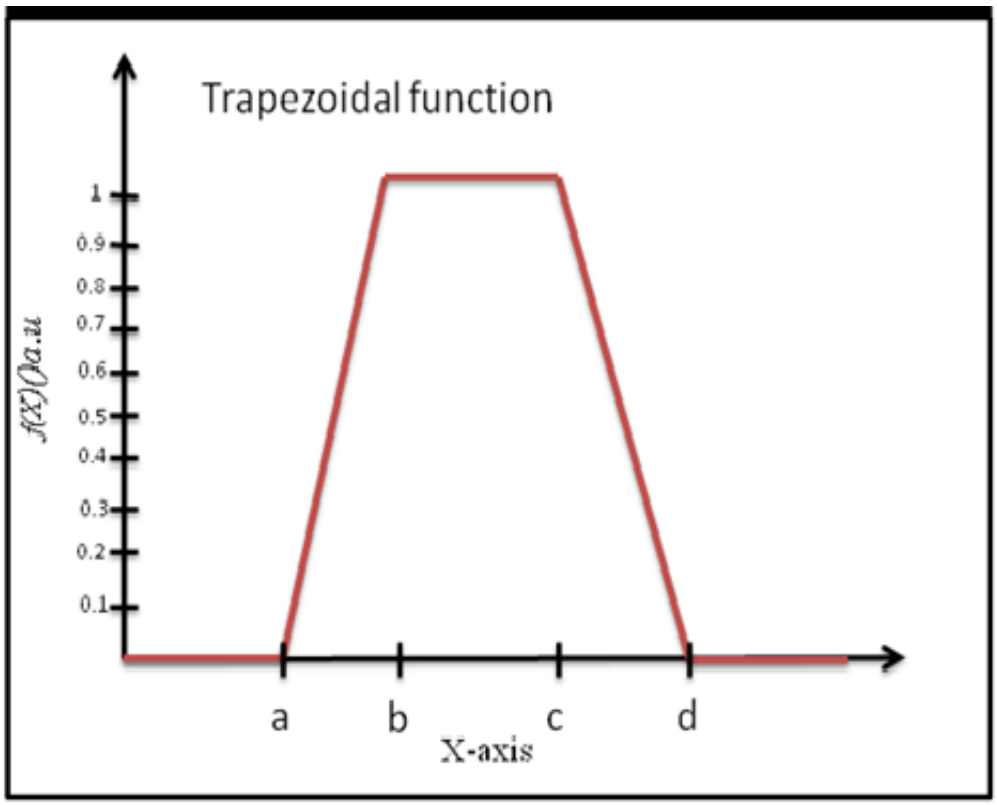

Figure 3-16: The trapezoidal function sketch diagram from Eq. (3-13).

3.10. Simulated output signal

The output signal is obtained by the induced charge formula described in chapter 2. As the simulation program runs each 2 ns, the induced charge is calculated by Eq. (2-31) and integrated till the end of the program, as shown in Fig (3-17) below.

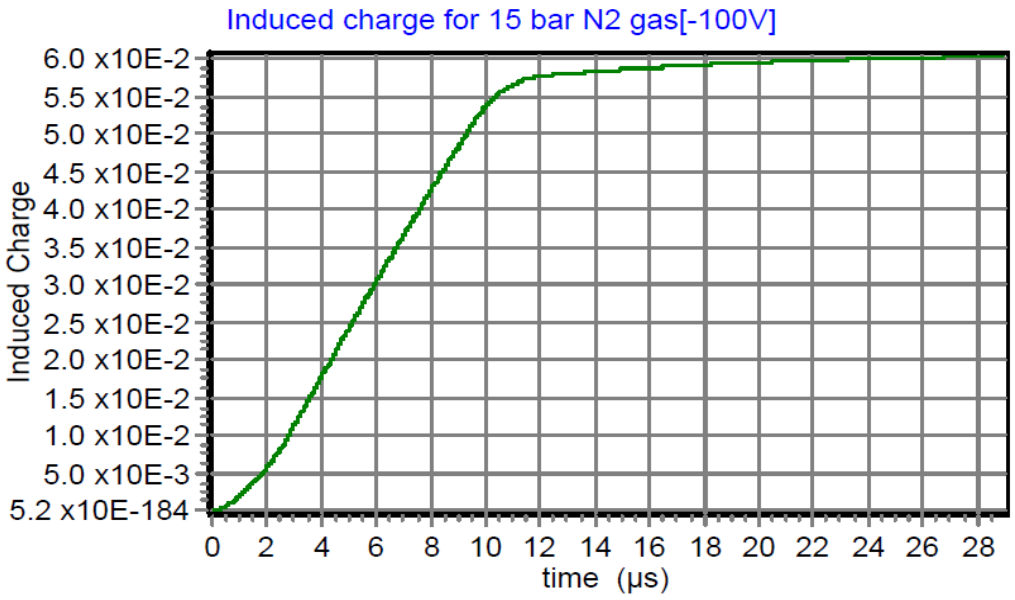

Figure 3-17: Induced charge of the total charges inside the chamber volume on the cathode and anode plate, for 15 bar Nitrogen gas and applying an electric field of -200 V/cm.

The induced current is given by differentiating the induced charge given by Eq. (2-31) in chapter 2. This is described by the following formula [14].

$$i_{ind} = \frac{d\, Q_n^{ind}}{dt} \tag{3-14}$$

The simulated induced current assumes an ideal chopper setting, opened to maximum in a very short time, leading to a high signal speed which decreases when the chopper closes to zero, as shown in Fig (3-18)

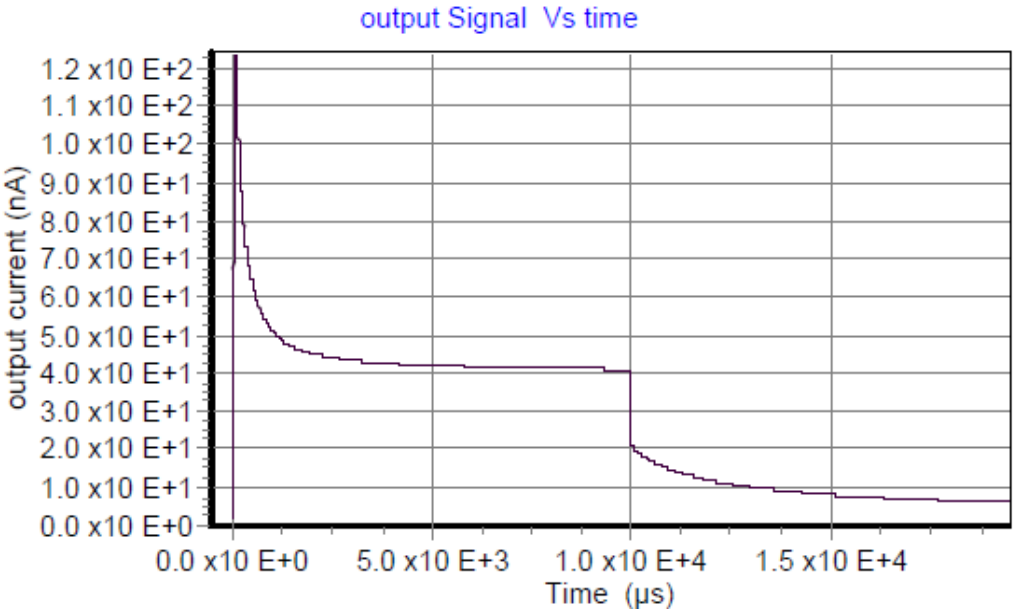

Figure 3-18: The output induced current simulated by assuming that ideal chopper opening to maximum at time t = 0.

The simulated output current signal, using the chopper as described before, and applying a trapezoidal function for the close/open/close cycles, and by differentiating the induced charge shown in Fig (3-16), the induced current is obtained for 15 bar Nitrogen gas with an applied electric field of -200 V/cm using a chopper frequency of 36.5 Hz is shown in Fig (3-19).

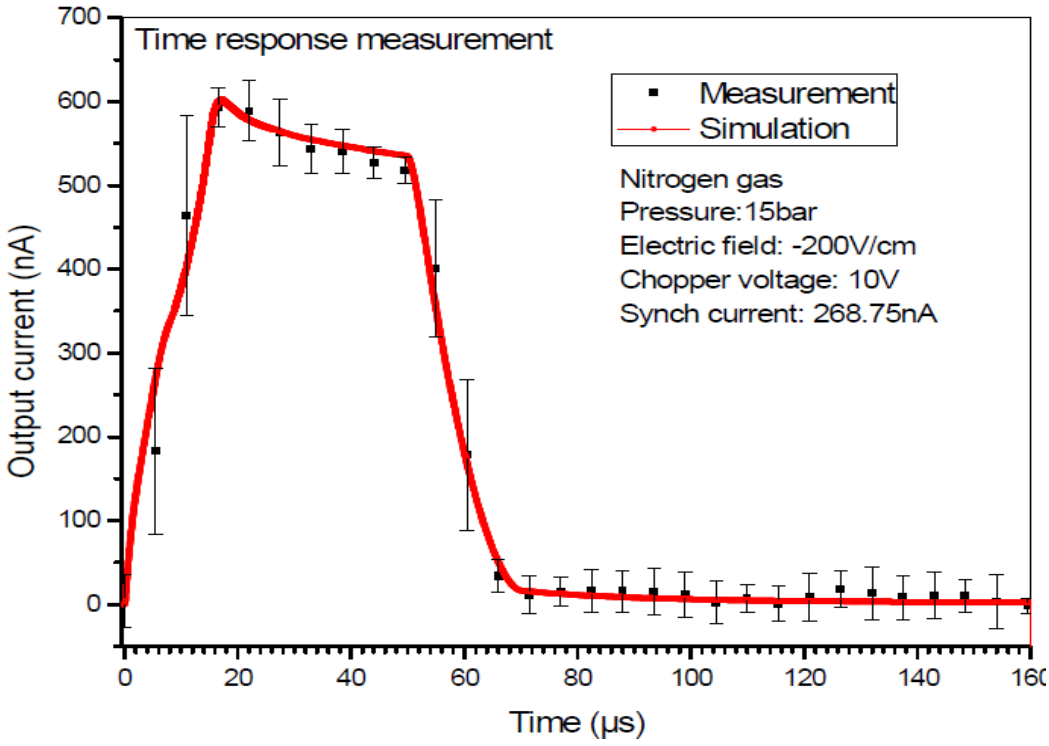

Figure 3-19: Simulated output induced current showing a fast response signal in the ionization chamber, obtained by differentiation of the induced charge shown in Fig (3-16)

3.11. Simulation flowchart:

The numerical simulation flowchart used to simulate the time response signal and the space charge effect explained in this chapter is described in detail below.

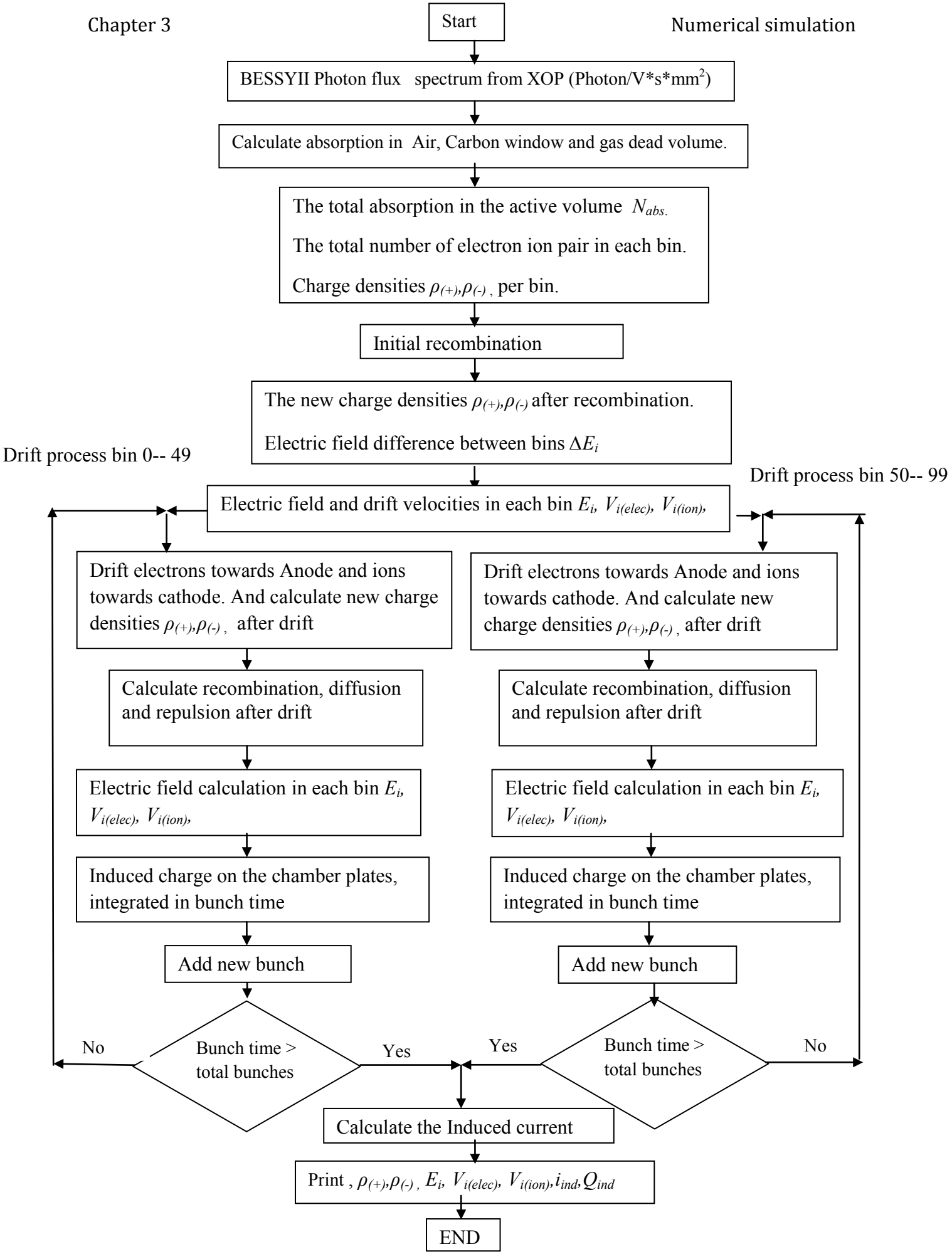
Start
BESSYII Photon flux spectrum from XOP (Photon/V*s*mm^2)
Calculate absorption in Air, Carbon window and gas dead volume.
The total absorption in the active volume $N_{abs.}$
The total number of electron ion pair in each bin.
Charge densities $\rho_{(+)},\rho_{(-)}$, per bin.
Initial recombination
The new charge densities $\rho_{(+)},\rho_{(-)}$ after recombination.
Electric field difference between bins ΔE_i
Drift process bin 0-- 49
Drift process bin 50-- 99
Electric field and drift velocities in each bin E_i, $V_{i(elec)}$, $V_{i(ion)}$,
Drift electrons towards Anode and ions towards cathode. And calculate new charge densities $\rho_{(+)},\rho_{(-)}$, after drift
Drift electrons towards Anode and ions towards cathode. And calculate new charge densities $\rho_{(+)},\rho_{(-)}$, after drift
Calculate recombination, diffusion and repulsion after drift
Calculate recombination, diffusion and repulsion after drift
Electric field calculation in each bin E_i, $V_{i(elec)}$, $V_{i(ion)}$,
Electric field calculation in each bin E_i, $V_{i(elec)}$, $V_{i(ion)}$,
Induced charge on the chamber plates, integrated in bunch time
Induced charge on the chamber plates, integrated in bunch time
Add new bunch
Add new bunch
No
Bunch time > total bunches
Yes
Yes
Bunch time > total bunches
No
Calculate the Induced current
Print , $\rho_{(+)},\rho_{(-)}$, E_i, $V_{i(elec)}$, $V_{i(ion)}$, i_{ind}, Q_{ind}
END

Chapter 4 Chamber design

4. Introduction

In this chapter the multi-channel ionization chamber construction and electronic design is described in detail, followed by the electronic noise and calibration measurement results.

4.1. The Multi-channel ionization chamber design

The multi-channel ionization chamber is designed in such a way as not absorb more than 1% of the incoming synchrotron beam. The chamber is divided into two parts by the anode strip, each part is of 0.5 cm depth to decrease the collection time of positive ions as shown in Fig. (4-1). It consists of an aluminum cover (1) with a 1 cm deep. 6 mm wide threaded with Helicoil to stand the high pressure of up to 30 bar and uses 6 mm steel screws. The second part is a 1 mm thick carbon-fiber plate (2). These light-conductive windows allow raising the gas pressure beyond 30 bar, the cathode (3) is made from a thin layer of aluminum foil, 13 μm thick (6) on a polyimide layer (polyimide 35E) as shown in Fig (4-2) [25]. The high voltage connection is made through two polyimide [27] layers (4) of 50 μm aluminum. As shown in Fig (4-3) a small hole (8) is made in one side for the high voltage connection to the strips on the ceramic with a resistance of 13 MΩ for the inner electric field and using inter-connecter NE [26]. The anode (5) is placed in the middle of the chamber as shown in Fig (4-1). The pressurized volume is sealed by a foil of Nova-press material [27]. The chamber is connected with a 3 mm diameter tube for gas input and output to decrease the differential pressure [28].

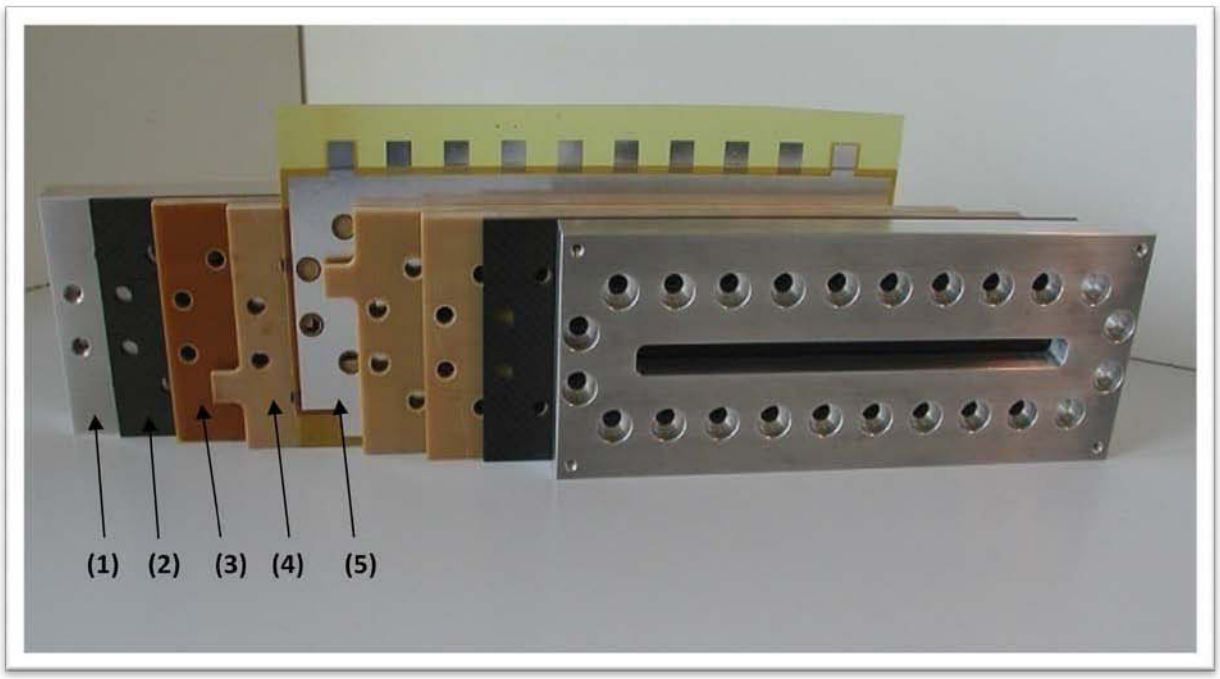

Figure 4-1: Photographs of the open chamber with a view of the anode and cathode details as well as the assembled detector

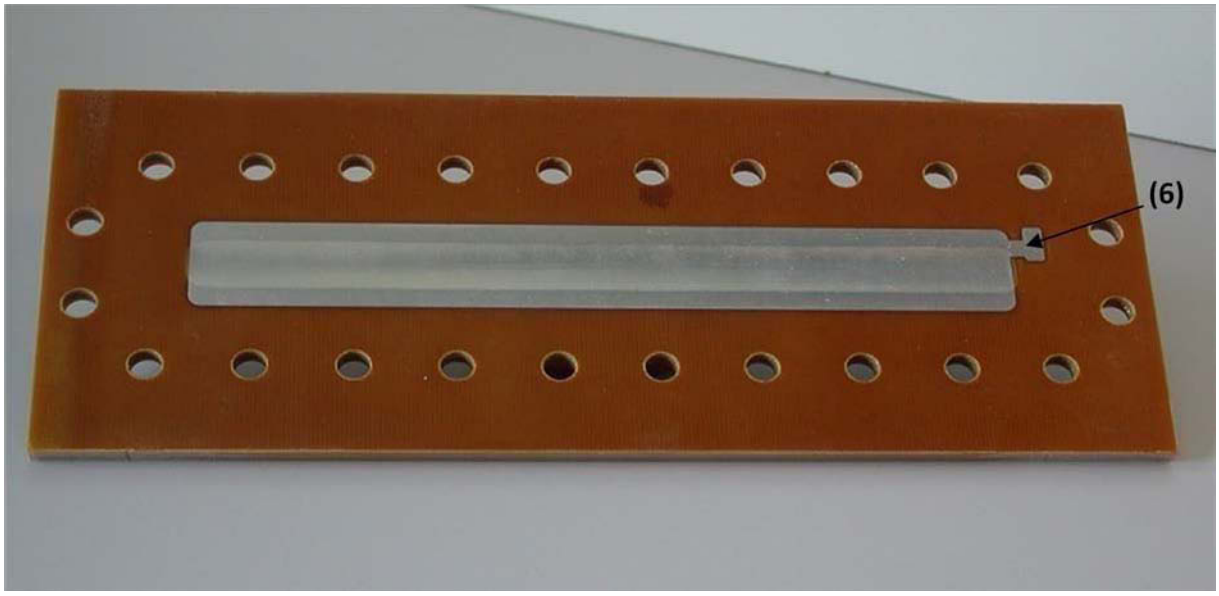

Figure 4-2: The design of the cathode (13 μm thick aluminum foil) for multi-channel ionization chamber construction.

Figure 4-3: High voltage connection for the multi-ionization chamber. High voltage contacts (7), feed through contact for the cathode (8) and Central electrode (9).

4.1.1. The anode

The anode contains different layers as shown in Fig (4-4) below. The first layer (10) from top to bottom is thin aluminum used as a guard ring. The careful implementation of guard rings has resulted in an effective isolation resistance of more than 10 MΩ to the high voltage (HV) electrode (cathode) on a polyimide layer with (e. glass) (11), the low flaw prepreg polyimide layer (12), another thin aluminum layer for the readout is divided into 16 readout panels (13), 8 upward and 8 downward lines each of size (4.5 x 17.8) mm^2. The space interval between the pads is 0.2 mm, and the space between rows is 1 mm.

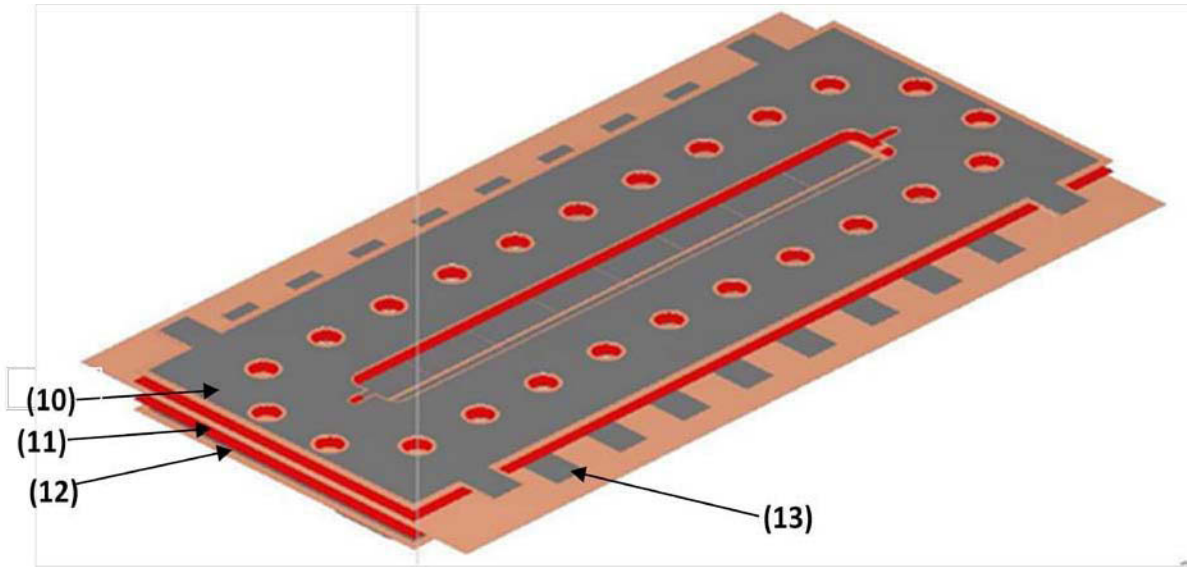

[a]

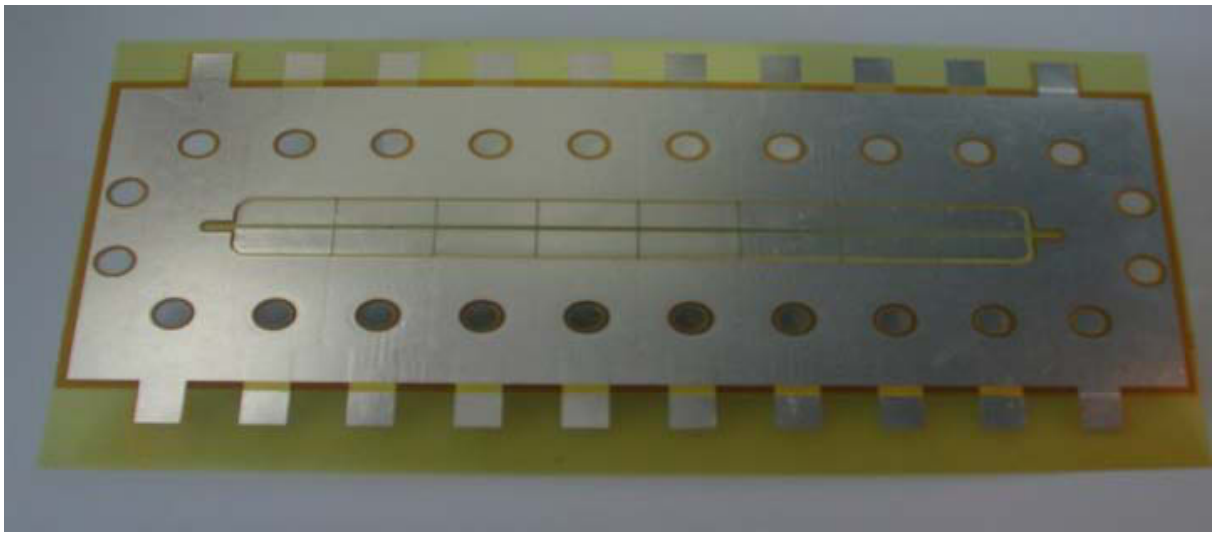

[b]

Figure 4-4: The anode sketch diagram showed the different layers design[a]. The anode photo [b].

4.1.2. Central electrode

The central electrode is a ceramic plate with a conductive strip built with a thick film processing technique. At the end of the strip is a resistive divider of 13 MΩ used to set the potential of the strip difference values for correcting the bending of the electric field lines. The central electrode separates the chamber into an upper and lower part see Fig (4-3), since there are two separated parallel synchrotron beams as discussed in chapter 1, with different energies E_1 and E_2 entering the chamber that should be measured independently without any interference [29]. The central electrode sketch diagram is shown in Fig (4-5).

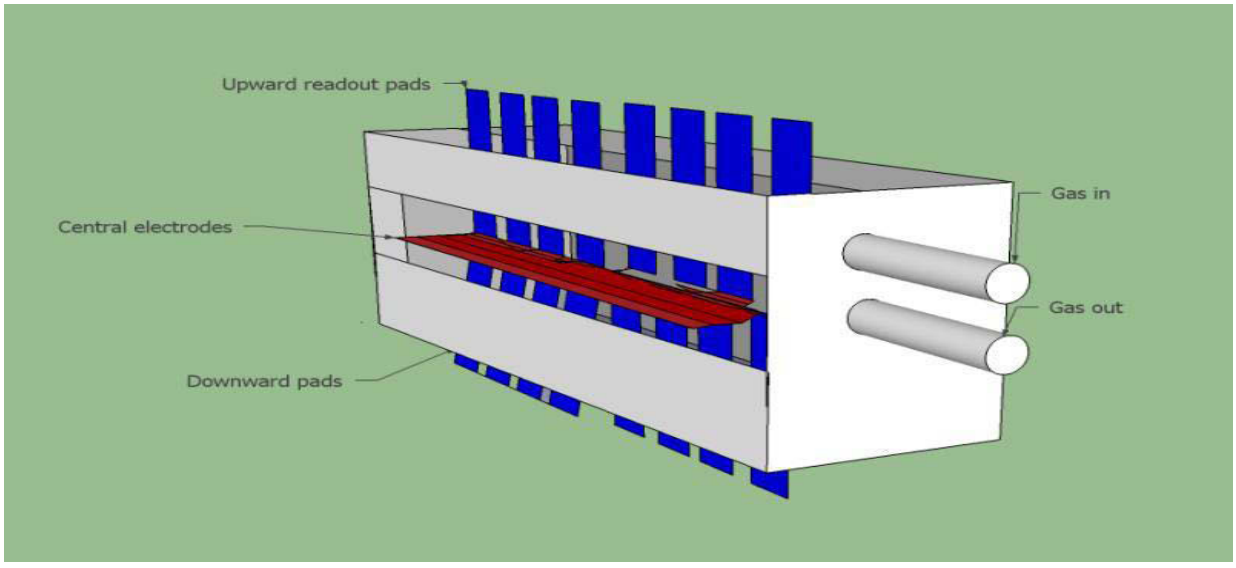

Figure 4-5: 3D sketch diagram of the Multi-channel ionization chamber shows the central electrode (red) at the middle of the chamber readout pads (blue) and gas input and output pipes.

4.2. Readout electronics

Low noise and linear electronics are important for high precision measurement. The following analog and digital electronics used for the readout of the beam monitor are briefly described.

The low noise electronics mainly contain the current voltage convertor (C.V) in which the operational amplifier OPA727 is used. It has very low noise of 6 nV/ at 100 kHz and bandwidth of 20 MHz. The OPA AD8131 is used as a differential line driver. A differential line receiver with OPA AD8130 is used. The output signal from the differential line receiver is injected into the 16 bit ADC from Meilhause which is used to digitize the signal to be processed by computer software [29].

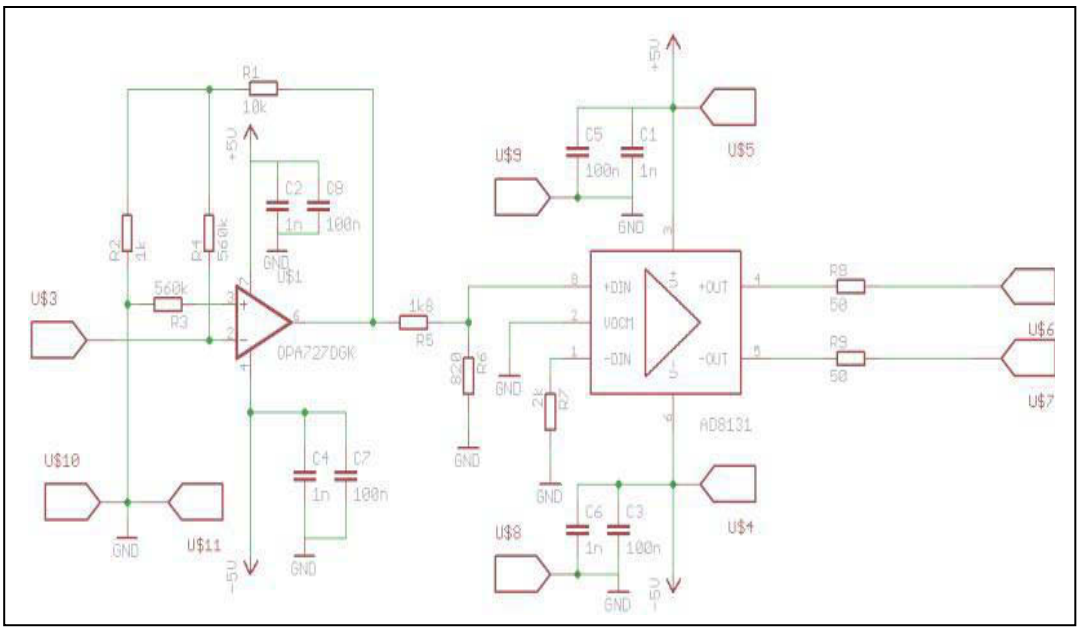

Figure 4-6: The complete sketch diagram of the PCB contains C.V converter and differential line driver.

4.2.1. Current to voltage converter

The output current which is produced from the Multi-channel ionization chamber is converted to a voltage. A constant input current obtained with a battery was used to test the current to voltage convertor [29]. The linear relation obtained from the measurement is shown in Fig(4-7).

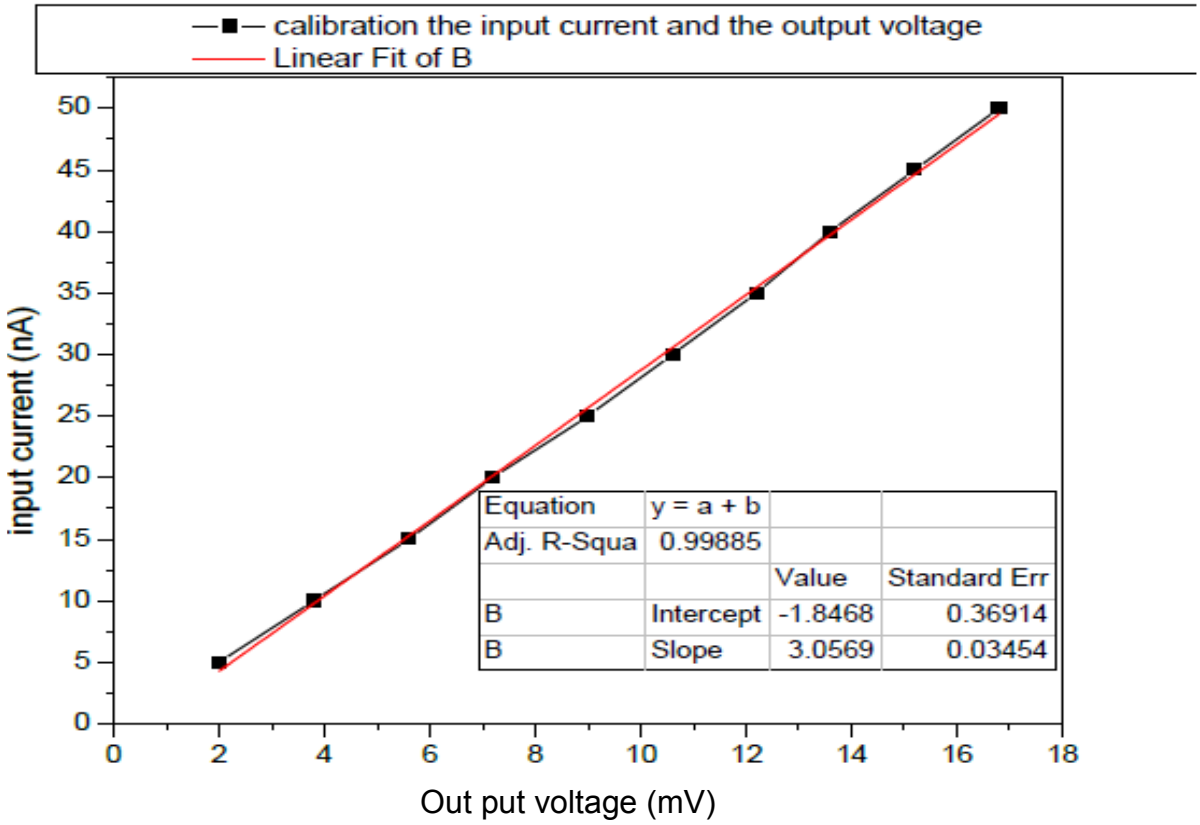

Figure 4-7: Calibration of the input current versus the output voltage from the current voltage convertor electronic circuit, shown in Fig (4-6).

4.2.2. Differential line driver

The second stage after the C.V convertor is the differential line driver (DLD). The OPA AD8131 is used as DLD which drives a differential signal from the output voltage signal of the C.V convertor. The sketch circuit diagram is shown in Fig (4-6).

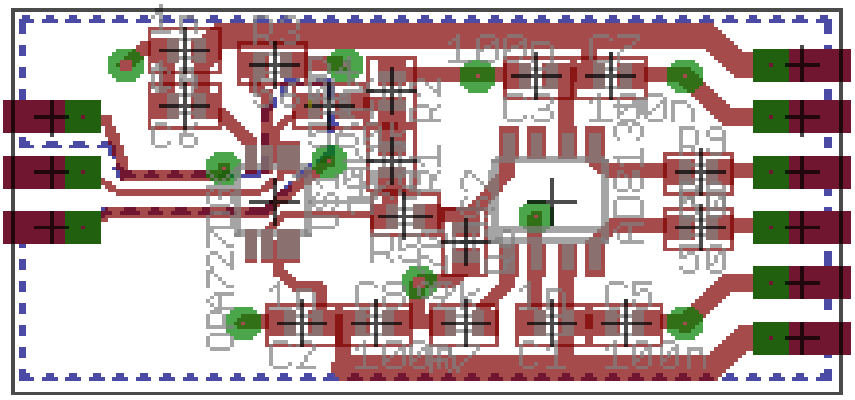

Figure 4-8: Layout board PCB image using Eagle software.

4.2.3. Differential line receiver

After the signal is derived from the current voltage converter and differential line driver, the signal is transferred through a shielded twisted pair cable of 20 m to the differential line receiver as a differential signal and received by a differential line receiver. The OPA AD 8130 is used as a differential line receiver, which subtracts the differential signal to reduce the pick-up noise from the signal. A low-pass filter with a cutoff frequency of (150 kHz) is implemented after the differential line receiver to reduce the pick-up of high frequency noise and get the signal ready to digitize by the Meilhaus ADC (ME-4661i) with 500 kHz, 16-bit A/D convertor which has A/D and D/A sections with a common ground isolated from the PC ground and the rest of the board. It has a channel time of 2 µs and a relaxation time of 1.5 µs [30].

The minimum time between two simultaneous measurements depends on the number of channels being sampled and the recovery time, which can be calculated as following.

Minimum scan time= number of channels x channel time + relaxation time.

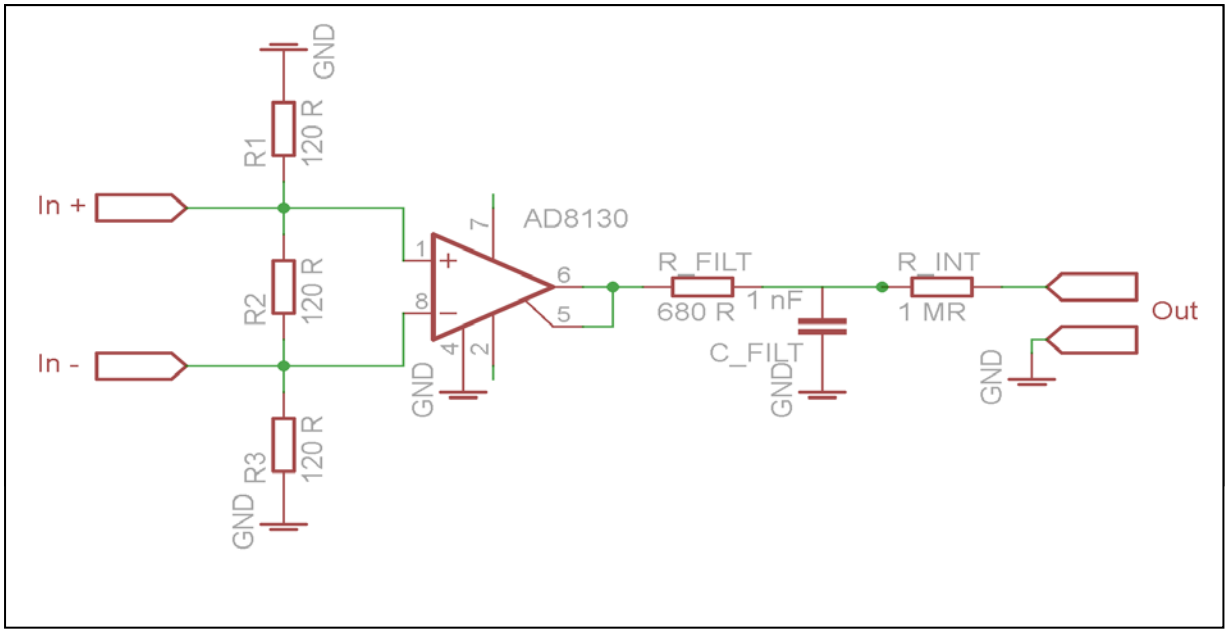

Figure 4-9: Differential line receiver sketch diagram showing the differential input signal and single-ended signal as output.

4.3. Noise measurement with styroflex capacitors

Polypropylene Film capacitors are used due to their most desirable electrical characteristics such as exceptionally high insulation, low leakage, low dielectric absorption, low distortion and excellent temperature stability.

We used a linear gate, spectroscopic amplifier and multi-channel analyzer to measure the output noise from the read-out electronics for the Multi-channel ionization chamber using different capacitors of type styroflex (120, 180, 200, 220, 270 and 330) pF.

4.3.1. Calibration the multi-channel analyzer

The calibration of the MCA is done using a 9 V battery which is terminated with a 150 MΩ resister to produce a current to the input channel of the electronics, which accepts an input current [30]. The output voltage is measured after the differential line driver by an oscilloscope and voltmeter to calibrate the offset and gain of the C.V convertor. The calibration curve is shown in Fig (4-7). The signal is injected into the multi-channel analyzer and the calibration spectrum and line fitting to the voltage with the channel number is shown in Fig (4-11), (4-12). The relation between the channel number and applied voltage is derived.

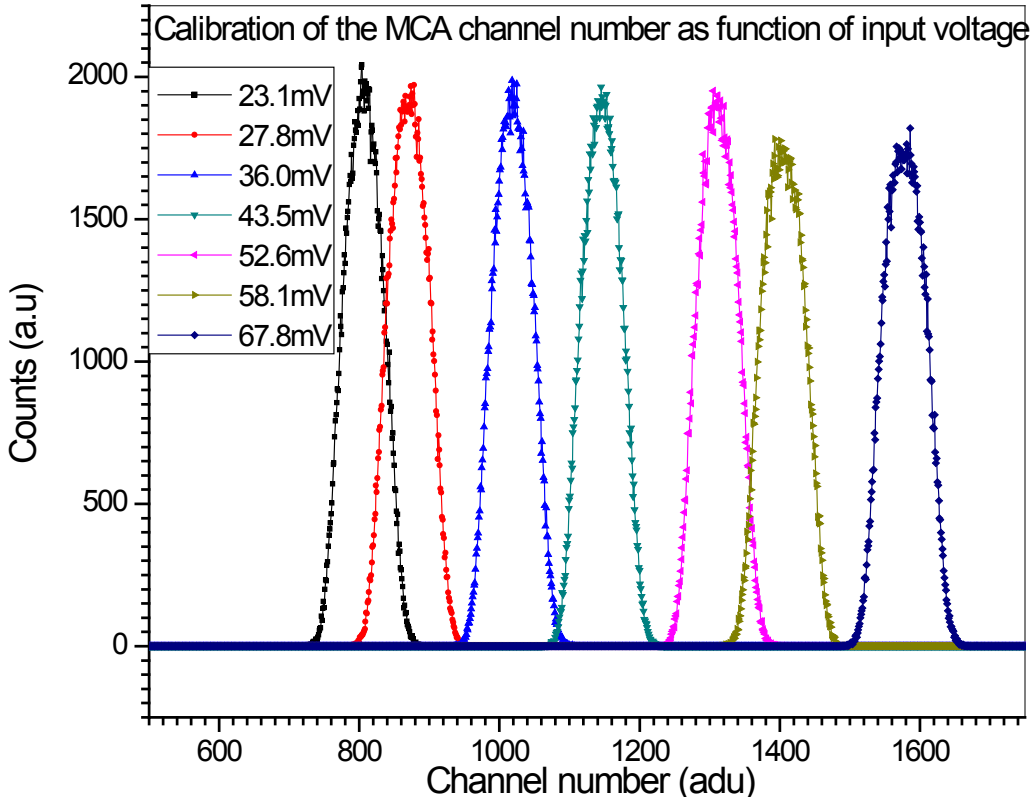

Figure 4-10: Calibration peaks of the input voltages and the peak channel number.

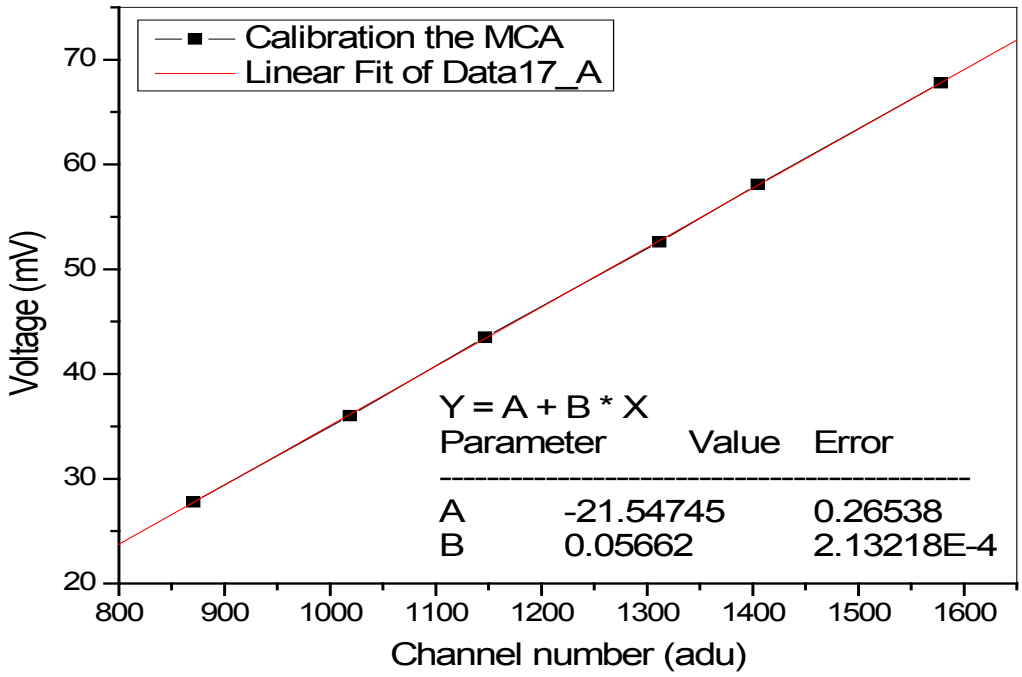

Figure 4-11: The linear fit for the input voltage and the channel number. The slope is found to be (0.05662).

4.3.2. Noise measurement

Different values of capacitor-type Styroflix are injected into the input stage of the readout electronics and then we look at the output from the linear gate, which depends on the gate pulse which is injected from a pulsed generator. The integrating time was 5 μs. This feeds the output of the linear gate to the spectroscopic amplifier, then to the multi-channel analyzer and then to the PC [31], as shown in the following block diagram.

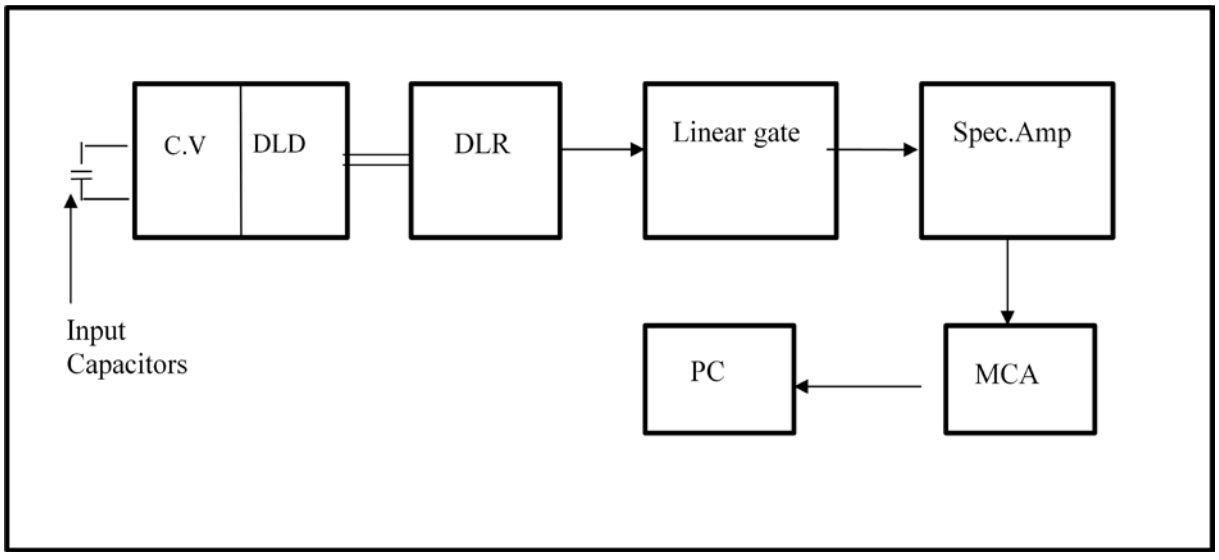

Figure 4-12: Measurement block diagram of the electronic noise with capacitors.

The following graph is the relation between the gain of the spectroscopic amplifier and noise in rms (V). It shows that noise increases with increasing gain.

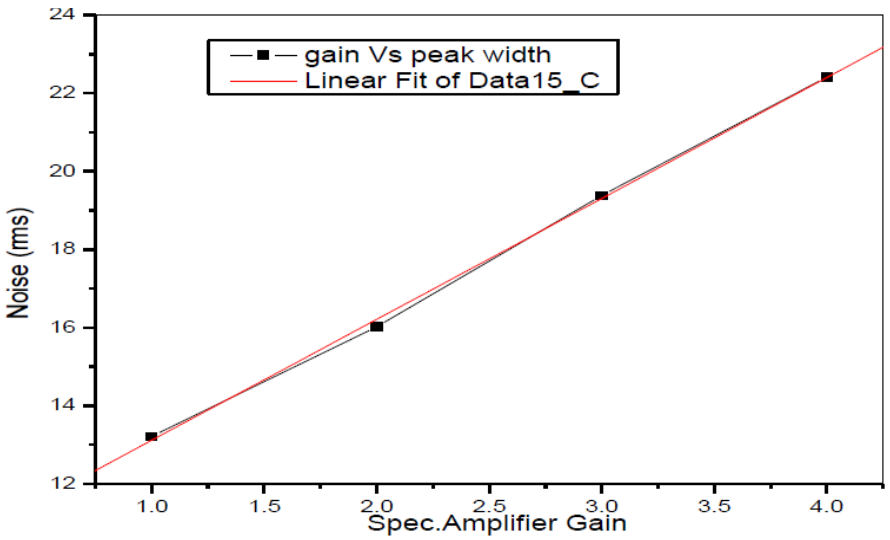

Figure 4-13: Noise level measurements with MCA as a function of spectroscopic amplifier gain.

4.3.3. Noise versus integration time

Theoretically, noise is dependent on the time between sampling pulses. The relationship between noise and integration time is measured using the setup shown in Fig (4-12). Using the MCA, the relationship between noise and integration time can be obtained. Fig (4-14) shows that noise decreases with increasing integration time.

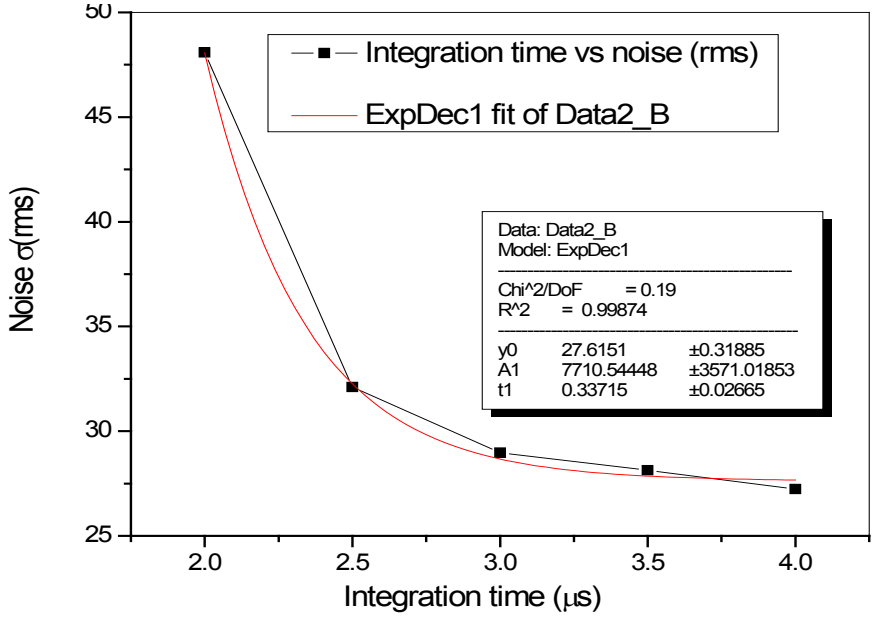

Figure 4-14: Relationship between integration time and noise, showing that noise decreases with increasing integration time.

Noise is measured with different input capacitors used to determine the dependence of noise on a range of input capacitors. The plot of noise versus the values of the input capacitors is shown in Fig (4-15). A polynomial fit is applied on the measured data to specify the noise at 0 pF intercept. The intercept represents the electronic noise at 0.3 rms (V).

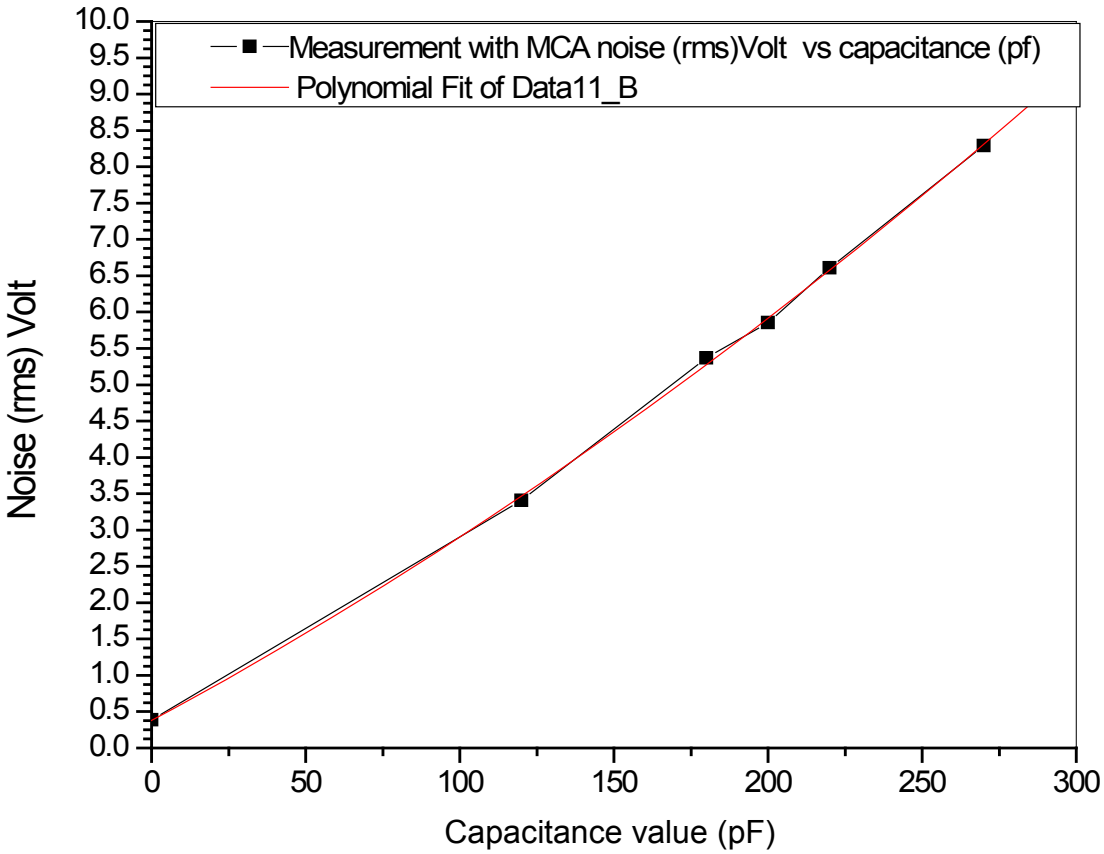

Figure 4-15: Noise measurements with MCA versus different input capacitors using the measurement setup in Fig (3-12).

4.3.4. Noise measurement with Meilhaus ADC

Another measurement is performed using the readout electronics with different input capacitors and the Meilhause ADC and directing the output signal to the PC as shown in the block diagram below, the signal comes out of the differential line driver and is driven through a 20 m twisted pair cable as differential signal to the differential line receiver, implementing a low-pass filter in front of the ADC card to reduce the pickup of high frequency noise. The overall noise can be read from the software implemented in PC.

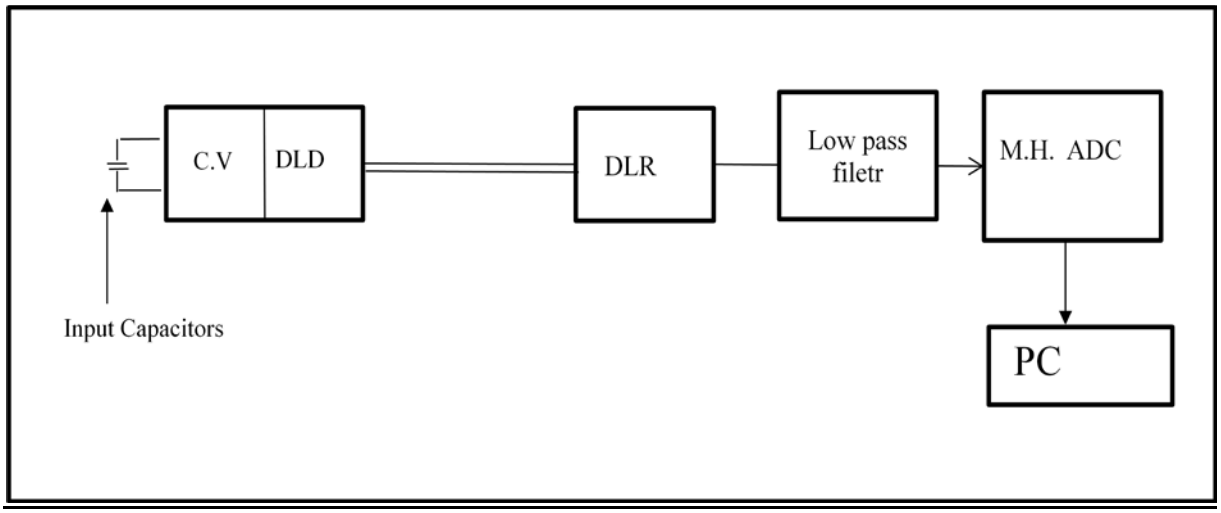

Figure 4-16: Sketch diagram showing the noise measurement with ADC and PC with different input capacitors.

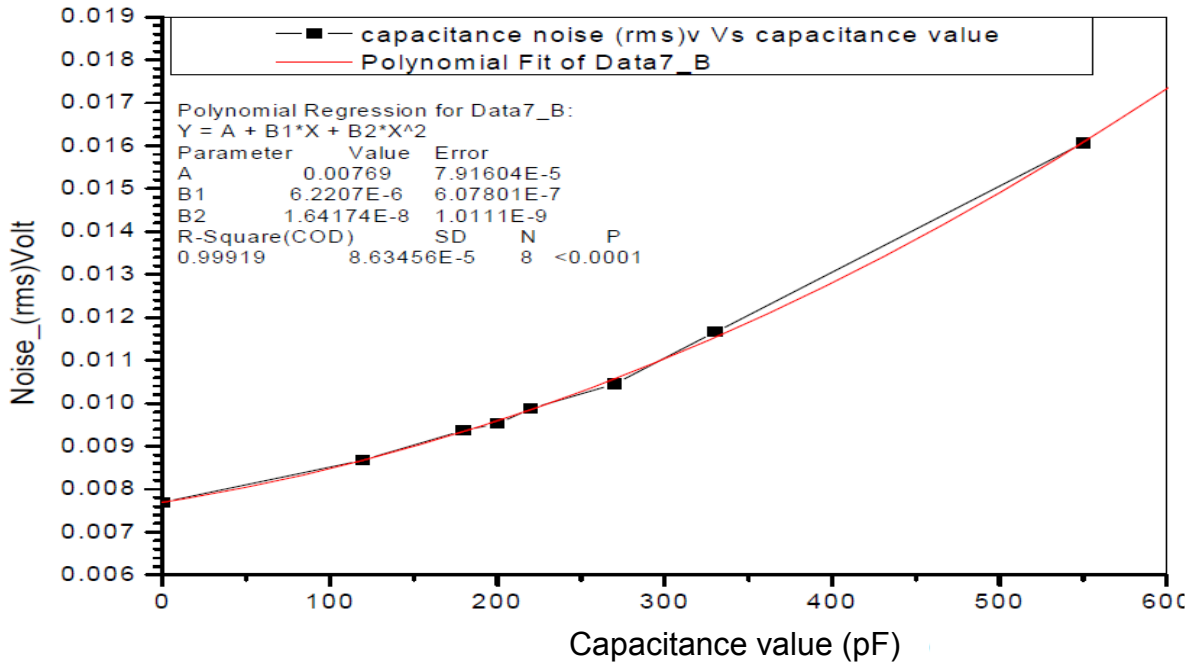

Figure 4-17: Measured noise in rms (V) as a function of the input capacitors with Meilhaus ADC card (ME 4661i).

The noise of the charge-sensitive preamplifier is measured by the setup block diagram shown in Fig (4-16), where the capacitors are inserted into the preamplifier and the output resulting from this charge is measured at the output of the filter amplifier (DLR), preamplifier noise is determined by measuring the root-mean-square (rms) of noise voltage at the output.

A polynomial fit is applied to the measurement results shown in Fig (4-17), the intercept value of the noise at 0 pF was 0.00769 rms (V). The measured signal is considered to be in the order of a few volts, and from chapter 6, the signal to noise ratio is calculated to be

$$\text{SNR= Signal / Noise = 1V/ 0.00769 V = 130} \qquad (4\text{-}1)$$

Chapter 5 Experimental setup

5. Introduction

This chapter introduces the most important experimental measurement setup and calibration procedures of the Multi-channel ionization chamber using synchrotron radiation and 2 kW molybdenum X-ray sources with a characteristic energy of 17.44 keV and regulation of photon intensity by changing the X-ray tube current.

5.1. Setup 1. X-ray spectrum

The major characteristic of the Multi-channel ionization chamber has been studied using a crystallographic 2 kW X-ray tube. The X-ray spectrum is measured using a proportional chamber connected to the multi-channel analyzer. The setup sketch diagram is shown in Fig (5-1), setting the voltage of the X-ray tube to 25 kV and the tube current to 5 mA.

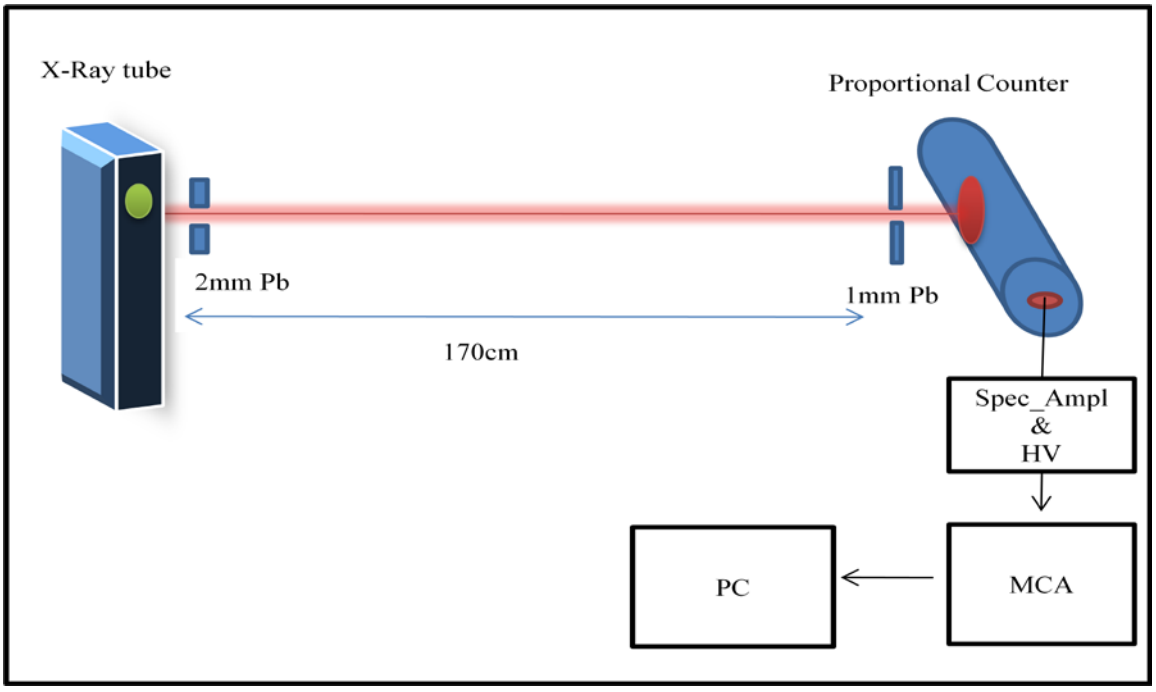

Figure 5-1: Setup for X-ray spectrum measurement with proportional counter and MCA, a 2 mm collimator is placed in front of the X-ray tube, a 1 mm lead collimator in front of the proportional chamber and the total distance between the X-ray tube and the proportional chamber is 170 cm:

5.2. Setup 2. Linearity and saturation current measurement:

The following setup is used for the measurements of the saturation current with synchrotron radiation at EDR beam line at BESSYII where the Multi-channel ionization chamber is placed 16 cm from the beam shutter and a 5 mm lead collimator is placed 3.5 cm from the chamber and a 3 mm lead collimator is attached to the chamber entrance window to protect the lower pads from the synchrotron beam.

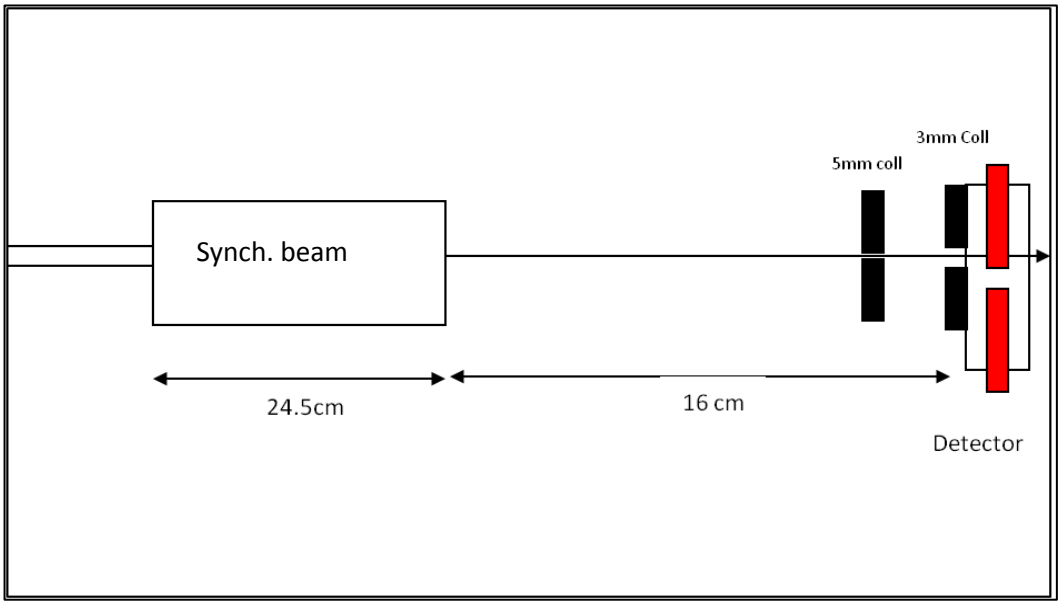

Figure 5-2 saturation current setup at EDR beam line at BESSYII.

The following setup is used for the saturation current and linearity measurement with the X-ray tube at Siegen University is shown in Fig (5-3) where the chamber is placed 14 cm from the X-ray tube and a 0.5 mm lead collimator is placed 3.5 cm from the chamber.

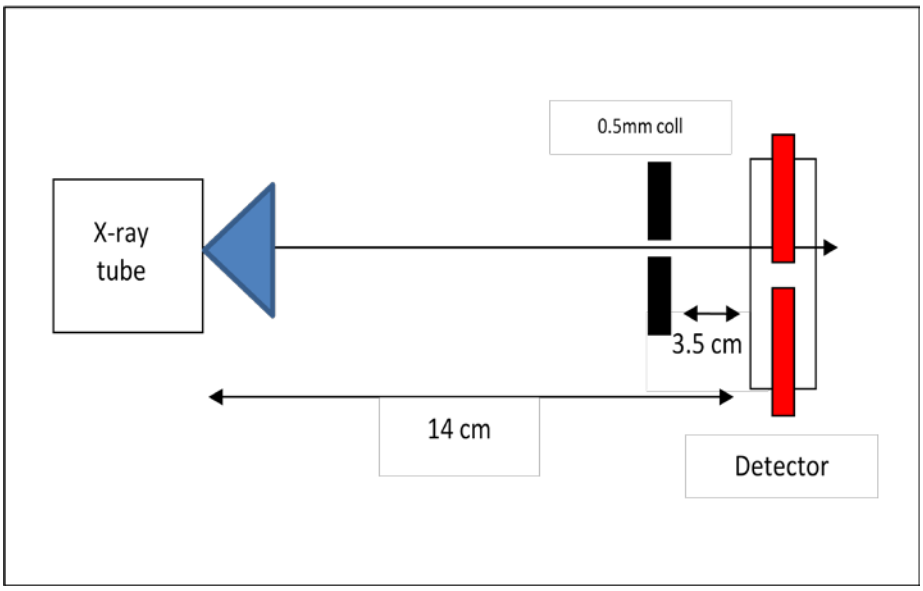

Figure 5-3 linearity and saturation current measurement setup with Mo source X-ray tube.

5.3. Setup 3. Position resolution measurement:

The chamber is placed on a horizontal scanner and moves in increments of 1 µm. A 50 µm step scan is performed for the measurement with a 2 kW molybdenum X-ray source. The experiment is carried out by applying a 60 mA tube current and voltage of 25 kV, filling the chamber with 15 bar of Argon-Methane gas mixture (90%:10%) and applying voltage of 1 kV, using the experimental setup shown in Fig (5-4) below.

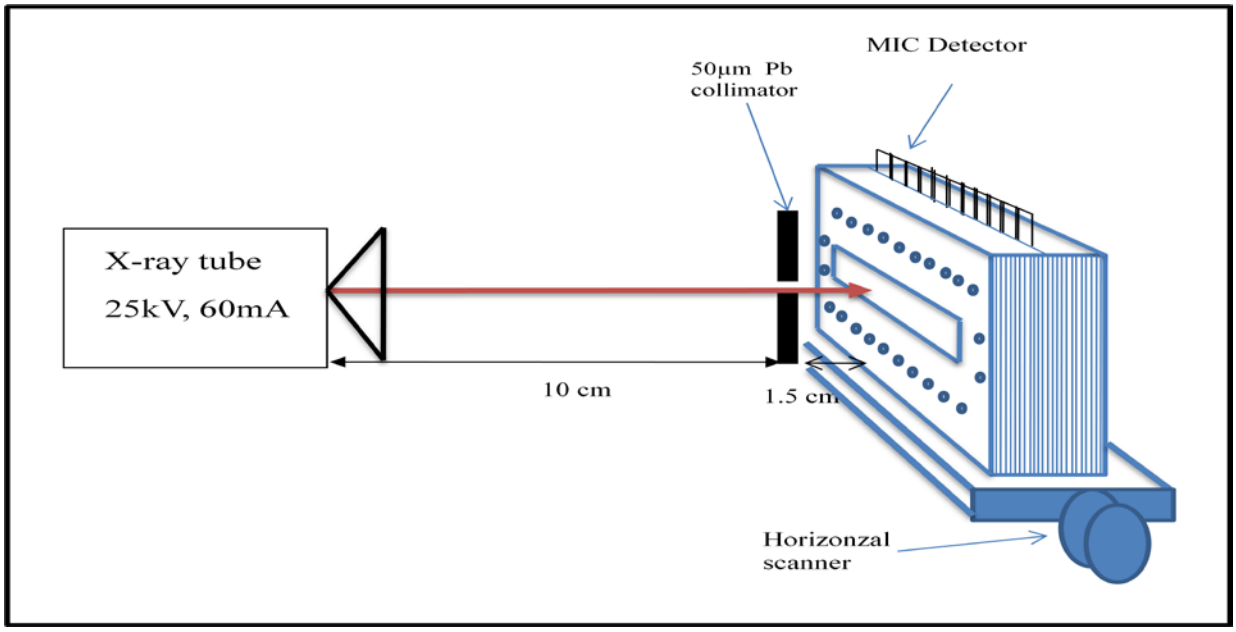

Figure 5-4: Setup for the position resolution measurement with 15 bar of Argon-Methane gas (90%:10%) with an X-ray tube source. Chamber is set 10 cm from the X-ray tube on a horizontal scanner; 50 µm vertical lead slit collimator is set 1.5 cm in front of the chamber.

5.4. Setup 4. Time response measurement

The results are obtained using a multi-channel ionization chamber with construction details shown in chapter 4. The chamber is filled with a mixture of 90% Argon and 10% Methane using an applied pressure of 5, 7 and 10 bar and pure Nitrogen gas with pressures of 15 and 26 bar. The measurements were carried out in the EDR synchrotron beam line at BESSYII. The beam size was 1x1.5 mm^2. A circular lead chopper with diameter of 9 cm and 1 mm slits cut in four positions as discussed in chapter 3, and shown in Fig (3-12) is used. The chopper is mounted on a drill machine connected to a power supply which is used for chopping the synchrotron beam as shown in Fig (5-5). Two collimators are placed in front of the chamber; a 3x50 mm^2 horizontal slit lead collimator is attached to the chamber entrance window to protect the lower parts of the chamber from the beam and a 0.2x0.4 mm^2 collimator is placed 4 cm from the chamber, (see Fig 5-5).

The multi-channel ionization chamber is placed 122.5 cm from the beam shutter. The lead chopper is mounted in between at 35 cm from the beam shutter and 87.5 cm from the chamber. The synchrotron beam is aligned to hit the upper readout pads and the lower readout pads are shielded with a 3x50 mm^2 lead collimator as shown in Fig (5-5).

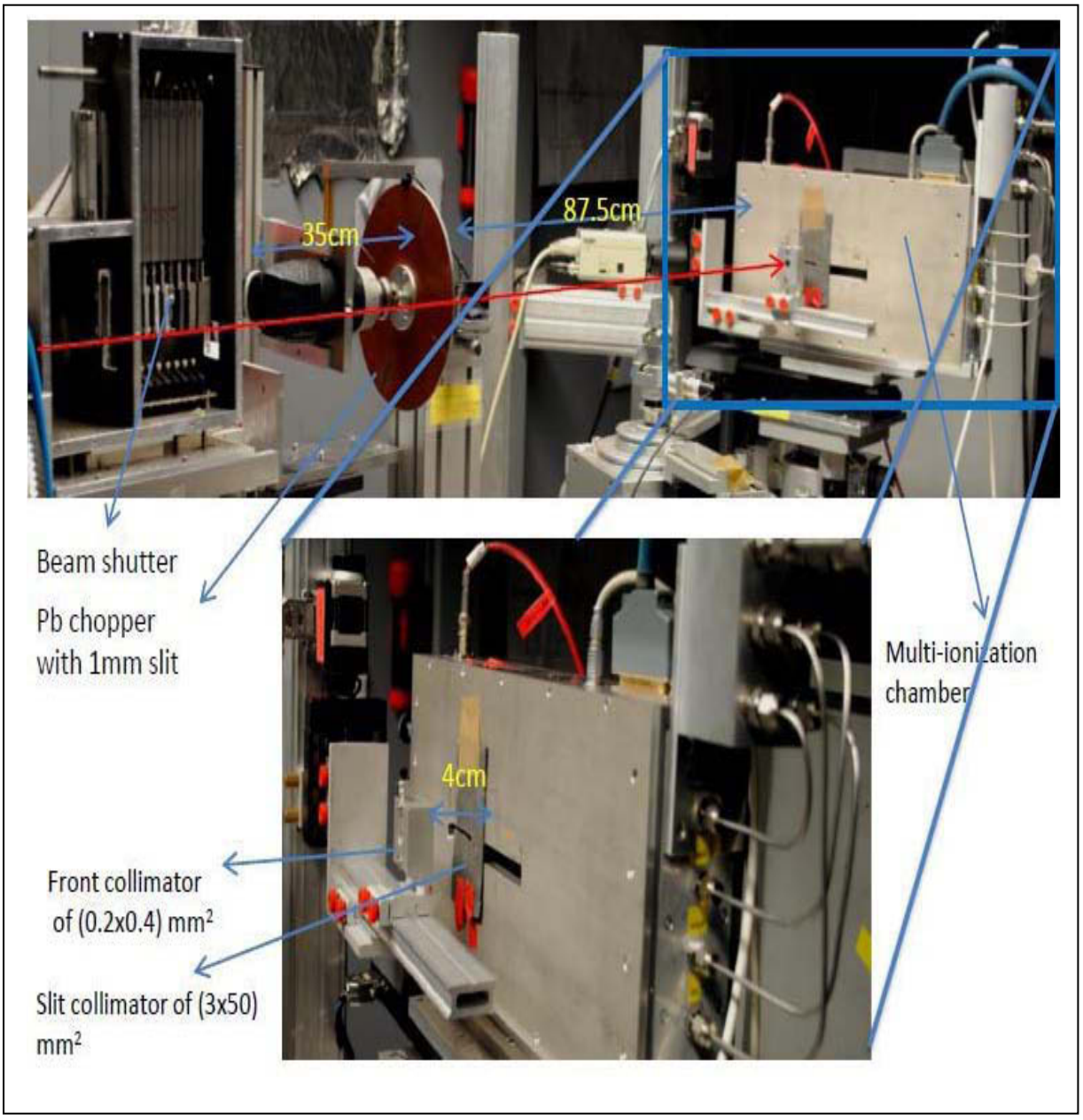

Figure 5-5: The measurement setup at BESSYII beam line, the beam shutter left, lead chopper at 35 cm from the shutter, the chamber is placed at 87.5 cm from the chopper. Magnified image to show the two collimators in front of the chamber.

Chapter 6 Results and analysis

6. Introduction

This chapter details the experimental results and offers analysis of the calibration measurements of the multi-channel ionization chamber with X-ray tube and time response measurement, when operating a multi-ionization chamber with a high synchrotron radiation photon flux from an EDR beam line at BESSYII, and the simulated output signals compared to those measured.

6.1. X-ray spectrum

The multi-channel analyzer (MCA) is calibrated using different fluorescent X-ray sources of (Cu, Rb, Mo and Ag). A linear model is fitted to the channel number and X-ray energy curve to get the calibration value. The spectrum of the X-ray tube is measured using setup 1, a Gaussian fit is applied to the spectrum peak and the characteristic energy kα is found to be 17.40373 keV which fits with the theoretical value. The measured spectrum is shown in Fig (6-1).

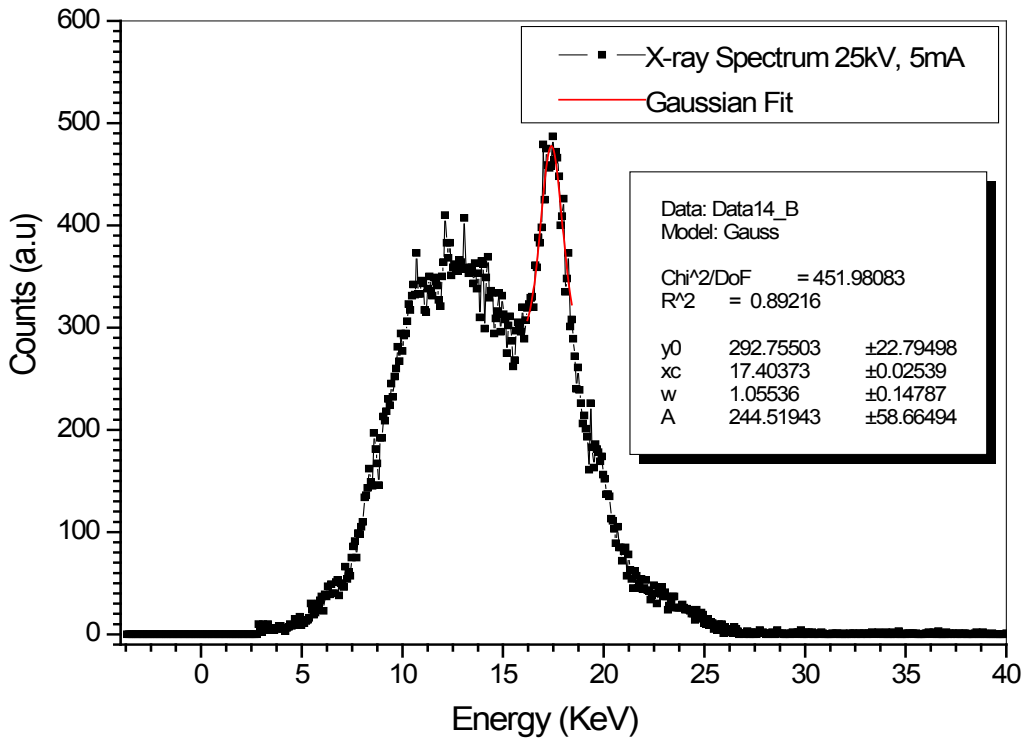

Figure 6-1: Measured spectrum of the Molybdenum X-ray source which has characteristic energy of 17.40373 keV.

The relationship between the tube current and the X-ray photon intensity is measured by using setup 1 and applying 25 kV X-ray tube high voltage and regulating the tube current. The intensity measured spectrum is plotted in Fig (6-2).

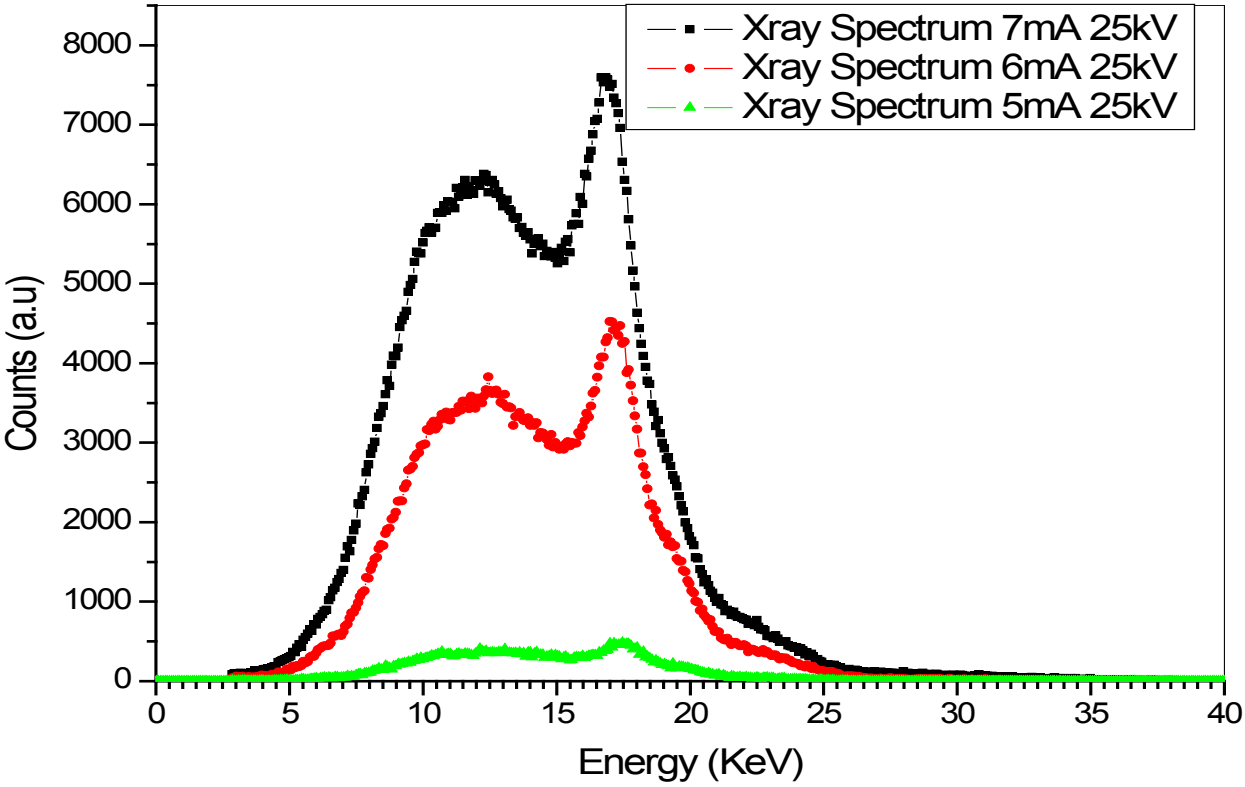

Figure 6-2: Measured X-ray spectrum at different intensities using proportional counter and applying 25 kV X-ray tube high voltage and regulating the tube current from (5 to 7) mA.

6.2. Linearity

The linearity test is particularly important when using the detector in a measurement with a synchrotron radiation, were the beam intensity is extremely high and the measurements can be affected by the nonlinear response of the detector.

The linearity response of the multi-channel ionization chamber has been investigated with respect to variation of X-ray photon intensities, which depends linearly on the X-ray tube current from Fig (6-2). Using setup 2, in Fig (5-3) and filling the chamber with a 10 bar $ArCH_4$ gas mixture (90:10%), and 10 bar Nitrogen gas, the detector was biased to (-1000 V) by using a stable power supply while a small collimator with a 1 mm slit is placed in front of the detector [23]. The measured results of the linearity are shown in Fig (6-3).

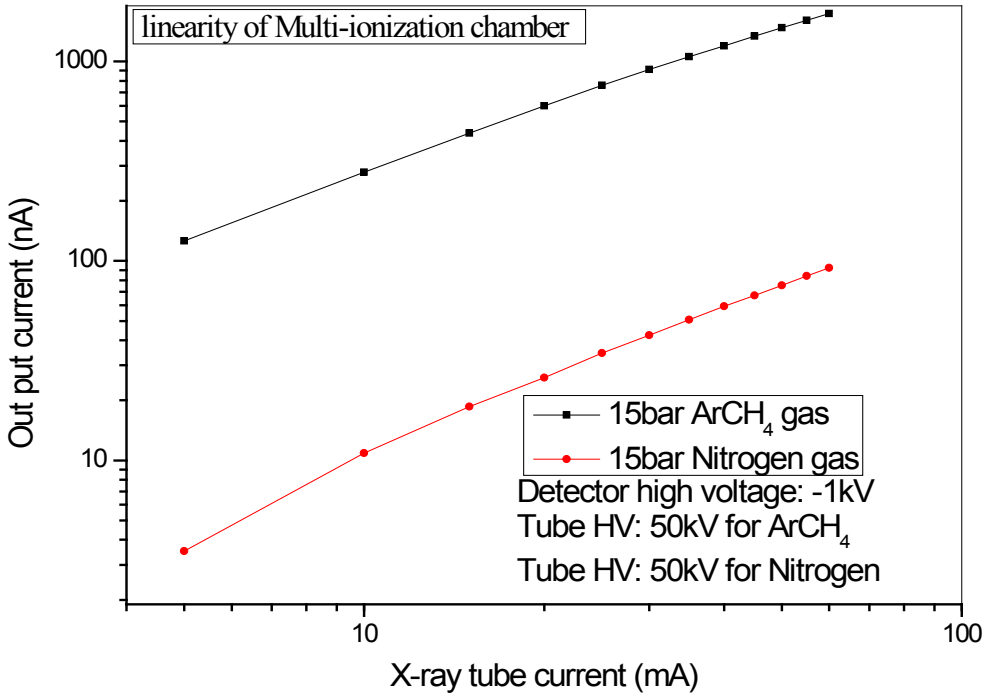

Figure 6-3: Linearity measurement of the multi-channel ionization chamber at different tube current using Nitrogen gas and $ArCH_4$ gas mixture of (90:10%).

6.3. Saturation current

In the ionization chamber the drift of the positive and negative charges is represented by the applied electric field in a given volume of gas that is continuously irradiated by an X-ray source. The amount of electron ion pair production depends on the gas density, number of photons and energy of the incoming photon flux. The rate of charge will be balanced by the loss of ion pairs from the volume by recombination and diffusion.

Current voltage characteristics of the chamber have been studied using different X-ray photon intensities by applying different tube currents which increase the photon flux and using setup 2, in Fig (5-3). When operating the chamber with the synchrotron radiation the saturation current is measured using setup 2, in Fig (5-2), by filling the chamber with Nitrogen gas at different pressures and regulating the applied voltage from 0 to 5 kV as shown in Fig (6-4) panel [b]. The electric field is created inside the chamber by applying external voltage from a stable power supply.

Figure (6-4) shows that no current flows in the absence of an applied electric field, since the ions and electrons which are created disappear either by recombination or diffusion from the active volume. As the voltage increases, the electric field begins to drive the positive ion towards the cathode and electrons towards the anode. The measured current increases with the

applied voltage as this increases the drift velocities of the charges and reduces the amount of lost charges. At sufficiently high applied voltage, the electric field is great enough to reduce the recombination to a negligible level and all the produced charges are collected in the electrodes, and with further increase of the applied voltage the output current remains constant because the charge collection rate is constant under these conditions, the ionization chamber is conventionally operated where the measured current is also constant which is called saturation current [6].

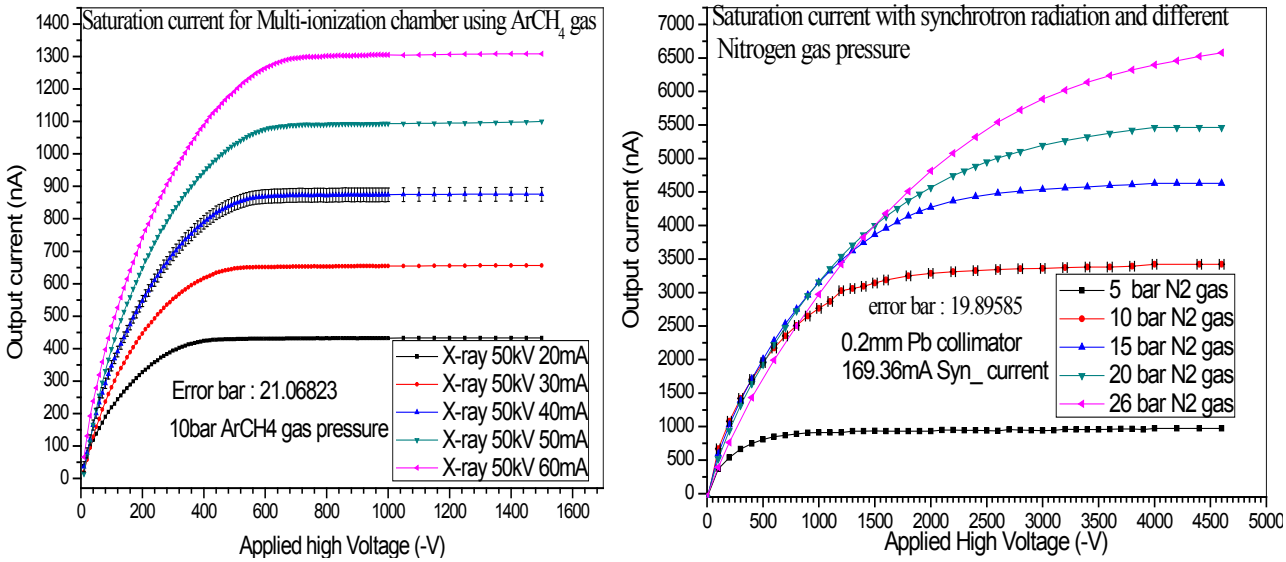

[a] [b]

Figure 6-4: The current voltage characteristics measurement with different applied voltages and different Nitrogen gas pressures with synchrotron radiation [b]. And 10 bar pressure of $ArCH_4$ gas mixture with X-ray tube [a], showing that the saturation level increases with increasing photon flux intensities.

The multi-ionization chamber sensitivity is given by

$$I_{out} = s\ p\ I_{syn} \tag{6-1}$$

$$s = \frac{I_{out}}{p\ I_{syn}} \tag{6-2}$$

Where I_{out} is the measured current, p is pressure and I_{syn} is the synchrotron current

Detector sensitivity to high intensity photon flux is taken from the measurements with different nitrogen gas pressures and the synchrotron beam shown in Fig (6-4), by dividing the output current signal to the applied pressure and the synchrotron current which is shown in Fig (6-5) below.

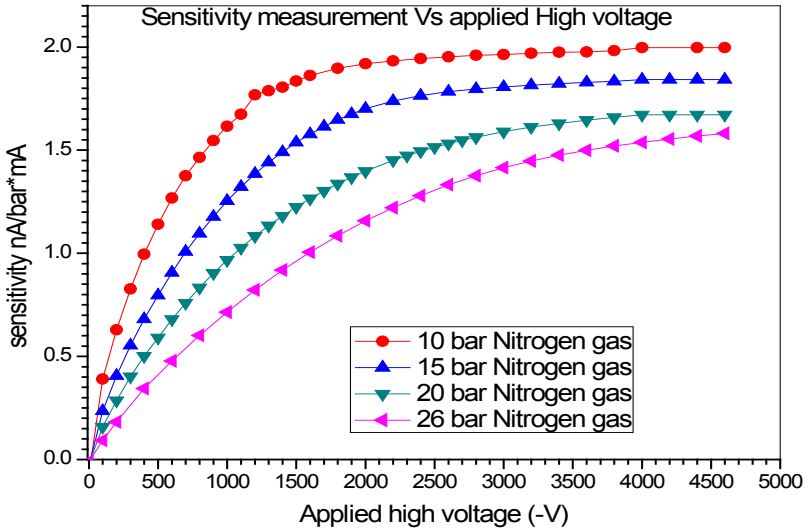

Figure 6-5: Multi-ionization chamber sensitivity measurement with high intensity synchrotron beam and different nitrogen gas pressures.

6.4. Position resolution measurement:

A horizontal scan measurement is done to check the separation between the pads of the multi-channel ionization chamber. The horizontal scan measurement results are shown in Fig (6-6) using setup 3 as in Fig (5-4), the scan started from the middle of upward pad number 2 and continued to the middle of upward pad number 5 while operating the chamber in the saturation region by applying voltage of 1kV, the pad size was found to be 178 mm and by differentiating the edge profile as shown in Fig (6-6) to obtain the line spread function that is shown in Fig (6-7).

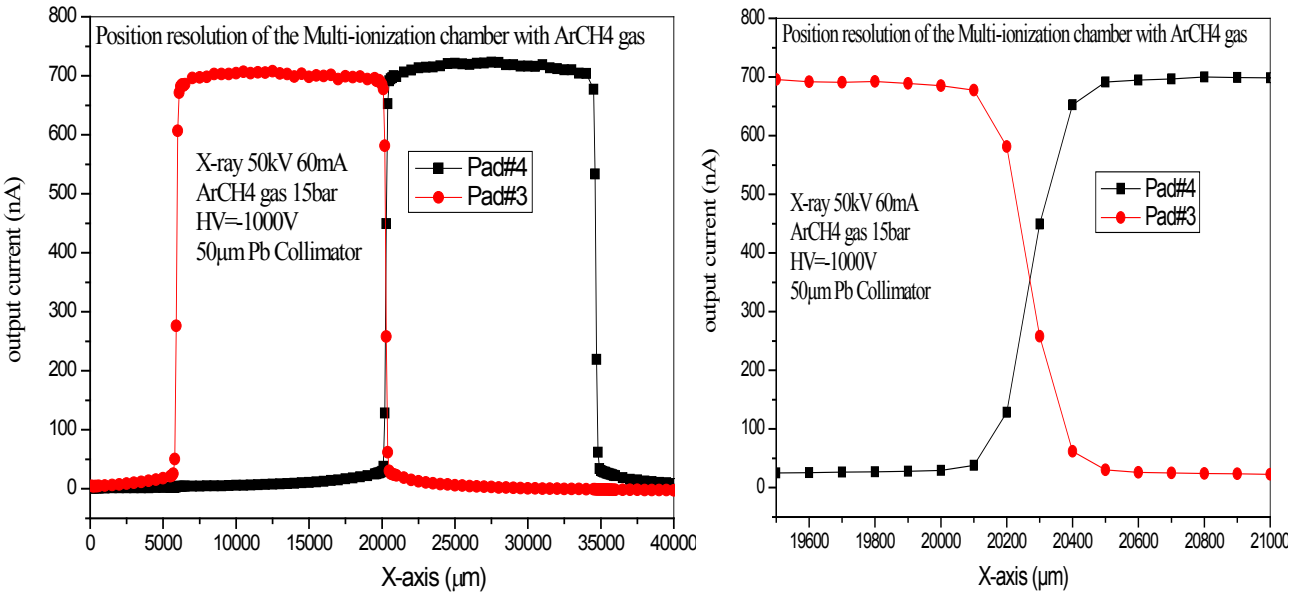

Figure 6-6: The horizontal scan result profile of two neighboring pads of the multi-channel ionization chamber [A]. Position resolution measurements with a 15 bar Argon-Methane gas mixture of (90:10%) and applied high voltage of 1 kV using a 50 µm lead collimator in front of the detector, a 50 µm scan step is performed [B].

The experimental value of sigma (σ_x) is determined by the intrinsic resolution of the chamber that is included, geometry of the chamber with accurate alignment of the anode pad, photon beam distribution and secondary electrons, mainly photoelectrons which are produced by photon interaction in the sensitive volume. These depend on the photon energy, gas pressure and geometry. The space charge effect of ion and electron diffusion also contributes [28].

The photon beam distribution depends on the focal spot of the X-ray tube, collimator width and step geometry. In addition there are also effects from the space charge, diffusion of electrons and florescence.

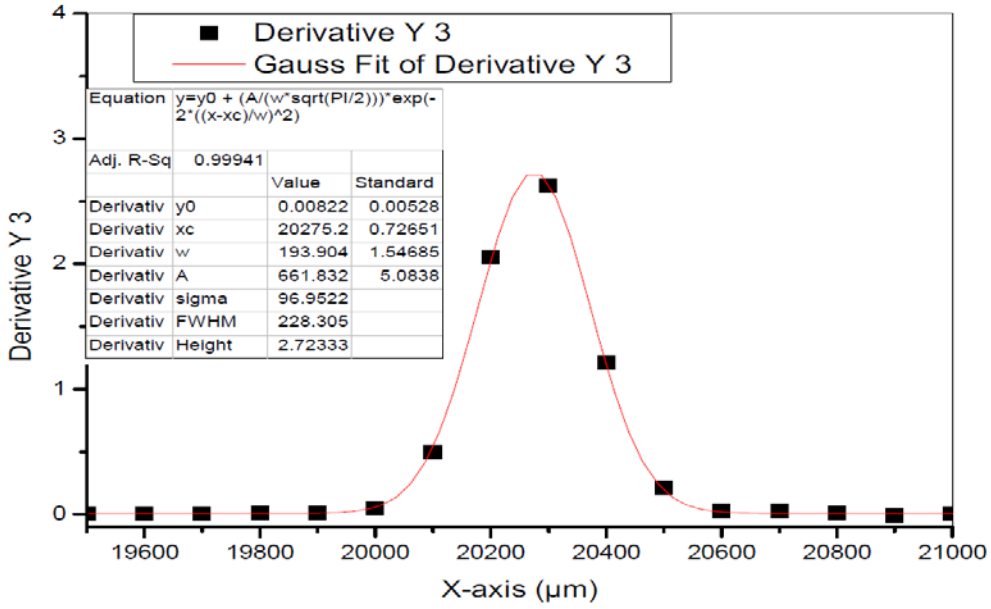

Figure 6-7: Derivative of the S shape scan shown in Fig (6-6), it represents the Gaussian shape, which is the effect of the primary photo electrons in the chamber. The FWHM was found to be 0.228 mm.

6.5. Space charge effect

At high photon flux rates, the most obvious impedance is caused by the space charge effect of most gas chambers. Space charge has an influence on the signal amplitude within the signal track where the positive ions need several milliseconds be moved from their position of creation by the incoming photons to the cathode. The arrival of the electrons at the anode plates is in the order of microseconds. The accumulation of the slow positive ions distorts the electric field, which has an influence on the electron and ion drift velocities and affects the total current density inside the chamber volume. In this chapter the measured result of the space charge effect will be shown. [32]

6.5.1. Measurement with $ArCH_4$ gas mixture

The time response measurement is carried out using setup 4, in Fig (5-5) and filling the chamber with an Argon-Methane mixture of (90:10%), the space charge effect is investigated. As shown in the following figure the time response measurement with a 10 bar $ArCH_4$ mixture using a lead slit chopper, when applying a low electric field with the slit open, a fast current signal appears and immediately drops down according to the space charge effect which disturbs the electric field and drift velocity of the charges till an equilibrium is reached and the signal declines as soon as the chopper is closed. By applying a high electric field in the saturation region a plateau is observed according to the fast drift velocities of the charges as well as reduction of the charge loss by the recombination effect as shown in Fig (6-8).

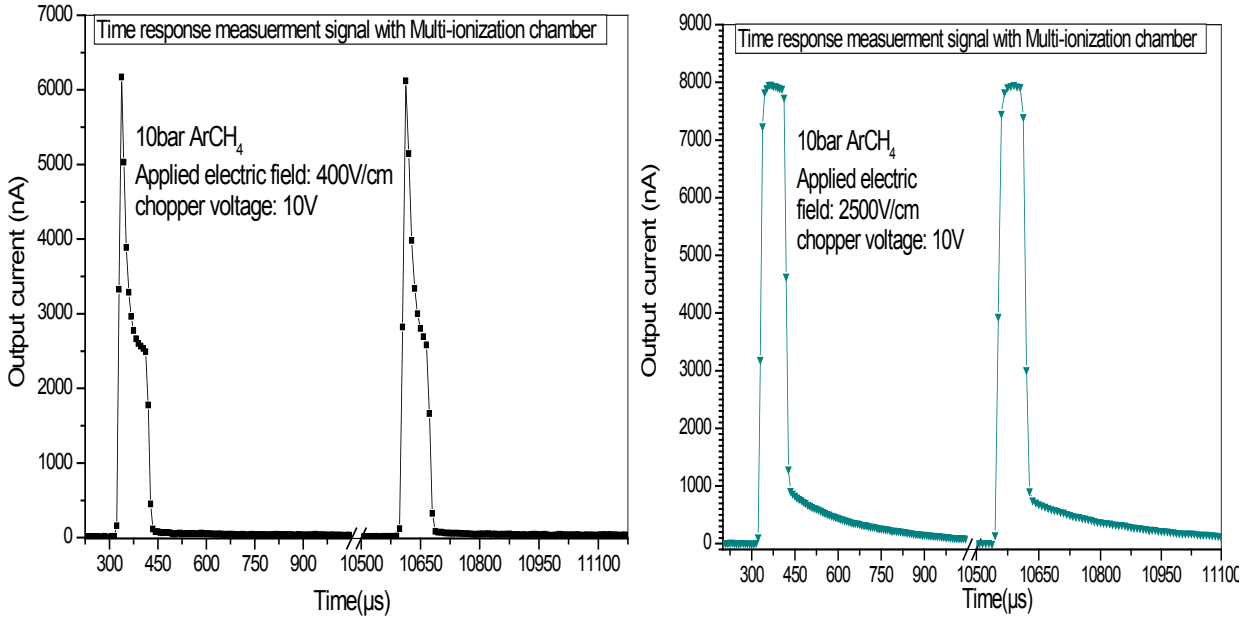

Figure 6-8: Time response measurement with 10 bar $ArCH_4$ mixture of (90:10%) using 1 mm lead slit chopper. When applying low electric field in the recombination regime with electric field of 400 V/cm [A]. By applying a high electric field in the saturation region with electric field of 2500 V/cm, the time response is measured and a plateau is observed [B].

The measured result of the space charge effect using an Argon-Methane mixture of (90:10%) with the pressure mentioned before and tuning the applied electric field from 400 V/cm up to 2500 V/cm, by plotting the figures together the space charge effect is clearly observed. As shown in Fig (6-9), Fig (A-1) and Fig (A-2).

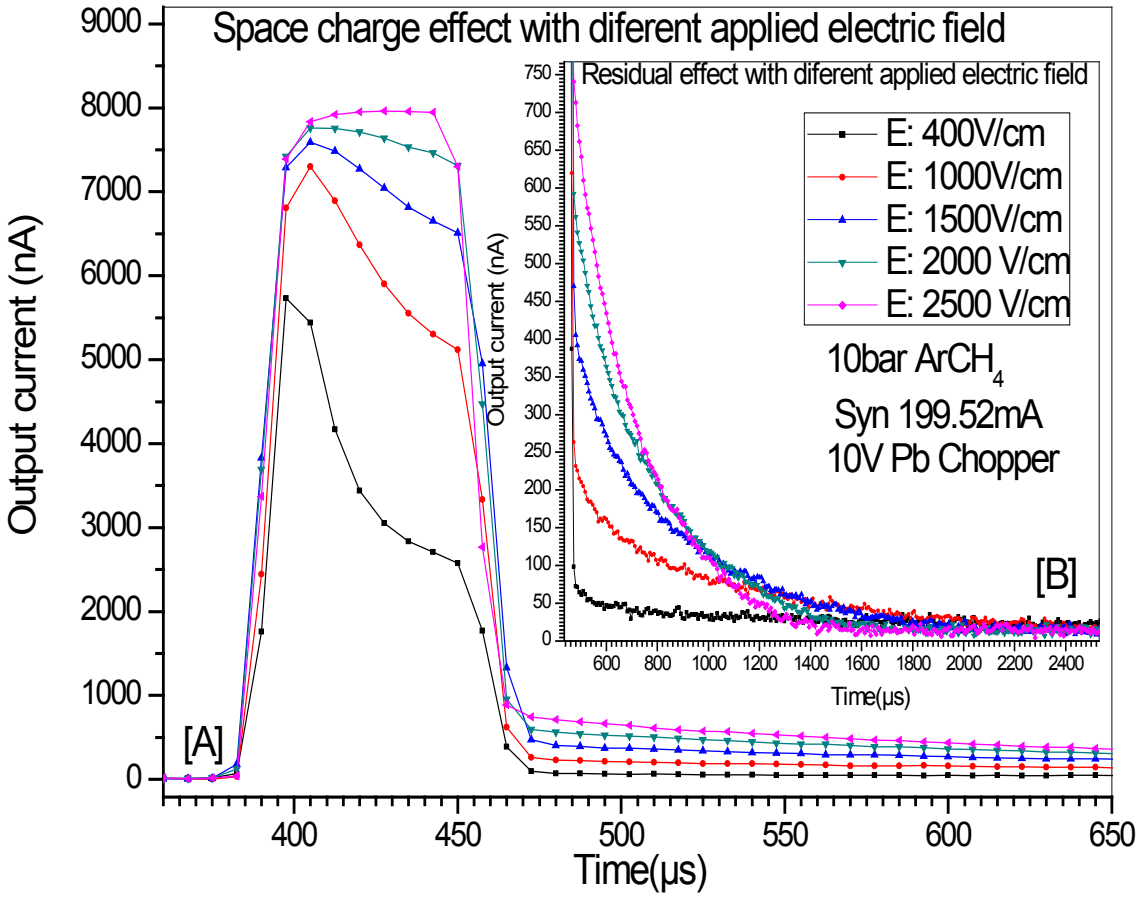

Figure 6-9: This figure shows different measurements of the output current as a function of applied electric field from 400 V/cm to 2500 V/cm, where the space charge effect decreases with the increasing of the applied electric field [A]. Magnified long tail signal to study the ion collection time [B].

6.5.2. Measurements with Nitrogen gas

Another measurement was conducted using setup 4, shown in Fig (5-5) and filling the chamber with pure Nitrogen gas at pressure of 15 and 26 bar and tuning the applied electric field from 200 V/cm up to 2000 V/cm. By plotting the figures together the measured output current as a function of applied electric field, a strong attenuation of the output current signal and exponential behavior is clearly observed according to the loss of the charges by recombination and diffusion when operating the chamber in the recombination regime. Further increasing the applied electric field in turn increases the drift velocities of the charges thus increasing the output current and a flattening at the top of the amplitude signal is observed. By further increasing the applied electric field till the saturation regime a plateau is observed as shown in Fig (6-10), Fig (6-11).

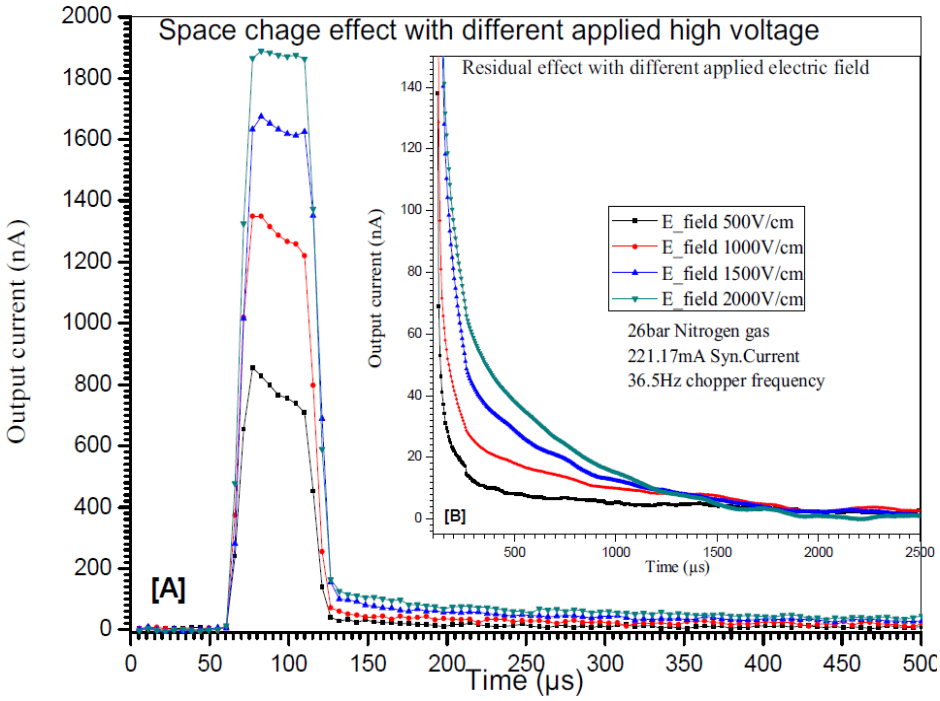

Figure 6-10: Time response measurement for 26 bar Nitrogen gas pressure as a function of different applied electric field a plateau is observed at 2000 V/cm [A]. The magnified long tail signal for ion collection time [B].

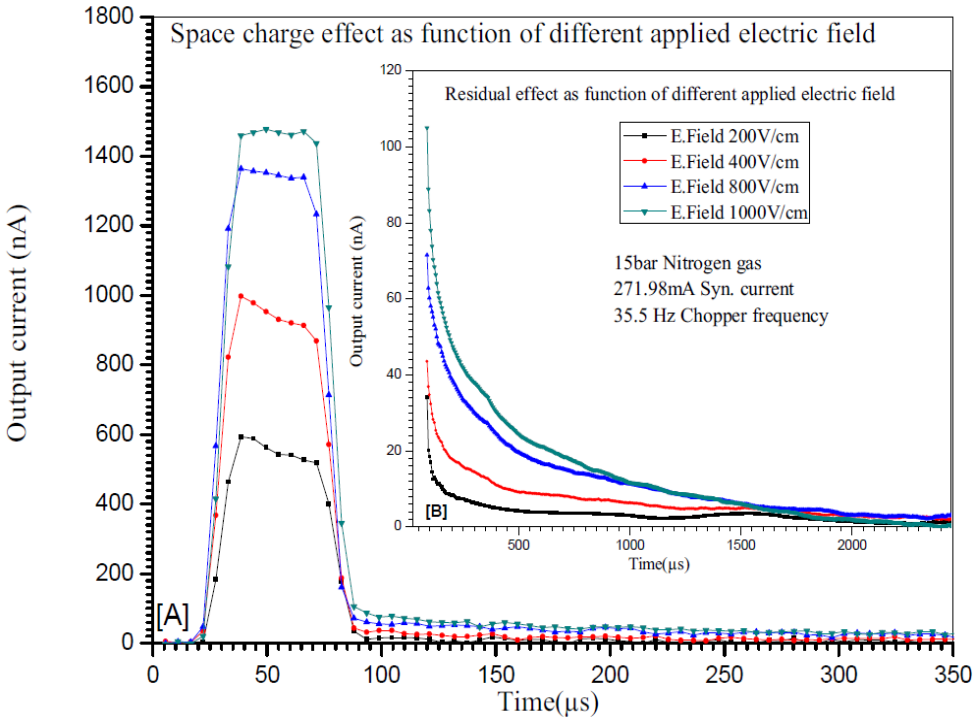

Figure 6-11: Time response measurement for 15 bar Nitrogen gas pressure as a function of different levels of applied electric field, a plateau is observed at 1000 V/cm [A]. Magnified long tail signal [B].

The effect of the space charge on the output amplitude current signal shown in Fig (6-8) panel [A] can be represented by the difference between the maximum amplitude height and the minimum amplitude height. Plotting the difference in amplitude of the measured curves gives the relation between applied electric field and output current signal in Fig (6-12) below

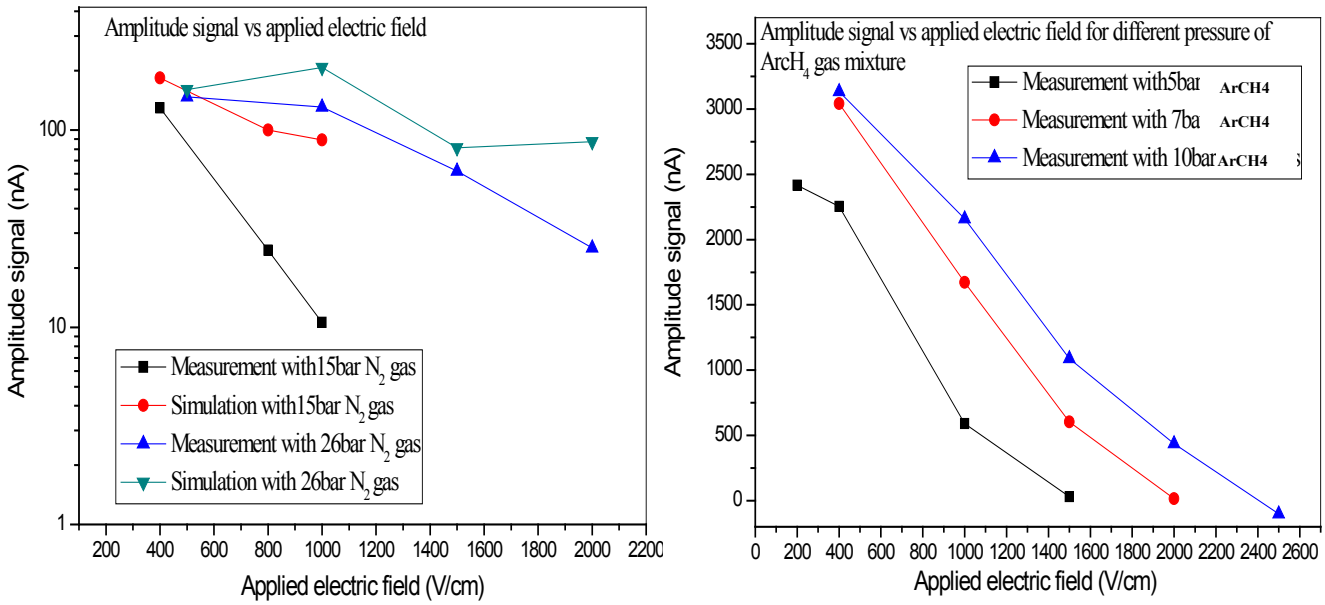

Figure 6-12: The relationship between the applied electric field and the space charge effect on the amplitude signal is plotted with different pressures of Argon methane gas mixture and nitrogen gas, showing the distortion of the electric field according to the space charge effect as a function of gas pressure.

This effect increases with increasing gas pressure which also increases the total amount of charge produced inside the chamber. However, the space charge effect, recombination and diffusion effects are considered, as well the strong attenuation in the output response signal observed in the measurements when operating the chamber in the recombination regime, this effect is less with Nitrogen gas than the $ArCH_4$ gas mixture.

It was found that increase of drift potential is proportional to the pressure and the amount of positive ion charge that flows back into the drift volume and produces the same amount of charge inside the drift volume as before, and the output current signal increases by a factor with increasing gas pressure.

6.5.3. Residual effect

The long tail signal observed from the measurements shown in panel [B] in Fig (6-9), Fig (6-10), Fig (6-11), Fig (A-1) and Fig (A-2) represents the remaining ions per collection time. At these moments of measurement the chopper had closed and interrupted the incoming photon flux. Accordingly, there is no new generation of electron and ion pairs. The remaining

electrons inside the active volume collect at the anode plate in a very short time, according to their fast drift velocity compared to the ion drift velocity, and remaining are only the slow ions inside the active volume of the chamber.

The remaining positive ions inside the chamber volume continuously drift toward the cathode, according to their drift velocity, which is caused by the applied electric field. The loss of the ions by recombination effect is negligible as all electrons have disappeared from the active volume. These ions are continuously drifting toward the cathode and induce a current signal, from the measurement results discussed before, the mean value of the residual signal, which represents the positive ion signal as a function of the applied electric field is shown in Fig (6-13).

6.6. Comparison measurements with simulation

The numerical simulation discussed in chapter 2 is applied to understand the behavior of the ionization chamber and the output measured signals, the comparison illustrated below shows close agreement of the simulation with the measurements.

The simulation is used by applying 26 bar Nitrogen gas pressure and using an incoming photon flux intensity and energy calculated from the simulated synchrotron photon spectrum, after calculating the absorption 122.5 cm of air, the 1 mm carbon window at the entrance of the detector and 0.5 cm dead of volume of the same gas and pressure filled in the active volume inside the chamber shown in Fig (6-14). The total charge produced in each bin inside the chamber is calculated using Eq. (3-3) and the integrated entrance synchrotron beam profile in a timed structure by using the open and closed cycles of the chopper described by a trapezoidal function is shown in Fig (6-15).

The numerical simulation is developed using a Nitrogen recombination factor of 2.7×10^{-7}cm/s given by [33], and using electron and ion mobility from the measured values discussed in chapter 3, the ion mobilities are a constant value from table (3-1).

The loss of the charge is calculated by a recombination event every 2 ns, the diffusion and repulsion generate new charge volume and is calculated from the information taken from the previous calculation. The total charge density in each bin inside the chamber is calculated using Eq. (3-4), as well as the disturbed electric field, drift velocities, induced charges by Eq. (2-31) and the output current signal by Eq. (3-14).

The simulated output current is compared to the measured output current signal shown in Fig (6-16). It shows very good overall agreement with the measurement.

Figure (6-16) panel [A], is a reduction of the pulse height as observed when applying an electric field of 500 V/cm. With further increase of the applied voltage up to 1000 V/cm and 1500 V/cm, there is a decrease in the signal amplitude attenuation as shown in Fig (6-16) panel [B] and [C]. Saturation at the top of the signal amplitude (plateau) occurs when applying 2000 V/cm see Fig (6-16) panel [D].

From Fig (6-16) and Fig (6-19) the fast part (rise time) discussed in chapter 2, occurs for the fast signal during the open time of the chopper and is reproduced in all simulated curves with Nitrogen gas by using gas pressure of 15 and 26 bar, also showing good agreement to the measurements.

The slow part (tail signal) of the time response measurement which is shown in Fig (6-10), panel [B] describes the slow drift of the remaining ions inside the ionization chamber at different applied electric fields. Plotting the curves together from Fig (6-10), for 26 bar Nitrogen gas pressure and Fig (6-11), for 15 bar Nitrogen gas pressure, it is shown that the collection of the remaining ions is faster when applying a high electric field up to 2000 V/cm and it crosses the signal measured when applying low electric field of 1500 V/cm, 1000 V/cm and 500 V/cm as described before.

In the simulation, a small deviation from the measured signal is observed in the slow part when they are compared together. The simulated collected ions are faster than the measurements, as shown in Fig (6-16) [C] and [D] which occurs at the stronger applied electric field.

The measured residual signal of the remaining slow ions is faster than the simulated signal when applying stronger electric field from Fig (6-13), as in reality the electric field out of the beam is higher. In the simulation we assumed the first approximation in the calculation by considering the electric field only inside the beam where the ionization occurs and assuming that there is only a charge inside the beam depth, the simulation result has a good fit to the measured signals with weaker applied electric fields, as shown in Fig (6-16) [A] and [B].

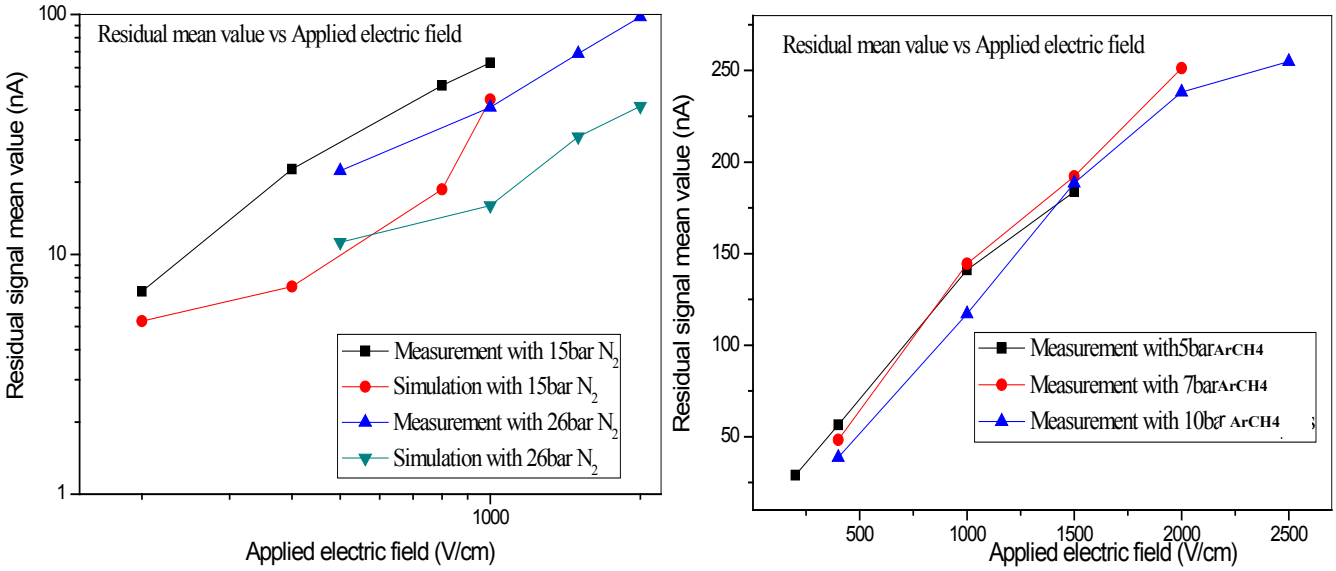

[A] [B]

Figure (6-13) Residual signal mean values for the measurement and simulation as a function of applied electric field for nitrogen gas [A]. The measured mean values of residual signal for $ArCH_4$ gas mixture of (90:10%) [B].

Another measurement of the residual signal is simulated by reducing the Nitrogen gas pressure to 15 bar. It shows a very good fit to the measurements when applying electric field of 200 V/cm and 400 V/cm. Small deviation of the simulated signal from the measurement of the slow part of the time response, is observed when applying an electric field of 800 V/cm and 1000 V/cm where the simulated signal is faster than the measurement.

The simulated amplitude signal fits well to the measurement and shows the same effect that occurs with the measurement and also has a good fit to the strong attenuation at the top of the amplitude signal, which occurs according to the space charge effect described before, when operating the chamber with low power electric field and the plateau observed in the simulated signal at greater applied electric field near saturation.

The signal decline (fall time) during the closed time of the chopper, which reduces the incoming photon flux is simulated and has good fit to all measurements, as shown in Fig (6-16) and Fig (6-19).

6.6.1. Simulation parameter

The most important parameters which affect the time response signal shape is the applied electric field, gas pressure and recombination factor. Increasing the gas pressure it increases the charge density inside the ionization chamber in each bin. This leads to a higher value of the simulated signal according to the high number of charges which are collected at the outer plates. By increasing the applied electric field value in the program, it increases the drift

velocity of the charges, ass given by Eq. (2-3) and Eq. (2-4), accordingly, the fast drift of the charged particles which leads to fast collection and increases the value of the total integrated charge on the outer plates. This delivers high values for the simulated output current signal. The plateau is observed at the top of the simulated time response signal when applying an electric field value of 1000 V/cm with 15 bar Nitrogen gas and 2000 V/cm with 26 bar Nitrogen gas pressure.

The simulated parameters are summarized in table (6-2) for both 26 bar and 15 bar nitrogen gas pressures, and tunings of the electric field from 200 V/cm up to 2000 V/cm.

Table 6-2: Simulation parameters of the time response signal for Nitrogen gas.

Simulation parameter	15 bar N_2				26 bar N_2			
Applied Electric field V/cm)	200	400	800	1000	500	1000	1500	2000
Rec_factor (α) cm^3/s	2.7E-7	2.7E-7	2.7E-7	2.7E-7	2.7E-7	2.7E-7	2.7E-7	2.7E-7
Rec_Correction num	3.5E-7	5.8E-7	5.4E-7	7.7E-7	2E-7	2.3E-7	3.1E-7	4E-7
P_{air} g/cm^3	1.25E-3	1.25E-3	1.25E-3	1.25E-3	1.25E-3	1.25E-3	1.25E-3	1.25E-3
μ_{N2} cm^2/g	1.53	1.53	1.53	1.53	1.53	1.53	1.53	1.53
Trapezoidal- (a)/ ns	0	0	0	0	0	0	0	0
Trapezoidal- (b)/ ns	15.5E+3	15 E+3	13 E+3	16 E+3	16 E+3	16 E+3	16 E+3	16 E+3
Trapezoidal- (c)/ ns	50 E+3	50 E+3	49 E+3	51 E+3	49 E+3	50 E+3	51 E+3	51 E+3
Trapezoidal- (d) /ns	70 E+3	68 E+3	66.5 E+3	70 E+3	67 E+3	67 E+3	67 E+3	67 E+3
Residual time/ ns	90 E+3	90 E+3	90 E+3	90 E+3	90 E+3	90 E+3	90 E+3	90 E+3
ions factor	2	2	5	6	2	2	5	5

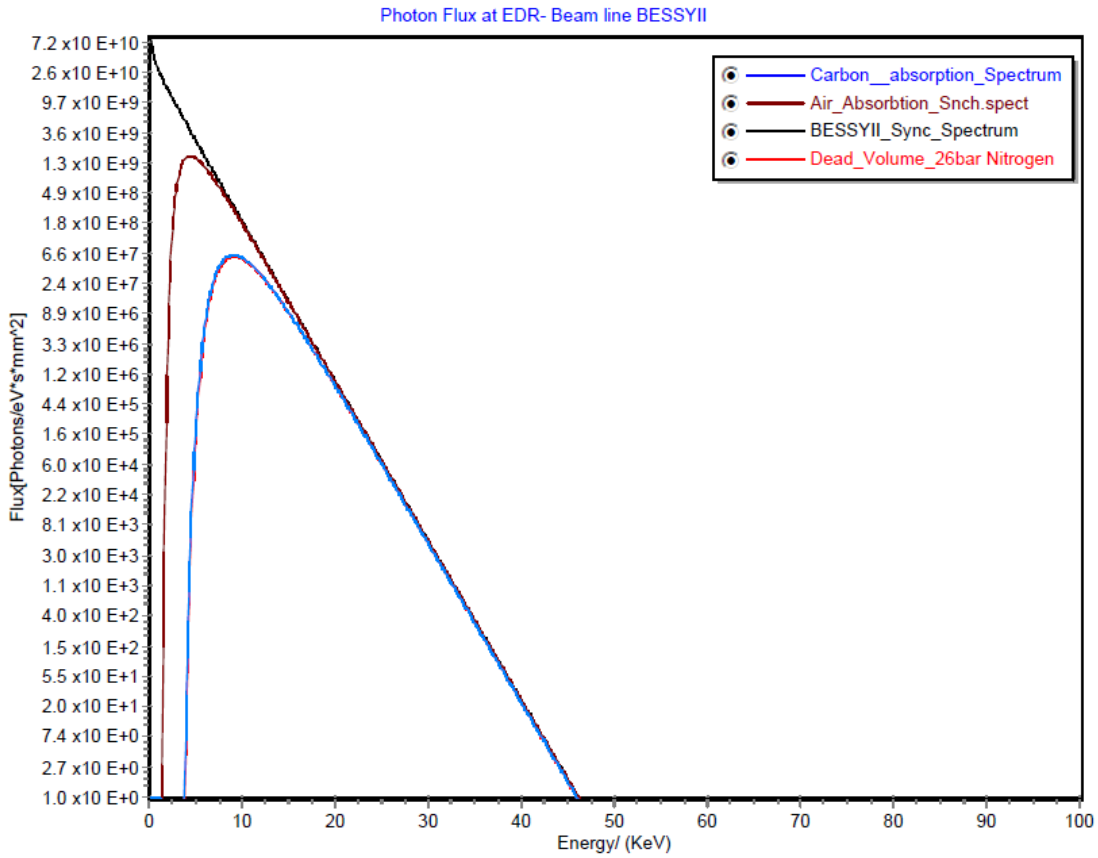

Figure 6-14: Synchrotron photon absorption by 26 bar Nitrogen gas inside the multi-channel ionization chamber.

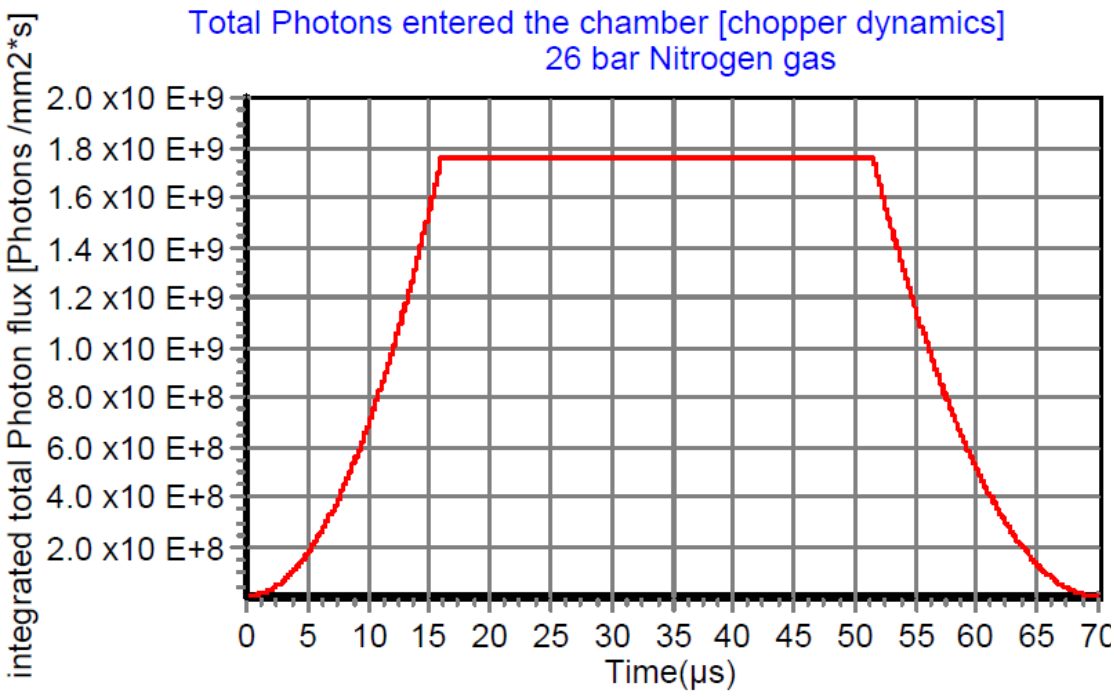

Figure 6-15: The total integrated synchrotron photon flux from Fig (6-8), entering the ionization chamber as a function of time.

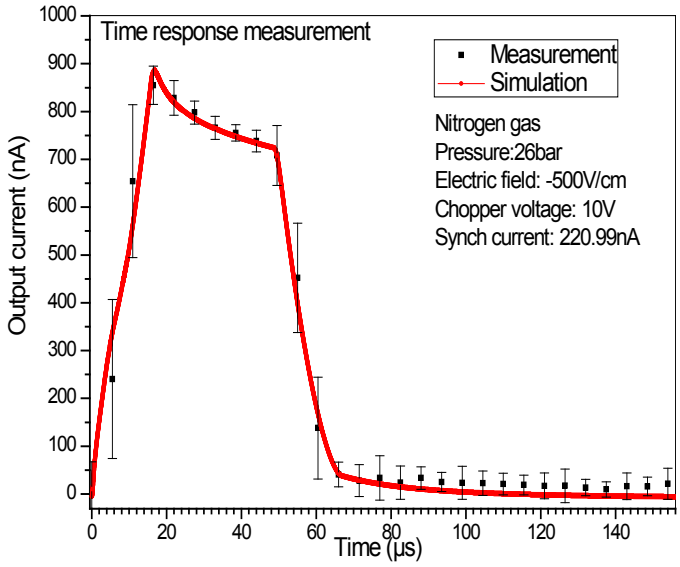

[A]

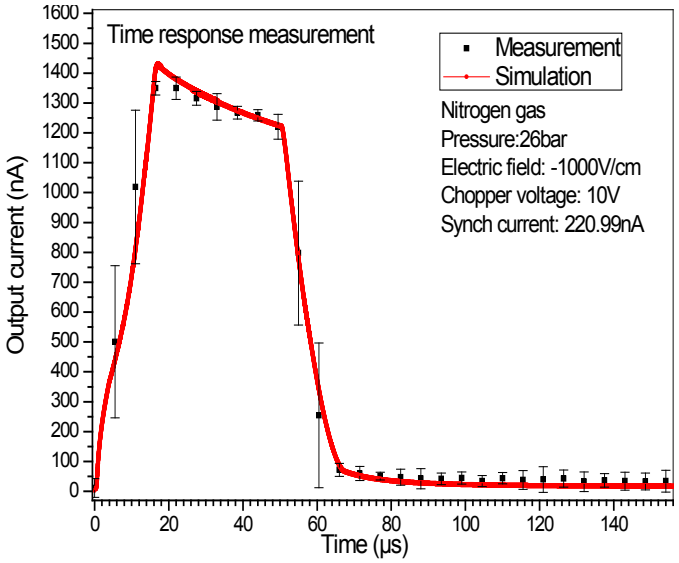

[B]

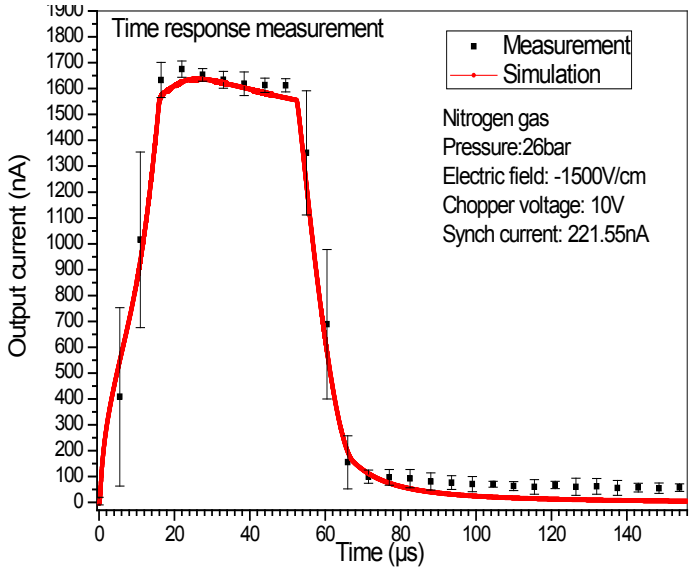

[C]

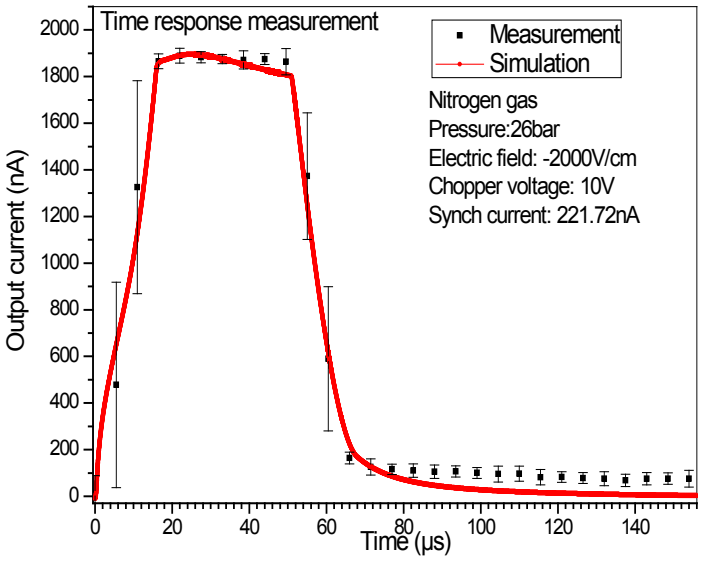

[D]

Figure 6-16: The simulated results discussed before compared to the measurement results shown in Fig (6104). The output current signal as a function of applied electric field for 26 bar Nitrogen gas pressure.

Another simulation is done by changing the Nitrogen gas pressure to 15 bar using the simulation method and parameters described before. By changing the gas pressure to 15 bar and using the simulated synchrotron spectrum shown in Fig (6-17), and tuning the electric field from 200 V/cm to 1500 V/cm with the same values used in the measurement shown in Fig (6-11), the simulated output current signal has good agreement with the measurements, as shown in Fig (6-19) below.

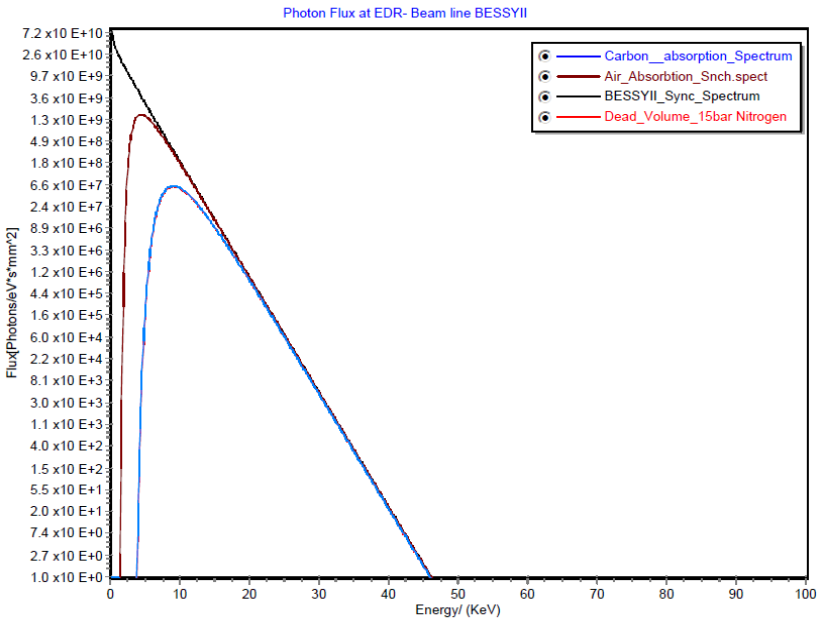

Figure 6-17: Synchrotron photon absorption by 15 bar Nitrogen gas pressure filled inside the Multi-channel ionization chamber.

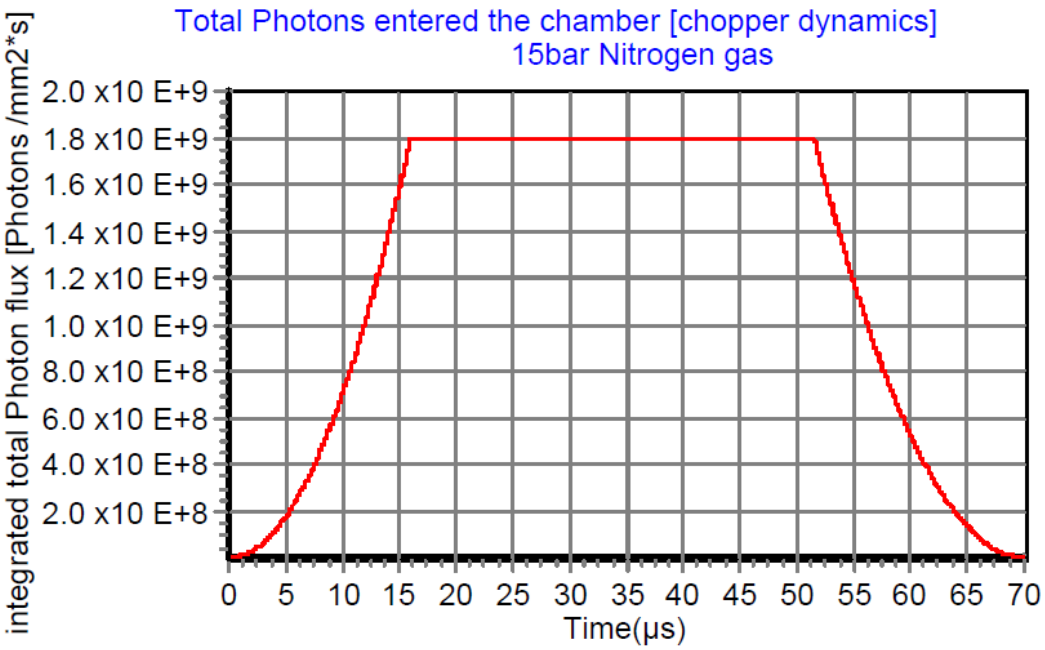

Figure 6-18: The total integrated photon flux from Fig (6-16), entering the ionization chamber as a function of time.

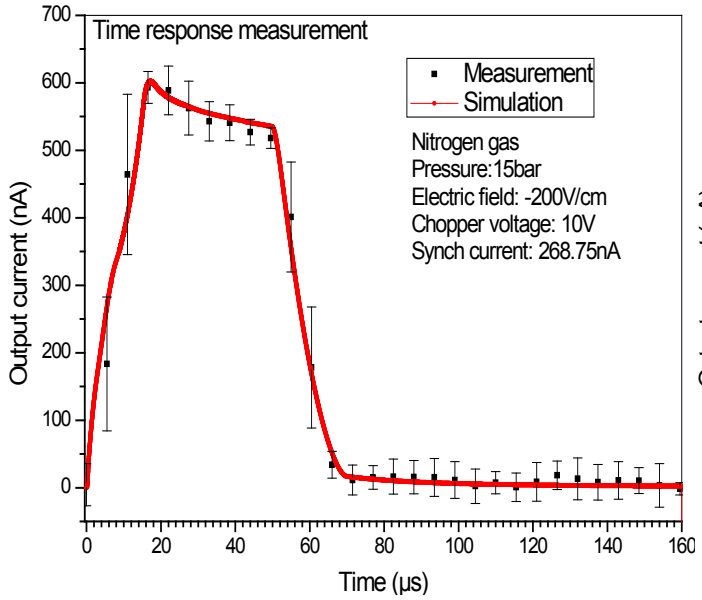

[A]

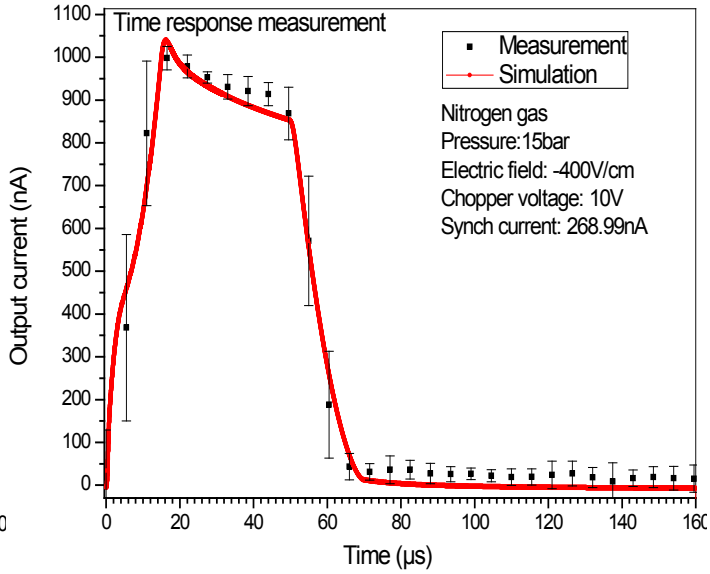

[B]

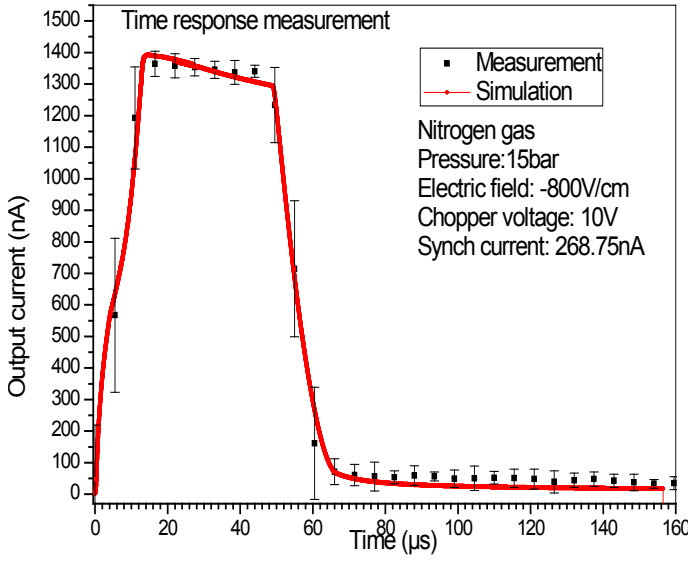

[C]

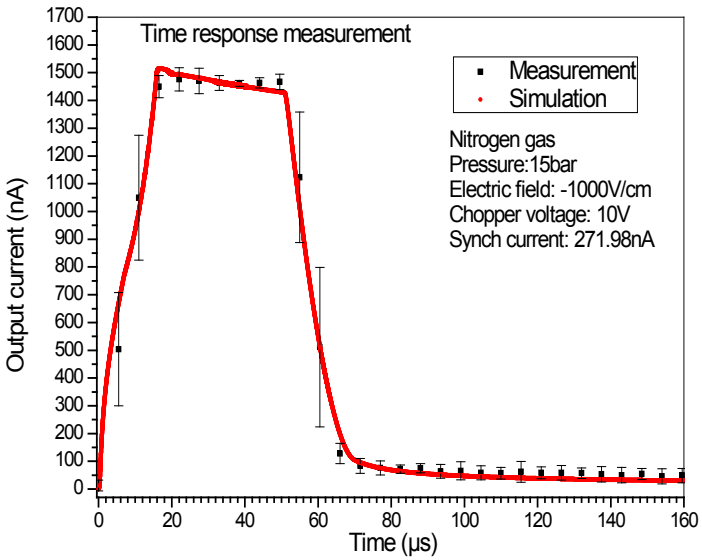

[D]

Figure 6-19: The simulated output current signal as a function of applied electric field is compared to the measurement signal shown in Fig (6-11) for 15 bar Nitrogen gas pressure.

Chapter 7 Discussion and conclusion

7. Space charge effects

To study the charge dynamics behavior and the space charge effects inside the multi-channel ionization chamber (MIC) with a chamber geometry shown in Fig (7-1), the results from the numerical simulation using 7 bar $ArCH_4$ gas mixture of (90%:10%), an applied electric field of -400 V/cm and the recombination factor of $25x10^{-6}$ cm^3/s are used including the chopper geometry discussed in chapter 3, with frequency of 37.4 Hz and the simulated photon flux for the synchrotron radiation spectrum shown in Fig (3-3) in chapter 3. The simulation program runs till 400 µs and the chopper closed after 89 µs as shown in Fig (7-2) below.

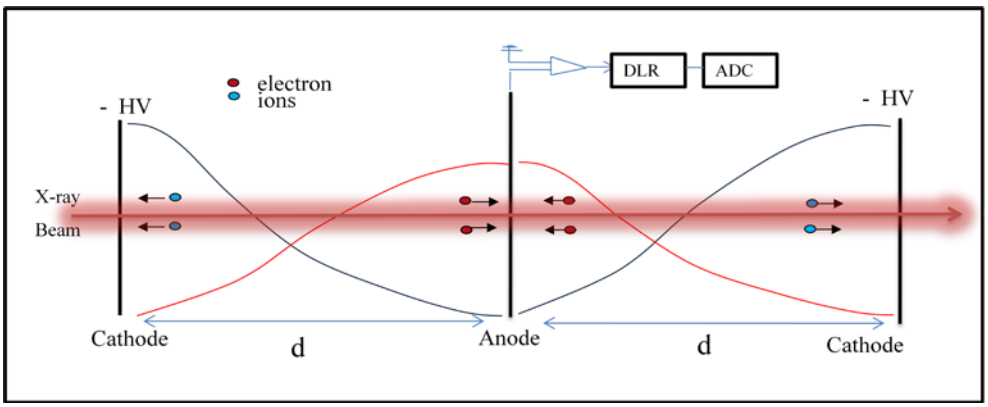

Figure 7-1: The detector geometry; divided into two parts. The photon beam is coming from the left side. The cathode plates on the left and right side and the anode in the center.

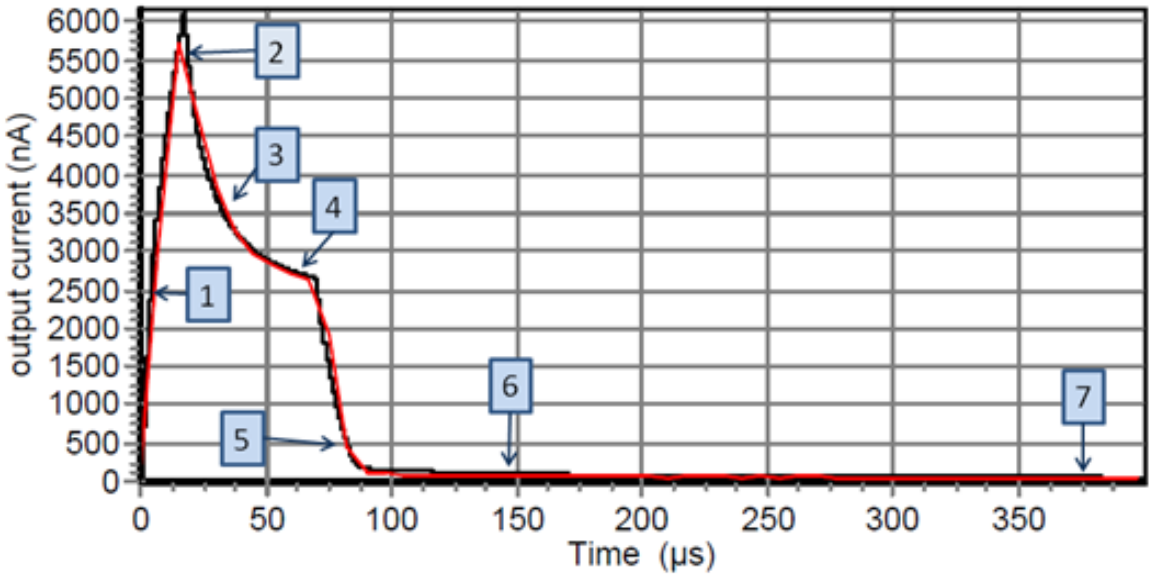

Figure 7-2: The measurement current (red) with 7 bar $ArCH_4$ and the applied electric field of 400 V/cm, simulation curve (black).

Figure (7-2) shows the space charge effect in the decay of the current signal. The long tail on the end represents the positive ions collection time. The labeled region has been chosen to represent the physics processes inside the chamber as shown above.

{1} when the lead slit chopper starts opening, the incoming photon flux will increase thus the produced charge will also increase.

{2} Maximum opening of the slit chopper and the full beam enters the chamber which should result in a flat top.

{3} Continuous illumination of the full beam and drop in the signal is observed according to the recombination and accumulation of the space charge inside the chamber, which affects the electric field and consequently the measured signal.

{4} The equilibrium states where there is no more drop in the signal.

{5} Closing of the chopper which decreases the incoming photon flux to zero.

{6} The chopper is closed and no more photons are arriving. This reduces the electron density in a short time to zero, due to their fast drift velocity compared to the ions which are still remaining inside the chamber volume.

{7} The ion density inside the chamber decreases due to the accumulation at the cathode. The measured signal decreases as the charge column is absorbed until no charge is left.

7.1.1. Ions density distribution

Positive ions distribution inside the chamber in each region of interest as described in Fig (7-2) is shown in Fig (7-3). At Region, [1] the ions density is relatively low since there are less photons which enter the chamber, [2] the ions density is increased due to the increasing of photon flux, [3] during continuous illumination the electrons and ions intermix and result in a reduction of free charges due to recombination, [4] equilibrium state of the chamber. The number of produced ions is equal to the ions lost by the accumulation at the cathode and recombination process [5] the chopper is closing, no ions generated and no ions are lost [6]. This eliminates the loss of the ions by recombination process and the ions density therefore decreases only by accumulation at the cathode. [7] The ions density is continuously reduced near the cathode and it dropped to zero near the anode because the ions drift towards the cathode plate.

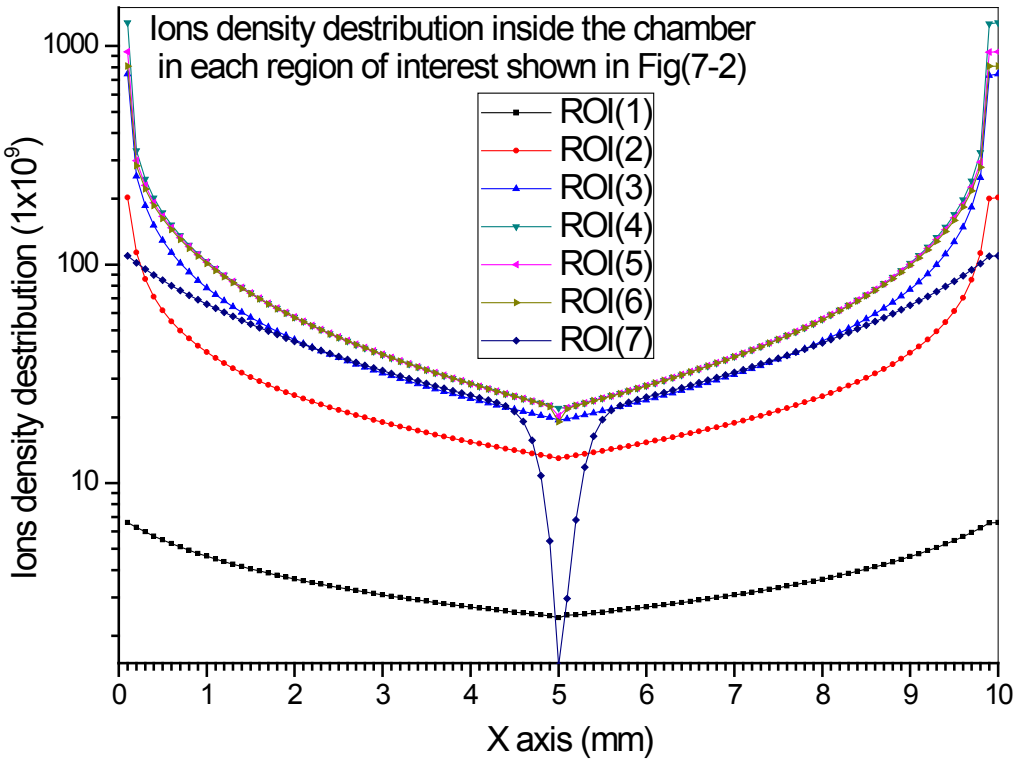

Figure 7-3: The ions density distribution in each region from Fig (7-2), it shows the increased density when the incoming photons flux increases at regions [1], [2], [3] and equilibrium at region[4], the density decreases on the regions [5], [6] and [7].

7.1.2. Electron density distribution

The electron density distribution inside the chamber is taken in each region of interest as defined in Fig (7-2). In region [1], a high electron density is obtained near the anode and few near the cathode since electrons drift rather fast towards the anode, [2] a higher electron density is observed according to increasing of the photon flux (until the full opening chopper is reached), [3] a decrease of the electron density according to the recombination and fast collection time, [4] at equilibrium there is a reduced electron density according to the continuous recombination process and collection process, [5], [6] and [7] the chopper is closed. There are no electrons in the chamber since all remaining electrons are collected fast.

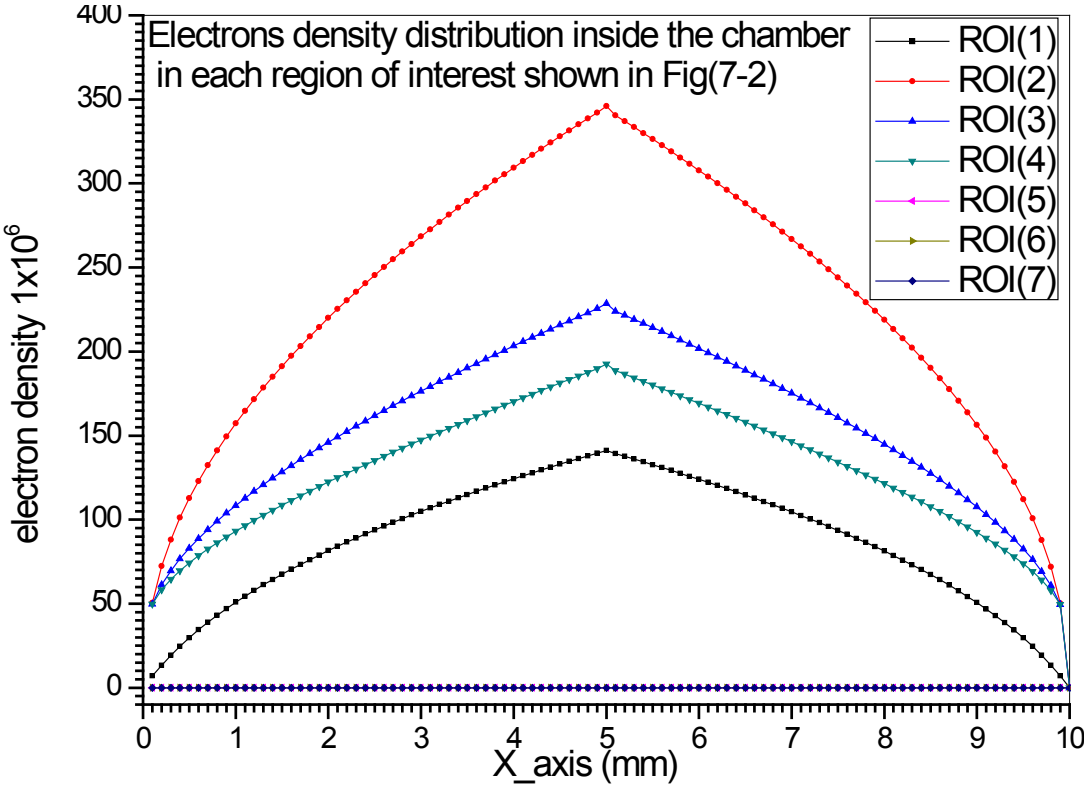

Figure 7-4: Electron density distribution inside the chamber in each region of interest shown in Fig (7-2), it shows that the electron density increases with the incoming photons flux and decreases to zero when the chopper closed.

7.1.3. Electric field distribution

The slow movement of the ions inside the chamber disturbs the applied electric field as shown in Fig (7-5). The electric field distribution inside the chamber is shown in Fig (7-2) for each region of interest. Region [1], there is small distortion of the applied field which seems to be negligible, [2] the increased ions density leads to more distortion of the electric field, [3] there is further increase of space charge when the chamber is continuously illuminated with the full beam, [4] in equilibrium state the recombination decreases the space charge inside the chamber volume, [5] and [6] the electric field stays almost constant. There is a decreasing in photon flux down to zero and according to the low drift velocity of the positive ions representing in total the space charge which leads to low collection time, [7] there is a decrease of space charge due to the ions collection at the cathode with time and consequently an increase in the electric field

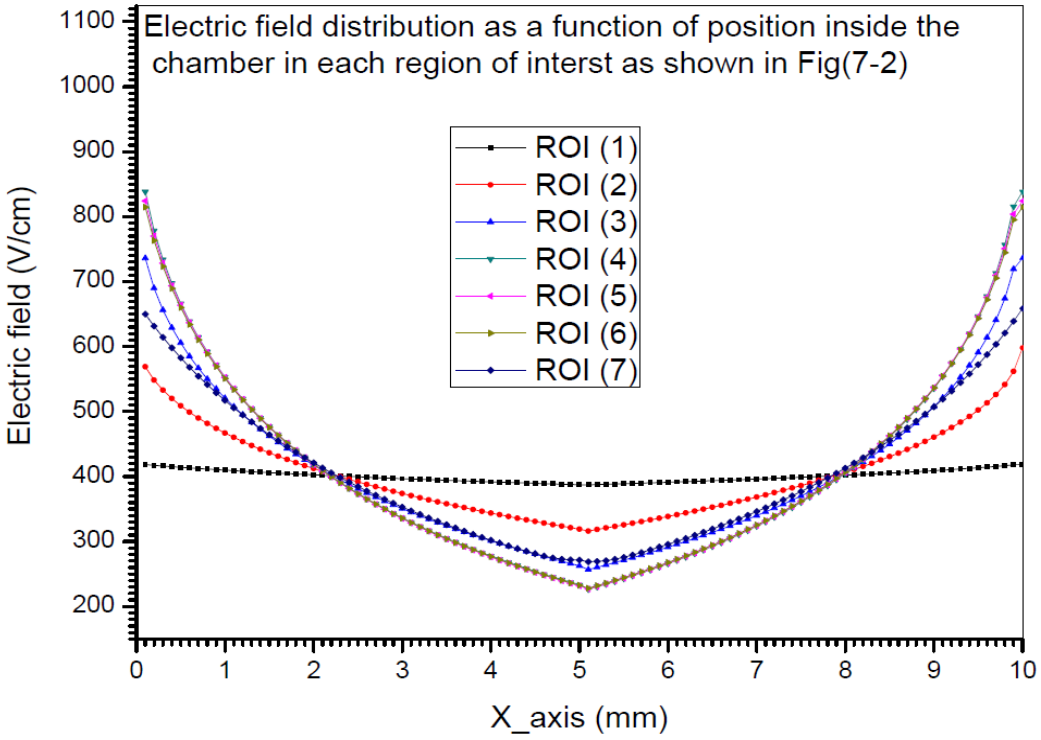

Figure 7-5: Electric field distortion according to the space charge inside the chamber in each region of interest shown in Fig (7-2).

7.1.4. Distribution of electrons and ions drift velocities

The relationship between the electric field and drift velocity is given by Eq. (2-3) and Eq.(2-4). The positive ion drift velocity distribution is shown in Fig (7-6), and the electron drift velocity distribution Fig (7-7) below, at each region of interest from Fig (7-2 reflecting the fact that the drift velocity is dependent on the electric field. when the electric field increases the drift velocity increases from Fig (7-5).

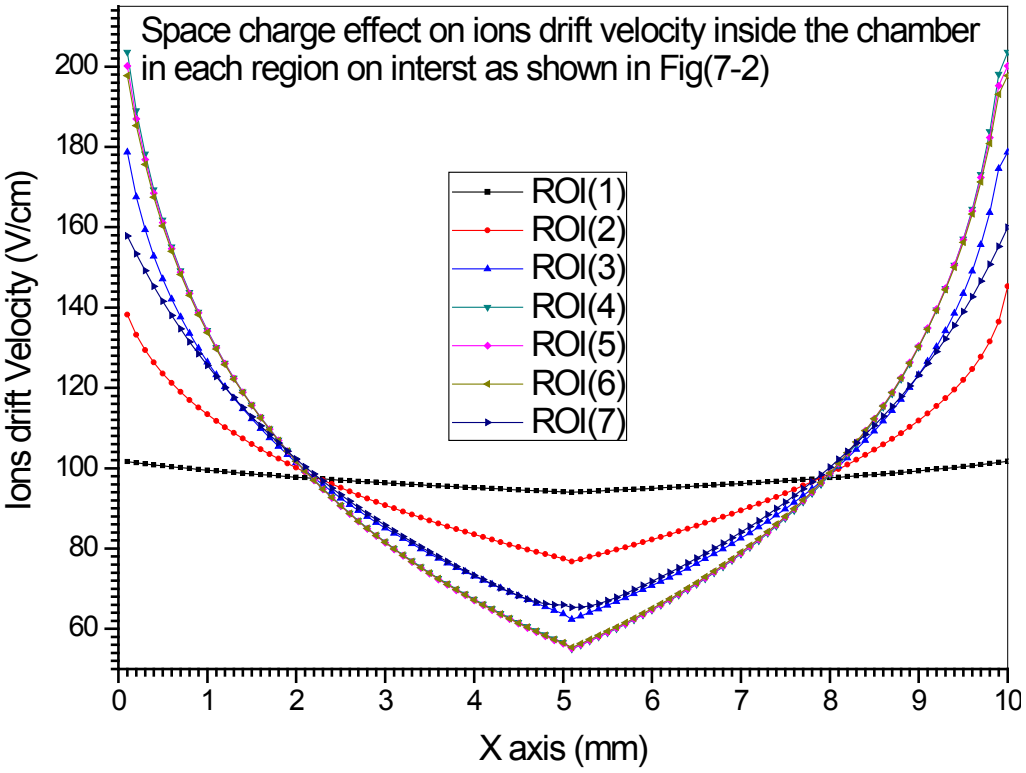

Figure 7-6: The ions drift velocity distribution inside the chamber in each region of interest, it changes linearly with the electric field.

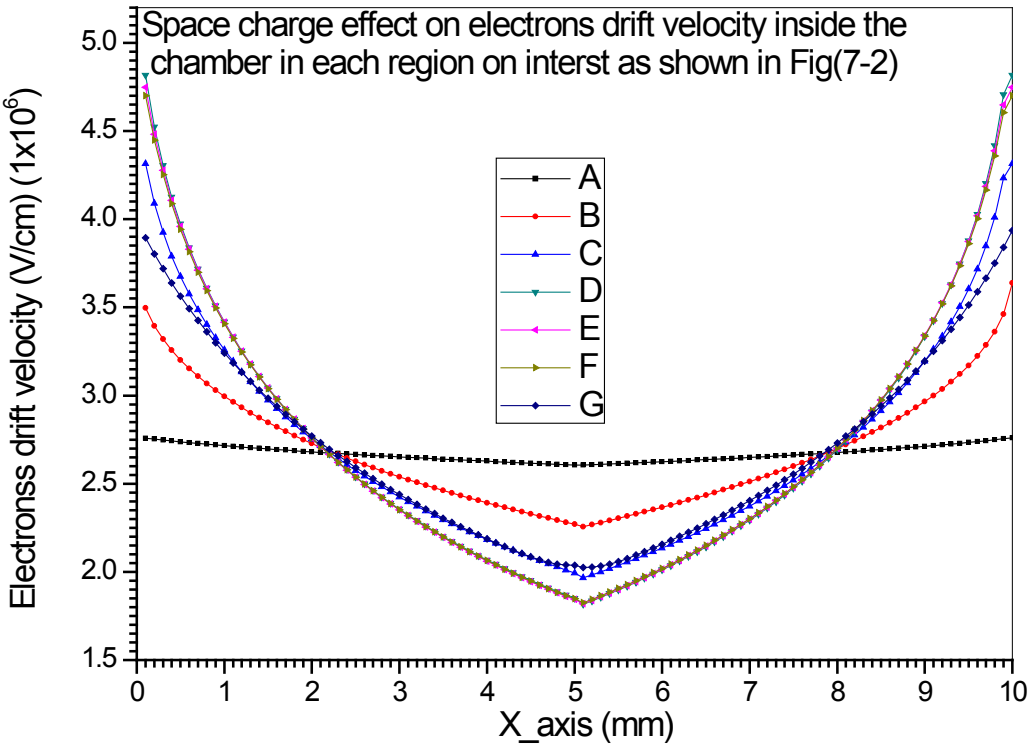

Figure 7-7: The linear relationship between the electric field and the electron drift velocity as well when the electric field increases the drift velocity increases from Fig (7-5).

7.2. Conclusion and outlook

From the measurements and discussions shown in this thesis it can be concluded that:

- The optimum operation of the ionization chamber is recommended by applying high voltage of -1 kV in the saturation region for 10 bar $ArCH_4$ gas mixture of (90:10%) with different X-ray photon intensities as shown Fig (7-8) below.

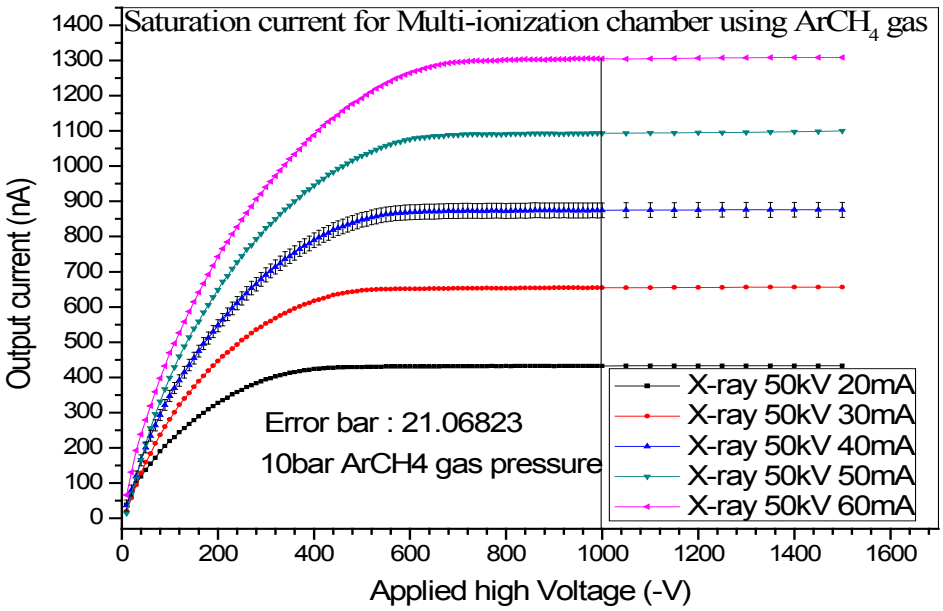

Figure (7-8) shows the optimum operation voltage of the Multi-ionization chamber at the saturation current with different photon intensities.

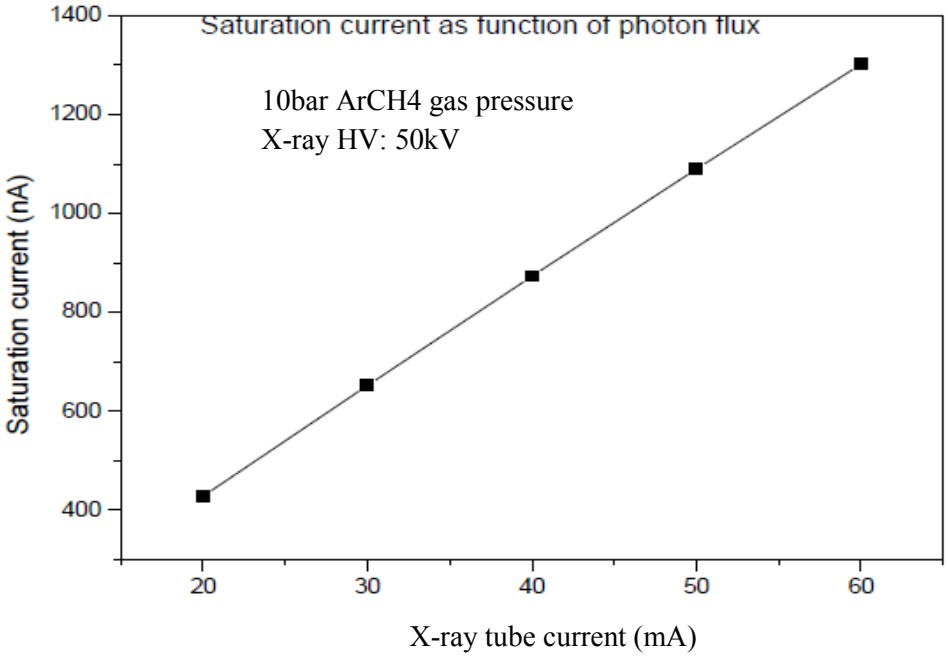

Figure 7-9: Relationship between the saturation current and X-ray tube current from above figure, which has a linear relation with the X-ray photon intensity.

- The linearity of the chamber response with different photons intensities is measured with $ArCH_4$ gas mixture and Nitrogen gas. A line spread function is measured at 15 bar $ArCH_4$ and applying high voltage of -1 kV. By scanning the Multi-Channel Ionization Chamber horizontally the FWHM is found to be (0.228 mm). This is sufficient to guarantee the separation between the anode pads.
- The simulation reproduces in most aspects the experimental results and can used to predict the time response profile changing different gases and parameters.
- The space charge effect due to the high positive ion density inside the chamber volume depending on the applied electric field is qualitatively understood in the simplifying field approximation used.
- The decrease of the signal amplitude measured as function of applied electric field shows good agreement with the simulation.
- The diffusion and repulsion effects are only understood qualitatively since the simulation does not include effects perpendicular to the drift as discussed before.
- For the optimum detector operation it is necessary to choose the right gas filling and Pressure. Besides the space charge effects and recombination it has to be taken into account that the attenuation of the incoming beam is small but sufficient to reach the desired precision. Using gases with very small attenuation coefficient will produce a small number of electron ion pairs. Therefore for optimum operation the following gas choice and pressure should be used:

  i- High pressure + big gap

  ii- Low pressure + medium gap

  iii- High pressure + small gap (free of gas choice)

- In this work pure nitrogen gas is used. Argon gas mixed with methane meets this requirement at low pressure but has the problem that the x-ray fluorescence photons from the K-shell have a rather large range which affects the spatial resolution.
- The slow tail of the signal caused by the movement of the positive ions accentuated by the low drift field caused by the generated space charge is a serious problem when high speed imaging is considered. It may be conceivable to develop a correction algorithm of the space charge effects using the dynamics found in the actual work.

7.3. Summary

Medical imaging with synchrotron radiation has a broad spectrum of applications in particular when high speed or high precision is require, which cannot be seen by the normal clinical imaging techniques.

A Multi-Channel Ionization Chamber (MIC) has been successfully developed, and the most important characteristics and calibrations have been measured. The saturation characteristics for a broad beam have been determined with an X-ray generator with characteristic energy of 17.44 keV Molybdenum anticathode. By regulating the tube current different photon intensities are obtained which are used for the measurements.

The theoretical calculation of the physical interaction of the photons with the active gas volume is considered for the chamber design geometry and construction.

The saturation current as a function of applied electric field is measured by filling the chamber with different gas types and pressures.

A numerical simulation is carried out to investigate the charge dynamics as drift, diffusion and repulsion as well the disturbance of the homogeneous applied electric filed considering the space charge and recombination effects inside the gas chamber in a steady state.

In order to observe the dynamic effects a time response measurement is carried out on the EDR beam line at BESSYII. A lead chopper of 1 mm slit is used to modulate the synchrotron photon intensity as a function of time, and recording the output current signal. By regulating the applied electric field from recombination regime up to the saturation regime, the space charge effect and recombination is investigated with different gas pressure of $ArCH_4$ gas mixture and Nitrogen gas. At beam intensities where space charge and recombination are present it is observed that shortly after onset of the beam a peak current is reached which settles down to an equilibrium value typically after the maximum electron drift time. After switching off the beam the current drops again in a time corresponding to the electron drift time leaving only the ion current. The latter produces a long tail where the complete disappearance is further delayed due to the lowered electric field caused by the remaining space charge.

Appendix A

The following time response measurements are taken using the setup in Fig (6-1), and applying pressure of 7 bar and 5 bar of $ArCH_4$ gas mixture of (90%:10%), and tuning he applied electric field from 200 V/cm to 2000 V/cm, Fig (A-1) and (A-2) panel [A], shows the change of the amplitude signal according to the space charge effect where strong attenuation occurs at low electric field and plateau at the high applied electric field.

Fig (A-1) and (A-2) panel [B], represent the slaw part signal from the remaining positive ions in which the positive ions collected faster at high applied electric field and need longer time to collect at low applied electric field.

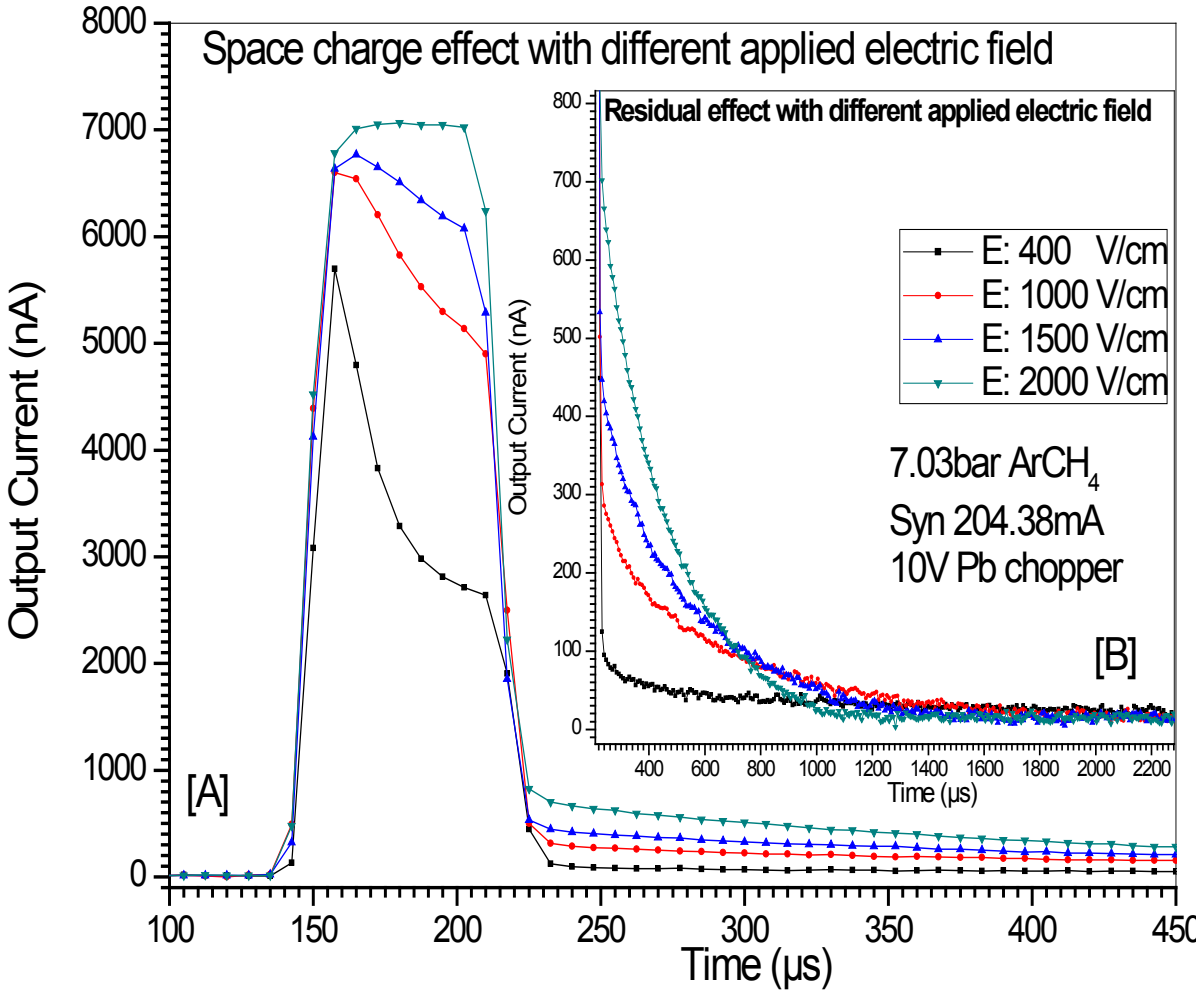

Figure A-1: This figure shows the time response of 7 bar $ArCH_4$ gas pressure using the setup shown in Fig (6-1), the same effect as 10 bar signal except that it reaches the plateau at applied electric field of 2000 V/cm [A]. Magnified long tail signal [B].

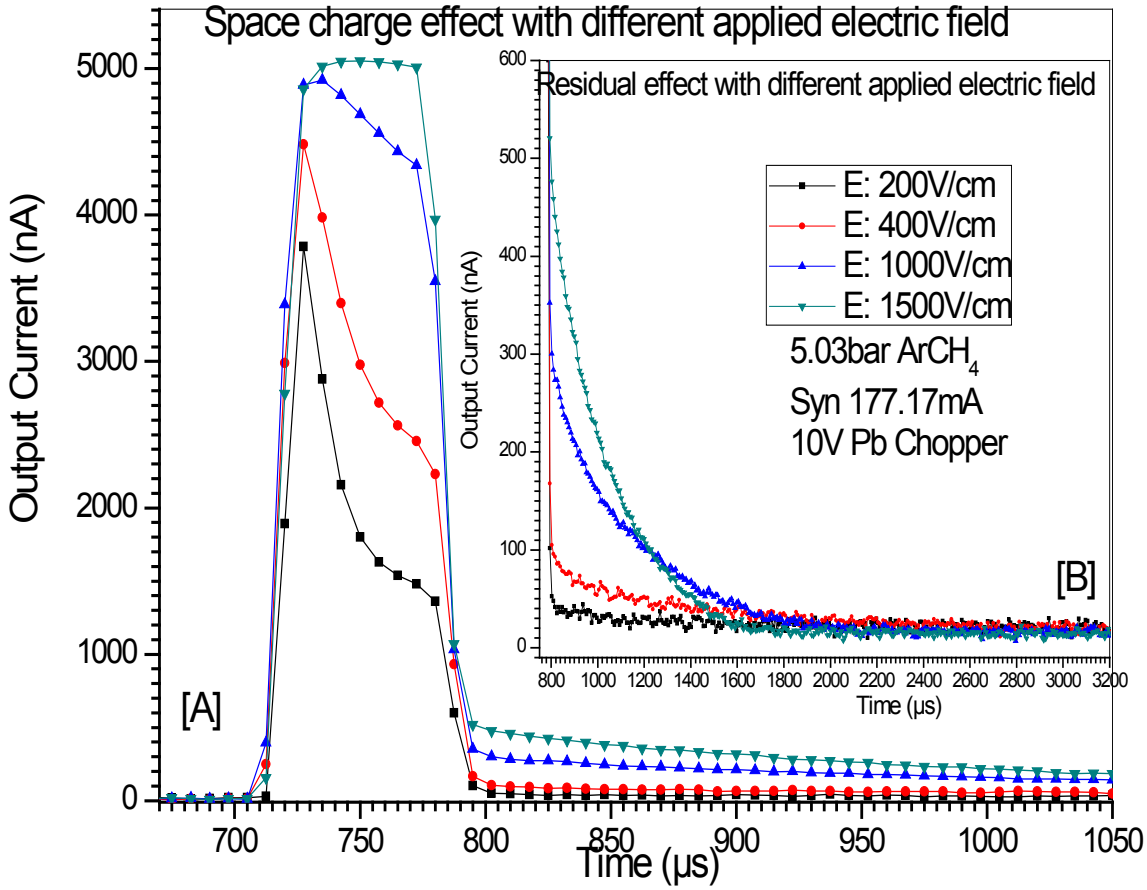

Figure A-2: This figure shows the time response of 5 bar $ArCH_4$ gas pressure using setup shown in Fig (6-1), the same effect as 10 bar signal except that it reaches the plateau at applied electric field of 1500 V/cm [A]. Magnified long tail signal [B].

Appendix B:

B-1. Electric field calculation

By the symmetry of the ionization which occurs by the pencil like synchrotron beam and there is homogenous distribution of the charge throughout the chamber depth around the beam. By assuming that there is no change in the angular dependent and considering the total charge distribution will be around the beam which has radial symmetry. The maximum value of the radial dependent R will not play important role in the calculation and the mean value is taken into account in the calculation.

By dividing the chamber depth in the x-axis into small binning, using this assumption will give a good approximation to use the gauss's formula to calculate the change of the electric field in each bin as shown below.

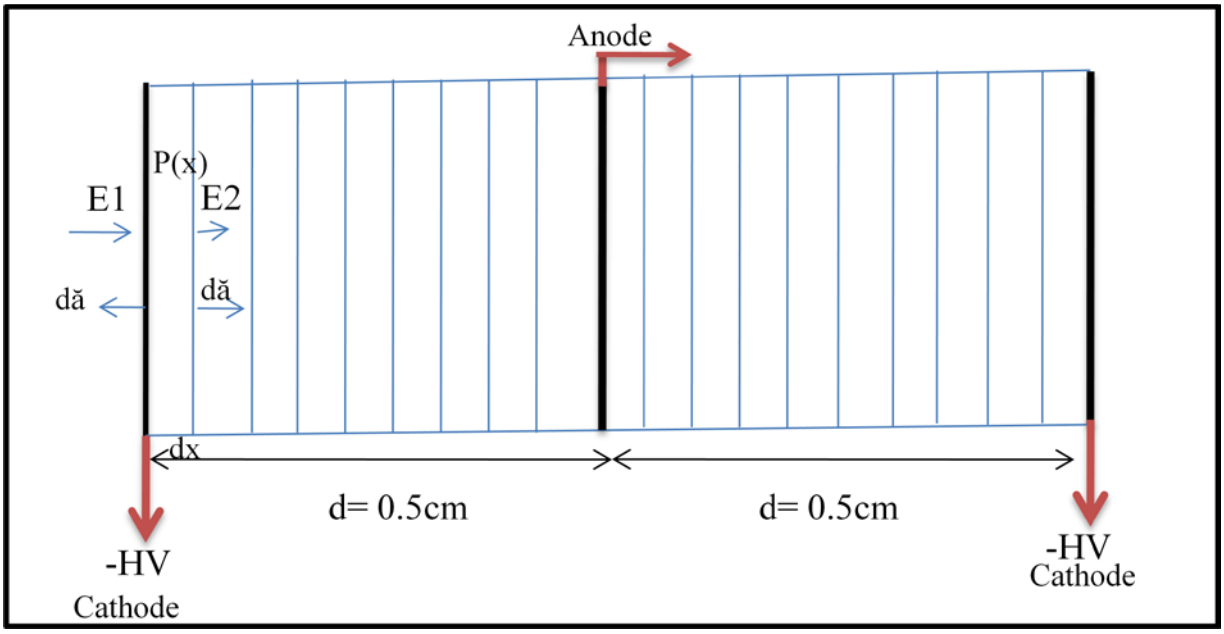

Figure B-1: Sketch diagram of the detector depth in the *x* direction divided into small binning cathode plate in the left side and anode in the right side.

At the first bunch the charge density is constant and homogenous throughout the chamber volume. The calculation the electric field difference in each bin surface from Gauss's law and Maxwell's equation as following

$$\frac{E_2 - E_1}{\Delta x} = \frac{\Delta E}{\Delta x} = \frac{\rho_i}{\varepsilon_0} \qquad (1)$$

$$\nabla \cdot E_i = \frac{\rho_i}{\varepsilon_0} \tag{2}$$

Where *i* is the bin number

$$\int_0^d \bar{E}\ \overline{ds} = U_0 \tag{3}$$

Were U_0 is the applied high voltage, *ds* is the small surface area for each bin.
The mean electric field is constant $\bar{E}$= constant then:

$$|\bar{E}|.d = U_0 \tag{4}$$

Assume that there is no change in the *y* and *z* direction and the charge drift only in *x* direction equation (3) become

$$\int_0^d E(x)dx = U_0 \tag{5}$$

A difference of the electric field between each bin can be calculated as following
From Fig (B-2), the electric field in each bin is given by:

$$\begin{cases} E_1 = E_0 \\ E_2 = E_0 - \Delta E_1 \\ E_3 = E_0 - \Delta E_1 - \Delta E_2 \\ . \\ . \\ . \\ E_n = E_0 - \Delta E_1 - \Delta E_2 - \Delta E_3 \ldots - \Delta E_{n-1} \end{cases} \tag{6}$$

The total electric field from equation (5), and substitute the values of electric field in each bin

$$E_1 \Delta x + E_2 \Delta x + E_3 \Delta x + \ldots . + n\, E_n \Delta x = U_0 \tag{7}$$

Dividing equation (6) by Δx

$$E_0 + E_0 - \Delta E + E_0 - 2\,\Delta E + \ldots\ldots\ldots E_0 - (n-1)\,\Delta E = U_0/\Delta x \tag{8}$$

By separating variables equation (12) becomes

$$nE_0 - n\,((n-1)/2)\,\Delta E = U_0/\Delta x \tag{9}$$

$$nE_0 = U_0/\Delta x + n\,((n-1)/2)\,\Delta E \quad (10)$$

Dividing equation (10) by *n*,

$$E_0 = U_0/\Delta x\, n + ((n-1)/2)\,\Delta E \quad (11)$$

Sub $d = n * \Delta x$

$$E_0 = U_0/d + ((n-1)/2)\,\Delta E \quad (12)$$

The iteration method on equation (12) and (7) is used to calculate the electric field change in each bin in the chamber depth. The applied high voltage is known and the total distance *d* is constant value. Thus the total electric field inside the active volume can calculated. Taking into a count that the electrons and ions drift and the recombination process occurs each time. Assuming that the positive ions concentration is constant with a homogenous illumination of X-ray in one shot.

B-2 Recombination

The rate of recombination in the detector can evaluated quantitatively by considering the n^+ and n^- the ion and electron densities respectively if α is the recombination coefficient as

$$\frac{dn-}{dt} = -\alpha n^+ n^- \quad (13)$$

$$\frac{dn+}{dt} = -\alpha n^+ n^- \quad (14)$$

Become $\frac{dn-}{dt} = \frac{dn+}{dt}$

$$\frac{d(n^- - n^+)}{dt} = 0 \quad (15)$$

After integration we get

$$n^- - n^+ = c \quad (16)$$

Were the negative sign denotes the reduce of the number of charge d particle with time [12].

If the electron density and ion density are equal then we get

$$\frac{\mathrm{dn}}{\mathrm{dt}} = -\alpha \mathrm{n}^2 \tag{17}$$

If recombination is taking place on the time interval from $t = t_0 \ to \ t = t$ and the density of the charged particle at $t = t_0$ is n_0 by integrating the equation (15) we get

$$n = \frac{n_0}{1+\alpha n_0 t} \tag{18}$$

Sub equation (16) in equation (14)

$$\frac{dn+}{dt} = -\alpha n^+(n^+ + c) \tag{19}$$

If $\alpha n^+ = n$ and $dn = \alpha \, dn^+$

Then sub in (19)

$$\frac{1}{\alpha}\frac{dn}{dt} = -\frac{1}{\alpha}\mathrm{n}^2 - \mathrm{nc} \tag{20}$$

$$\frac{dn}{dt} = -\alpha n^2 - \alpha nc \tag{21}$$

$$\frac{dn}{n^2+\alpha nc} = -dt \tag{22}$$

Solution of (22) is then by taking the roots

$$n^2 + \alpha nc + (\frac{\alpha c}{2})^2 = (\frac{\alpha c}{2})^2 \tag{23}$$

$$n + \left(\frac{\alpha c}{2}\right) = \pm\left(\frac{\alpha c}{2}\right) \tag{24}$$

The roots is

n_1= - α c; n_2= 0

$$\frac{1}{n^2+\alpha nc} = \frac{1}{n(n+\alpha c)} = \frac{A}{n+\alpha c} + \frac{B}{n} = \frac{nA}{n(n+\alpha c)} + \frac{(n+\alpha c)B}{n(n+\alpha c)} = \frac{(nA+nB+B\alpha c)}{n(n+\alpha c)} \quad (25)$$

$$\frac{1}{n(n+\alpha c)} = \frac{n(A+B)+B\alpha c}{n(n+\alpha c)} \quad (26)$$

Then

$$n(A+B) + B\alpha c = 1$$

$$A = -B; \qquad B = \frac{1}{\alpha c}\ ;\ A = -\frac{1}{\alpha c}$$

Substitute the values of the roots *A* and *B* in equation (22)

$$\frac{1}{n(n+\alpha c)} = \frac{-\frac{1}{\alpha c}}{n+\alpha c} + \frac{\frac{1}{\alpha c}}{n} = -dt \quad (27)$$

Multiply by (–) we got

$$\int_n^{n0} \frac{dn}{(n+\alpha c)} - \int_n^{n0} \frac{dn}{n} = -\alpha c \int_t^{t0} dt \quad (28)$$

After integration

$$\ln(n+\alpha c) - \ln(n) = \alpha c\ t \quad (29)$$

Substitute the integration limits

$$\ln(n+\alpha c) - \ln(n_0+\alpha c) - (\ln(n) - \ln(n_0)) = = \alpha c\ (t - t_0) \quad (30)$$

Separation variables we got

$$\ln\frac{(n+\alpha c)}{(n_0+\alpha c)} - \ln\frac{(n)}{(n_0)} = \alpha c\ (t - t_0) = \ln\frac{(n_0+\alpha c)}{(n+\alpha c)} - \ln\frac{(n)}{(n_0)} = -\alpha c\ (t - t_0) \quad (31)$$

Separation and multiply by exponential

$$\frac{(n_0+\alpha c)n}{(n+\alpha c)n_0} = \mathrm{e}^{-\alpha c\,(\mathrm{t}-\mathrm{t}_0)} \tag{32}$$

Cross product

$$(n_0 + \alpha c)n = (n + \alpha c)n_0 e^{-\alpha c\,(\mathrm{t}-\mathrm{t}_0),} \tag{33}$$

Separation variables

$$n\left(n_0 - n_0 e^{-\alpha c\,(\mathrm{t}-\mathrm{t}_0)} + \alpha c\right) = \alpha c n_0 e^{-\alpha c\,(\mathrm{t}-\mathrm{t}_0)} \tag{34}$$

$$n = \frac{\alpha c n_0 e^{-\alpha c\,(\mathrm{t}-\mathrm{t}_0)}}{\left(\alpha c + n_0(1-e^{-\alpha c\,(\mathrm{t}-\mathrm{t}_0)}\right)} \tag{35}$$

Using $n^- - n^+ = c$ when $c \overset{\Delta}{\rightarrow} 0$

Then we get

$$n = \frac{n_0}{1+\alpha n_0 t} \tag{36}$$

Using Boag formula to calculate t which is given by [9].

$$t = \frac{da}{(\mu_{ion}+\mu_{elect})E} \tag{37}$$

Were t is the time needed to for all ions and electrons to arrive to the cathode and anode respectively, $\mu_{(ions)}$ is the mobility of the ions ; $\mu_{(elect)}$ is the mobility of the electrons ; *E* is the electric field [15].

Reference:

[1] Albert Hofmann, The Physics of synchrotron radiation, Cambridge (2004).

[2] Waldemar. H. Scharf. Biomedical particle accelerators, American institute of physics, (1994).

[3] S. N. Ahmed, H. J. Besch, A. H. Walenta, N. Pavel, W. Schenk, High precision ionization chamber for relative intensity monitoring synchrotron radiation. Nucl. Instrum. Methods. A 449, 248-253, (2000).

[4] W. R. Dix, H. J. Besch, W. Graeff, C. W. Hamm. Coronary angiography with synchrotron radiation, jornal de physique IV (1994).

[5] N. A Mezenstv and V. F. Pindiurin. Application of synchrotron radiation to medical diagnostic at Novosibirsk: status and prospect, Nucl. Instrum. Methods. A261, 301-307,(1987).

[6] Glenn. F. knoll, Radiation detection and measurement, John Wiley & Sons, Inc (1999).

[7] C. F. G. Delaney, Radiation detectors, Oxford University Press, New York, (1992).

[8] A. M. Howatson, An introduction to gas discharge, Pergamon press, (1965).

[9] J. W. Boag, Ionization Measurements at very high intensities, British Journal of Radiology, 23, 601-611, (1950).

[10] Patricia. B. Scott, and J. R. Greening, Recombination in parallel plate free-air ionization chambers, British Journal of Radiology. 34, 791-800, (1961).

[11] J. W. Boag, General recombination in a standard parallel pate free air ionization chamber, Int. J. radiat. Chem, 1, 267-285, (1969).

[12] E. Nasser, Fundamentals of gaseous ionization and plasma electronics, John Wiley & Sons, Inc, (1971).

[13] L. G. H. Huxley, R. W. Crompton, The diffusion and drift of electrons in gases, John Wiley & Sons, Inc, (1974).

[14] W. Blume, W. Rirgler, L. Rolandi, Particle detection with drift chambers, Springer-verlag Berlin Heidelberg, (2008).

[15] R. H. Menk, Eine Vielkanalionisationskammer für Röntgenbildaufnahmen, PhD thesis, University of Siegen, (1994).

[16] H. Okuno, J. Fischer, V. Radeka and A. H. Walenta, Azimuthal spread of the avalanche in proportional champers, IEEE Transactions on Nuclear Sience, Vol. NS-26, 1, (1979).

[17] E. Gatti, A. Longoni, P. Rehak and M. Sampietro, Dynamics of electrons in drift detectors, Nucl. Instrum, Methods. A253, 393-399, (1987).

[18] S. Ramo, Current induced in electron motion, Proc. IRE 27, 584, (1939).

[19] W. Riegler, Extended theorems for signal induction in particle detectors VCI 2004, Nucl. Instrum. Methods. A 535, 287-293, (2004).

[20] O. Rübsamen privet contact.

[21] Leo. W. R, Techniques for nuclear and particle physics, Springer, (1994).

[22] G. W. Fraser and E. Mathieson, Monte Carlo calculation of electron transport coefficients in counting gas mixture Argon-methane mixture, Nucl. Instrum. Methods. A247, 544-565, (1986).

[23] S. N. Ahmed, Quantum fluctuations in a segmented ionization chamber for beam monitoring of synchrotron radiation, PhD thesis, University of Siegen, (1998).

[24] M. Cammarata, Chopper system for time resolved experiments with synchrotron radiation, Review of scientific instruments, 80, 015101, (2009).

[25] Polyimide 35N, Arlon.

[26] Inter connection NE, ShinEtsu.

[27] Nova Press FLEXIBLE/815, Frenzelit-Werke GmbH, Germany.

[28] V. K. Myalitsin, H. J. Besch, H. W. Schenk, A. H. Walenta, A Multichannel position sensitive ionization chamber for x-ray intensity monitoring. Nucl. Instrum. Methods. A323, 97-103, (1992).

[29] M. M. Costin, Position sensitive beam monitor for medical imaging with synchrotron radiation, M.Sc. Thesis University of Siegen (2006).

[30] Meilhaus manuel (AD ME 4661i).

[31] A. S. Niculae, Development of low noise analog readout for DEPFET pixel detector, Siegen, (2003).

[32] A. Andronic, et al, Space charge in drift chambers operated with the Xe, CO_2 (15%) mixture, Nucl. Instrum. Methods. A 525, 447–457, (2004).

[33] H. S. W. Massey and H. B. Gilbody, Electronic and ionic impact phenomena, Volume VI, Oxfors University Press, (1974).

Acknowledgement

First and foremost I offer my sincerest gratitude to my supervisor Professor. Albert H. Walenta, for his firmly support throughout my thesis, timely help, energetically encouragement, invaluable comments and discussion.

I would like to thank my committee members, Professor Hans D. Dahmen, Professor Ivor Fleck and Professor. Claus Grupen.

I would like to thank Dr. Werner Schenk, Dr. Tuba Çonka Nurdan and Dr. Kivanc Nurdan, for patient samples and helpful discussion during the study.

I would like to thank Dr. U. Werthenbach for his kindly help in design and constructing the detector.

I would like to thank, the people from the Mechanical and Electronic workshop Guido Schmidt, Dr. Michael Ziolkowski, Rainer Neumann, Olaf Meyer and Joachim Behner for their excellent technical help and discussion.

I really appreciated fruitful teamwork of my colleagues Dr. Hazim Yosef, Oliver Rübsamen and M.Sc. Mohamed Altaani.

My deep thanks to the working group members Dieter Junge, Dieter Gebauer, Andrea Brombach and Alfred Peper.

I greatly appreciate the love and support from my wife, Wafa Osman, and my Daughter, Lamees.

Finally, I thank my parents, brothers and sisters for supporting me throughout all my studies.